

#### LIBRARY Michigan State University

This is to certify that the dissertation entitled

#### DEVELOPMENT OF A TRANSMISSION SPECTROELECTROCHEMICAL METHOD WITH OPTICALLY TRANSPARENT DIAMOND ELECTRODE FOR THE STUDY OF REDOX PROTEINS

presented by

Yingrui Dai

has been accepted towards fulfillment of the requirements for the

Ph. D.	degree in _	Chemistry
	Jug M &	Sauce Sauce
	•	10, 2009
		Date

MSU is an affirmative-action, equal-opportunity employer

.\_\_\_\_

PLACE IN RETURN BOX to remove this checkout from your record.

TO AVOID FINES return on or before date due.

MAY BE RECALLED with earlier due date if requested.

DATE DUE	DATE DUE	DATE DUE

5/08 K:/Proj/Acc&Pres/CIRC/DateDue indd

## DEVELOPMENT OF A TRANSMISSION SPECTROELECTROCHEMICAL METHOD WITH OPTICALLY TRANSPARENT DIAMOND ELECTRODE FOR THE STUDY OF REDOX PROTEINS

Ву

Yingrui Dai

#### A DISSERTATION

Submitted to
Michigan State University
in partial fulfillment of the requirements
for the degree of

**DOCTOR OF PHILOSOPHY** 

Chemistry

2009

#### **ABSTRACT**

### DEVELOPMENT OF A TRANSMISSION SPECTROELECTROCHEMICAL METHOD WITH OPTICALLY TRANSPARENT DIAMOND ELECTRODE FOR THE STUDY OF REDOX PROTEINS

By

#### Yingrui Dai

The goal of the research was to develop a transmission spectroelectrochemical method with an optically transparent boron-doped diamond electrode that is useful for studying structure-function relationships of redox proteins.

First, the electrochemical behavior of the cytochrome *c* was investigated at boron-doped ultrananocrystalline diamond (UNCD) and microcrystalline diamond (MCD) electrodes. Quasi-reversible, diffusion-controlled electron transfer was observed at oxygen-terminated, but not hydrogen-terminated electrodes. UNCD electrodes exhibited a similar electrochemical response as the MCD electrodes but showed higher peak currents due to a larger electrochemical active area. pH-dependent studies of the voltammetric response revealed that the largest peak current and smallest peak separation were observed between pH 7 and 7.5.

Next, a custom-designed thin-layer transmission spectroelectrochemical cell was constructed and characterized. Electrochemical characterization of the thin-layer cell showed Gaussian-shaped thin-layer voltammetric *i-E* curves with a linear relationship between the peak current and the scan rate. Time-dependent measurements indicated rapid and complete electrolysis in the cell, and good

agreement between electrochemical and spectral data. The spectroelectrochemical studies of cytochrome c revealed an advantage of diamond OTE in terms of its fouling resistance. The spectral characterization of the cytochrome c-cyanide complex was also presented for the first time. The reversible spectroelectrochemical response of myoglobin demonstrated the applicability of the cell under anaerobic condition.

An analysis method was developed for studying a multicomponent redox protein, Na<sup>+</sup>-translocating NADH:quinone oxidoreductase (Na<sup>+</sup>-NQR). The UV-Vis difference spectra of this protein at diamond OTE without mediators indicated that the reversible reaction and complete electrolysis occurred in the thin-layer cell. The spectra were modeled with global regression analysis to resolve the redox centers in Na<sup>+</sup>-NQR and determine the corresponding formal potentials.

#### **DEDICATION**

To my husband

#### **ACKNOWLEDGEMENTS**

There are many people I want to thank during my time at Michigan State University. The first person I want to thank is my advisor, Dr. Greg M. Swain. Thanks for his guidance over the last five years. Thanks to Dr. Denis A. Proshlyakov for the helpful discussion and comments. Thanks to my committee members, Dr. Gary J. Blanchard, Dr. David P. Weliky and Dr. Shelagh Ferguson-Miller for the comments about my work. I also want to thank Dr. Denise A. Mills and Yi Zheng for the help with the protein work.

I have been fortunate to work with people in the Swain Group. Words alone can not express my gratefulness to my friends in chemistry department. It is nice to have you in my life that saw me through the process.

Finally, and most importantly, I would like to say thank you to my parents and husband. Without your love and support, I would not be here today. Thank you for always being there with me.

Grants from the National Science Foundation (CHE-0616730) and National Institutes of Health (GM 070544) are gratefully acknowledged.

#### **TABLE OF CONTENTS**

LIST OF TABLES	·viii
LIST OF FIGURES	·· ix
CHAPTER 1 INTRODUCTION	1
1.1 Spectroelectrochemistry	1
1.2 Transmission Spectroelectrochemistry	5
1.2.1 Optically Transparent Electrodes (OTE)	6
1.2.2 Development of Optically Transparent Boron-Doped Diamond	
Electrodes (Diamond OTE)	8
1.2.2.1 Boron-Doped Diamond Electrodes	8
1.2.2.2 Optically Transparent Boron-Doped Diamond Electrodes	.11
1.3 The Importance of Studying Structure-Function Relationships of	
Metalloproteins	
1.4 Na <sup>+</sup> -Translocating NADH:Quinone Oxidoreductase	
1.5 Specific Aims	.17
1.6 Organization of the Dissertation	
1.7 References	.19
CHAPTER 2 EXPERIMENTAL METHODS	.32
2.1 Electrode Materials	
2.1.1 Boron-Doped Diamond	
2.1.1.1 Ultrananocrystalline and Microcrystalline Boron-Doped Diamor	nd
Electrodes (UNCD and MCD)	.34
2.1.1.2 UV-Vis Transparent Boron-Doped Diamond Electrode	
(Diamond/Quartz OTE)	
2.1.2 Glassy Carbon	37
2.1.3 Gold Minigrid	
2.2 Cyclic Voltammetric Experiments	
2.3 Electrochemical Kinetics	
2.4 X-ray Photoelectron Spectroscopy (XPS)	
2.5 Spectroelectrochemical Measurements	
2.5.1 Thin-Layer Spectroelectrochemical Cell	
2.5.2 Potential Step Method	
2.5.3 UV-Vis Spectroelectrochemical Measurements	
2.6 Global Regression Analysis	
2.7 Chemicals	
2.8 References	49

CHAPTER		
	BORON-DOPED DIAMOND ELECTRODES	50
3.1 In	troduction	50
3.1.1	Electrochemical Studies of Cytochrome c	50
3.1.2	Oxygen-Terminated Boron-Doped Diamond Electrodes	
3.2 R	esults	
3.2.1	XPS Measurements	
3.2.2	Cyclic Voltammetric Studies	61
3.3 D	iscussion	68
3.4 C	onclusions	73
3.5 R	eferences	74
CHAPTER	R 4 SPECTROELECTROCHEMICAL BEHAVIOR OF REDOX	
	PROTEINS IN A THIN-LAYER TRANSMISSION CELL	78
4.1 Ir	ntroduction	78
4.1.1	Ideal Thin-Layer Behavior	79
4.1.2	Ideal Thin-Layer Transmission Cell	
4.1.3	Electrochemical Studies of Myoglobin	81
4.2 R	lesults	86
4.2.1	Electrochemical Performance of the Cell	86
4.2.2	Spectroelectrochemcial Kinetics	91
4.2.3	Spectroelectrochemistry of Cytochrome c – Cyanide Complex.	96
4.2.4	Spectroelectrochemistry of Myoglobin	100
4.3 D	viscussion	104
4.4 C	Conclusions	107
4.5 R	References	109
CHAPTE	R 5 SPECTROELECTROCHEMICAL STUDIES OF Na <sup>+</sup> - TRANSLOCATING NADH:QUINONE OXIDOREDUCTASE	
	FROM VIBRIO CHOLERAE	112
5.1 lr	ntroduction	
	Results	
	Discussion	
	Conclusions	
	References	
		•
CHAPTE	R. 6. CONCLUSIONS AND OUTLOOK	130

#### **LIST OF TABLES**

Table 2.1	Growth conditions for UNCD and MCD thin films deposited on <i>p-type</i> Si
Table 2.2	Growth conditions for UV-Vis optically transparent diamond electrode
Table 3.1	Summary of the surface composition on various diamond electrode surfaces
Table 3.2	Apparent heterogeneous electron-transfer rate constant, $k_{app}^{o}$ , calculated from cyclic voltammetric data
Table 3.3	pH dependence of the midpoint potential $E_{1/2}$ of cytochrome $c$ at boron-doped diamond electrodes. Scan rate=20 mV/s. Electrode area=0.2 cm <sup>2</sup> 68
Table 4.1	Extinction coefficients for horse myoglobin at pH 7, ~20 °C83
Table 5.1	Determined redox potentials for Na <sup>+</sup> -NQR125
Table 5.2	Redox transitions for known cofactors in Na <sup>+</sup> -NQR determined by Bogachev

#### LIST OF FIGURES

Figure 1.1	Different types of spectroelectrochemical techniques2
Figure 1.2	General design of an OTE and a thin-layer electrochemical cell for transmission spectroelectrochemical measurement6
Figure 1.3	Two conventional OTEs for transmission measurements: (A) a metal minigrid and (B) a thin film supported on an optically transparent substrate
Figure 1.4	Schematic bonding arrangement of sp <sup>3</sup> -bonded diamond9
Figure 2.1	A diagram of a microwave plasma-assisted CVD reactor used to grow boron-doped diamond thin-film electrodes32
Figure 2.2	Design of the single-compartment, three-electrode electrochemical cell with (a) the diamond film working electrode, (b) o-ring seal, (c) rubber spacer (and nickel foil), (d) reference electrode inside a glass capillary tube with a cracked tip, (e) carbon rod counter electrode, and (f) input for nitrogen purge gas
Figure 2.3	Diagram of the thin-layer transmission spectroelectrochemical cell. A thin layer (TL) is formed between the working electrode (WE) and the transmission window (not shown) and its thickness is determined by the spacer (SP). The thin layer is connected to the Pt counter electrode (CE) via electrolyte capillary (EC) between the transmission window and outer cell body. A miniature Ag/AgCl reference electrode (RE) is also connected to the electrolyte capillary via a cracked glass junction (GJ). Reference electrode capillary is also used for loading sample (SM), which is exhausted via a similar capillary on the opposite side (not shown)
Figure 2.4	Scheme for measuring the steady-state absorbance of a redox analyte as a function of the potential in a spectroelectrochemical measurement. An absorbance spectrum was recorded at each potential, as indicated by the arrows
Figure 2.5	Principle of difference absorbance spectroscopy. The difference spectrum B-A is generated by subtracting spectrum of initial state A from spectrum of product state B44

Figure 2.6	Potential-time profile for potential step studies of Na <sup>+</sup> -NQR. Absorbance spectra at the reference potential (dashed arrow) were recorded before and after each potential step (solid arrow). The difference absorbance spectrum was generated by subtracting the average of the absorbance spectra at reference potential from absorbance spectrum at each potential (e.g., $\Delta A = A_2 - (A_1 + A_3)/2$ )45
Figure 3.1	Heme <i>c</i> structure of cytochrome <i>c</i> . (A) Planar porphyrin ring system; (B) heme Fe is also bonded to histidine (His) and methionine (Met) axial ligands
Figure 3.2	Terminal atomic structure for hydrogen- and oxygen-terminated diamond (100) and (111) surfaces55
Figure 3.3	XPS spectra for (A) as-deposited, (B) oxygen-terminated, and (C) hydrogen-terminated UNCD electrode surfaces58
Figure 3.4	XPS spectra for UNCD electrode surfaces after potential cycling in cytochrome c solution. (A) Hydrogen-terminated surface; (B) oxygen-terminated surface
Figure 3.5	Cyclic voltammetric <i>i-E</i> curve of 0.1 mM cytochrome <i>c</i> in 0.1 M NaCl, 10 mM Tris-HCl (pH 7) solution at a hydrogen-terminated UNCD electrode. Scan rate=20 mV/s61
Figure 3.6	Cyclic voltammetric <i>i-E</i> curves for 0.1 mM cytochrome <i>c</i> in 0.1 M NaCl, 10 mM Tris-HCl buffer (pH 7) at oxygen-terminated (A) UNCD and (B) MCD electrodes. Curves are shown for different scan numbers. Scan rate=20 mV/s
Figure 3.7	Cyclic voltammetric background <i>i-E</i> curves for an oxygenterminated UNCD electrode. Cyclic voltammograms were measured in 0.1 M NaCl and 10 mM Tris-HCl (pH 7) before (solid line), after (dashed dot line) cytochrome <i>c</i> potential cycling and after purging with N <sub>2</sub> (dashed line) following cytochrome <i>c</i> measurements. Scan rate=20 mV/s
Figure 3.8	Cyclic voltammetric <i>i-E</i> curves for 0.1 mM cytochrome <i>c</i> in 0.1 M phosphate buffer (pH 7.5) at UNCD electrodes at different scan rates. Electrode area=0.2 cm <sup>2</sup>
Figure 3.9	Cyclic voltammetric data for cytochrome $c$ at UNCD electrodes. Electrode area=0.2 cm <sup>2</sup> . (A) Plot of reduction peak current for 0.1 mM cytochrome $c$ solution versus the square root of the scan rate; (B) Plot of reduction peak current versus cytochrome $c$

	7.5) at 20 mV/s66
Figure 3.10	Effect of the solution pH on the cytochrome <i>c</i> reduction peak current at boron-doped diamond electrodes. The solutions were 0.1 mM cytochrome <i>c</i> in 0.1 M phosphate buffer at different pH. Scan rate=20 mV/s. Electrode area=0.2 cm <sup>2</sup>
Figure 4.1	A theoretical cyclic voltammetric <i>i-E</i> curve for a reversible, one- electron redox reaction in a thin-layer cell79
Figure 4.2	Heme <i>b</i> structure of myoglobin. (A) Planar porphyrin ring system and (B) heme Fe is axially bound to a histidine molecule with the sixth coordination site remaining unoccupied or weakly ligated by a solvent molecule
Figure 4.3	UV-Vis spectra for horse myoglobin in different oxidation states with different bound ligands. Metmyoglobin (metMb): MbFe(III)H <sub>2</sub> O <sub>2</sub> deoxymyoglobin (deoxyMb): MbFe(II), oxymyoglobin (MbO <sub>2</sub> ): MbFe(II)O <sub>2</sub> and carboxymyoglobin (MbCO): MbFe(II)CO
Figure 4.4	Background-corrected cyclic voltammetric <i>i-E</i> curves for Fe(CN) <sub>6</sub> <sup>4</sup> in 1 M KCl in the thin-layer cell with a glassy carbon electrode. (A) Effect of scan rate for 1 mM Fe(CN) <sub>6</sub> <sup>4</sup> using the 75 $\mu$ m spacer; (B) effect of Fe(CN) <sub>6</sub> <sup>4</sup> concentration using the 75 $\mu$ m spacer at 1 mV/s (C) effect of layer thickness for 1 mM Fe(CN) <sub>6</sub> <sup>4</sup> at 1 mV/s; and (D) peak separation as a function of layer thickness
Figure 4.5	Plots of (A) oxidation peak current and (B) faradaic charge $vs.$ scar rate for different concentrations of $Fe(CN)_6^{-4}$ . The spacer thickness was 75 $\mu m$ and the supporting electrolyte was 1 M KCI90
Figure 4.6	Time dependence of the current and optical absorbance at 220 nm for $\text{Fe(CN)}_6^{-4}$ at a gold minigrid electrode in the thin-layer cell during a potential step from -0.1 to 0.6 V. Data are shown for supporting electrolyte concentration of (A) 100 mM KCl and (B) 1 M KCl. Lines are for the current on the left and markers are for the simultaneous optical changes on the right. The spacer thickness was 25 $\mu$ m 92
Figure 4.7	Cyclic voltammetric <i>i-E</i> curve for cytochrome <i>c</i> at a gold minigric electrode in a thin-layer cell with a 75 µm spacer. The analyte solution was 0.1 mM cytochorme <i>c</i> in 10 mM phosphate buffer (pF7) and 100 mM KCI. Scan rate=10 mV/s93

Figure 4.8	Difference absorbance spectra of cytochrome $c$ at a gold minigrid electrode in a thin-layer cell with a 75 $\mu$ m spacer. The Red-Ox difference spectra were generated during a potential step from 0.5 to -0.3 V. The analyte solution was 0.1 mM cytochorme $c$ in 10 mM phosphate buffer (pH 7) and 100 mM KCl. The spacer thickness was 75 $\mu$ m
Figure 4.9	Absorbance change of cytochrome $c$ on (A) a gold minigrid electrode and (B) a boron-doped diamond thin film at 418 nm. The analyte solution was 0.1 mM cytochorme $c$ in 10 mM phosphate buffer (pH 7) and 100 mM KCl. The spacer thickness was 75 $\mu$ m. Repetitive potential steps between 0.5 and -0.3 V were applied, as indicated in the figure
Figure 4.10	Spectroelectrochemical measurements of cytochrome <i>c</i> –cyanide complex on a boron-doped diamond electrode. (A) Absorption changes at characteristic wavelengths; (B-D) difference absorbance spectra between key states as designated by letters at o g; and (E) thermodynamic cycle of cytochrome <i>c</i> –cyanide complex. The analyte solution was 0.1 mM cytochorme <i>c</i> in 0.1 M KCN, Tris buffer (pH 7) and 100 mM KCl. Potentials were stepped between +0.3, -0.3 and -0.7 V as indicated in the figure98
Figure 4.11	Absorbance-time profiles and absorption spectra of myoglobin without (A, B) and with (C, D) far-UV light exposure. Spectra were recorded in the thin-layer transmission cell with a gold minigrid electrode. The spacer thickness was 75 μm. The analyte solution was 50 μM myoglobin in 10 mM sodium phosphate buffer (pH 7) and 100 mM KCl
Figure 4.12	Proposed mechanism for photoreduction of myoglobin107
Figure 5.1	Chemical structures of riboflavin, FMN, FAD and ubiquinone-8113
Figure 5.2	(A) UV-Vis absorption spectra for air-oxidized (solid line) and sodium dithionite reduced (dashed line) Na <sup>+</sup> -NQR purified from <i>Vibrio cholerae</i> . The solution was 0.01 mM Na <sup>+</sup> -NQR in 50 mM sodium phosphate buffer (pH 8), 100 mM NaCl, 1 mM EDTA, 5% glycerol and 0.05% dodecylmaltoside; (B) difference absorbance spectrum (Red-Ox) for Na <sup>+</sup> -NQR
Figure 5.3	Background-corrected cyclic voltammetric <i>i-E</i> curves for Na <sup>+</sup> -NQR at (A) a freshly polished glassy carbon electrode and (B) a diamond/quartz electrode with a 75 μm spacer. The analyte solution was 0.1 mM Na <sup>+</sup> -NQR in 50 mM sodium phosphate buffer

	(pH 8), 500 mM NaCl, 1 mM EDTA, 5% glycerol and 0.05% dodecylmaltoside. The scan rate was 0.5 mV/s118
Figure 5.4	Absorbance change of Na <sup>+</sup> -NQR (460nm) at a diamond/quartz OTE in a transmission cell with a 75 μm spacer. Potential steps to 0.2 and -0.7 V were applied as indicated in the figure. The analyte solution was 0.1 mM Na <sup>+</sup> -NQR in 50 mM sodium phosphate buffer (pH 8), 500 mM NaCl, 1 mM EDTA and 0.05% dodecylmaltoside
Figure 5.5	UV-Vis difference absorbance spectra measured for Na <sup>+</sup> -NQR at a diamond/quartz OTE in a transmission cell with a 75 μm spacer. Ox-Red and Red-Ox difference spectra were generated from the oxidized and reduced spectra collected at 0.2 and -0.7 V. The analyte solution was 0.1 mM Na <sup>+</sup> -NQR in 50 mM sodium phosphate buffer (pH 8), 500 mM NaCl, 1 mM EDTA and 0.05% dodecylmaltoside
Figure 5.6	Difference absorbance-potential curve (460 nm) for Na <sup>+</sup> -NQR at a diamond/quartz OTE in a transmission cell with a 75 μm spacer. The analyte solution was 0.1 mM Na <sup>+</sup> -NQR in 50 mM sodium phosphate buffer (pH 8), 500 mM NaCl, 1 mM EDTA and 0.05% dodecylmaltoside. The data were collected at a scan rate of 2 mV/s
Figure 5.7	UV-Vis difference absorbance spectra of Na <sup>+</sup> -NQR during cathodic and anodic potential steps at a diamond/quartz OTE in a transmission cell with a 75 μm spacer. The difference spectra were generated from the oxidized spectra collected at reference potential 0.2 V for reduction and oxidation potential steps every 100 mV and 20 min. The analyte solution was 0.1 mM Na <sup>+</sup> -NQR in 50 mM sodium phosphate buffer (pH 8), 500 mM NaCl, 1 mM EDTA and 0.05% dodecylmaltoside
Figure 5.8	Absorbance changes of Na <sup>+</sup> -NQR upon reduction ( <i>vs.</i> -0.1 V) and oxidation ( <i>vs.</i> -0.6 V) potential steps every 10 mV and 20 min. Markers: experimental data, solid line: global fitting results. The analyte solution was 0.1 mM Na <sup>+</sup> -NQR in 50 mM sodium phosphate buffer (pH 8), 500 mM NaCl, 1 mM EDTA and 0.05% dodecylmaltoside
Figure 5.9	Resolved spectra of redox transitions in Na <sup>+</sup> -NQR124

#### **CHAPTER 1**

#### INTRODUCTION

#### 1.1 Spectroelectrochemistry

Spectroelectrochemistry is a hybrid of two techniques: reaction-oriented electrochemistry and species-focused spectroscopy. The technique can be used to record the change in spectroscopic signature of an analyte associated with a change in redox state caused by electron transfer at an electrode. It provides more information about a redox reaction mechanism than can be acquired using traditional electrochemical methods alone.

Considerable development in spectroelectrochemistry has taken place since its inception in 1964 when Kuwana introduced this hybrid analytical method.<sup>1</sup> Over the years, spectroelectrochemistry has been used with electromagnetic radiation from multiple regions of the electromagnetic spectrum in the study of inorganic, organic, and biological redox systems.<sup>2-5</sup> Some commonly used spectroscopic methods that have been coupled with electrochemistry are listed in Figure 1.1.

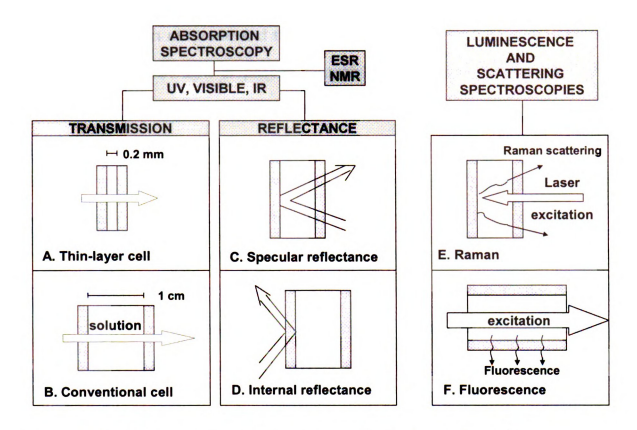


Figure 1.1 Different types of spectroelectrochemical techniques.<sup>2</sup>

Absorption spectroscopy using ultraviolet, visible, or infrared radiation is most often employed. In the transmission mode (Figure 1.1, A and B), the optical beam is directed orthogonally through an optically transparent electrode (OTE) and the adjacent solution layer. Specular reflectance spectroscopy (Figure 1.1, C) involves passing light through a solution layer and measurement of the light reflected from the electrode surface. In the internal reflection mode (Figure 1.1, D), the light beam is introduced through the back side of an OTE at an angle greater than the critical angle so that the beam is totally internally reflected. The light interacts with species present adjacent to the electrode surface. The sensitivity can be increased by introducing multiple reflections. In normal and resonance Raman spectroscopy (Figure 1.1, E), a laser beam is directed through

the solution at an electrode and the Raman back-scattered light is detected. A beam of excitation light is passed through an electrochemical cell and the resulting luminescence from electrogenerated species is recorded (Figure 1.1, F). Many other techniques, such as surface plasmon resonance (SPR), mass spectrometry (MS), electron paramagnetic resonance (EPR), nuclear magnetic resonance (NMR) and X-ray diffraction (XRD), have also been coupled with electrochemistry. In summary, the transmission mode provides information about the electrochemical reaction in the solution; the reflectance mode is more focused on the electrode/electrolyte interface; and the scattering mode is useful for the investigation of electrogenerated species adsorbed on the electrode surface.

The combination of spectroscopic and electrochemical techniques has enabled new and powerful combinations to be applied to complex redox systems. A recent book reviewed UV-Vis/IR/Raman/NMR/EPR spectroelectrochemistry and their application in analysis of redox reactions through identification of the intermediates and products to study iron-containing proteins, metalloporphyrins, mixed-valence complexes and organometallics. A series of papers by Heineman et al. reported a spectroelectrochemical sensor that is based on an attenuated total reflection measurement at an indium tin oxide (ITO) optically transparent electrode coated with a thin (20-500 nm thick) ion-exchange film. This type of sensor has been employed as a small portable unit for the detection of ferrocyanide in tank waste. Saavedra et al. used spectroelectrochemical

analysis to study surface-confined redox couples and characterize adsorbed polymer films on ITO electrodes with attenuated total reflectance spectroscopy. 30-<sup>36</sup> Lopez-Palacios et al. focused on using a reflection-transmission bidimensional spectroelectrochemistry cell to analyze the ion exchange processes during doping/dedoping of conducting polymers.<sup>37-44</sup> The Porter and Barbara groups demonstrated that single-molecule fluorescence spectroelectrochemistry was a powerful approach for the study of electron transfer process at highly heterogeneous interfaces using carbon OTE and ITO separately. 45 This technique was later employed by the Ackerman group to investigate the electron transfer dynamics of single redox molecules in aqueous solution using cresyl violet as a model fluorescent redox molecular probe. 46 Mantele and coworkers have used electrochemically-induced UV-Vis/IR transmission spectroscopy (spectroelectrochemistry) over the last two decades to study redox protein structure-function relationship. 47-76 The informative mid-IR difference spectra revealed information about complex molecular mechanisms, such as the conformational and hydrogen-bonding changes in the backbone and the side chains, protonation and deprotonation reactions of amino acid residues, and interactions between prosthetic groups and the protein.<sup>58</sup> Berthomieu and coworkers extended this method to the far infrared (50 cm<sup>-1</sup>) domain for the analysis of metal-ligand interactions in redox proteins with diamond windows.<sup>77</sup> The far-IR difference spectra can extend the analysis of vibrational properties to metal sites or redox states that are not accessible to resonance Raman spectroscopy.

#### 1.2 Transmission Spectroelectrochemistry

The transmission spectroelectrochemical measurement mode is most often used with a thin-layer cell and an optically transparent electrode (OTE). The general design of an OTE and the thin-layer electrochemical cell is shown in Figure 1.2.<sup>78</sup> A thin laver solution containing a redox analyte is confined between an optically transparent window and the working electrode. The OTE acts as the working electrode as well as the optically transparent window. The reference and counter electrodes are in contact with the thin layer solution but outside the optical path. Potential step and potential sweep methods are usually employed to drive the redox reaction inside the thin volume of solution. As the electromagnetic radiation with intensity,  $I_0$ , passes through the cell, changes in the spectroscopic signature for the redox analyte are recorded as a function of the applied potential (i.e., change in oxidation state). One of the main advantages of the thin-layer cell design is that the electroactive analyte present can be exhaustively electrolyzed in a very short time (typically 20-120 s depending on the cell thickness). In the design, there is finite diffusion, which means that the mathematical description of the electrochemical process can be simplified.

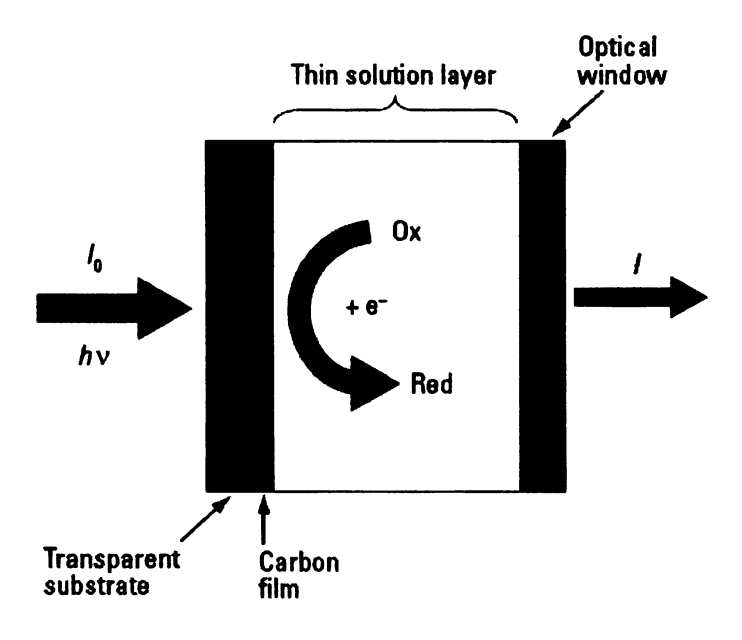


**Figure 1.2** General design of an OTE and a thin-layer electrochemical cell for transmission spectroelectrochemical measurement.<sup>78</sup>

#### 1.2.1 Optically Transparent Electrodes (OTE)

Transmission spectroelectrochemical measurements require an electrode that is transparent to the electromagnetic radiation. The electrode transparency enables potential-dependent spectra of electrogenerated species to be recorded in the thin layer solution. An ideal OTE should possess good electrical conductivity, high optical transparency, robustness and chemical inertness.<sup>78</sup>

# A. Minigrid OTE B. Film-Based OTE OTE Substrate 125 μm

**Figure 1.3** Two conventional OTEs for transmission measurements: (A) a metal minigrid and (B) a thin film supported on an optically transparent substrate.

One electrode architecture that would work for such measurements is a porous electrode. Examples are a minigrid electrode (e.g., Au, Ni, Ag or Cu),<sup>79-81</sup> which is simply a metal mesh (Figure 1.3 A) and porous reticulated vitreous carbon.<sup>82, 83</sup> Light is transmitted through the electrode openings, allowing one to probe changes in electronic properties or structural features of a molecule, brought about by a change in redox state. A gold minigrid is the most commonly used electrode material due to its accessibility and transmission over the entire electromagnetic spectrum.<sup>47, 48</sup> The disadvantages of this electrode type are the narrow potential window, the large background charging current and temporal instability due to protein denaturation even after surface modification. Due to their geometry, they are not suitable for optical probing of surface localized processes, such as adsorption. Also, their fragility limits the lifetime of the cell using such materials.

The other design is a thin conductive film (Figure 1.3 B) supported on an optically transparent substrate. Depending on the spectral region of interest, conductive thin films, such as metals, <sup>84, 85</sup> carbon materials, <sup>78, 83, 86-89</sup> and metal oxides, <sup>90-92</sup> can be employed. Usually, a compromise between electrical conductivity and transparency has to be reached as these two parameters are inversely related to one another, and both of them are controlled by film thickness. <sup>93</sup> The transparent substrate improves the mechanical stability of the thin OTE. Currently used OTE materials are indium–doped tin oxide (ITO) and boron-doped diamond. Both materials can be deposited as a thin film on transparent substrates, such as glass (visible), quartz (UV-Visible), germanium or silicon (infrared). The development and application of carbon OTEs were recently reviewed. <sup>78</sup>

# 1.2.2 Development of Optically Transparent Boron-Doped Diamond Electrodes (Diamond OTE)

#### 1.2.2.1 Boron-Doped Diamond Electrodes

Diamond is the hardest natural material, consisting of a crystal lattice of tetrahedrally-arranged sp³-bonded carbon atoms. This arrangement leads to six-membered rings in a chair conformation, as shown in Figure 1.4.94 It can be produced synthetically by two methods: (1) high-pressure-high-temperature (HPHT) growth (>1400 °C, >50,000 bar) in the presence of a catalyst; and (2) low pressure, low temperature (<1000 °C, 0.01-1 bar) chemical vapor deposition

(CVD) from a carbon-containing source gas mixture.<sup>95</sup> CVD diamond is usually polycrystalline with randomly-oriented crystallites and grain boundaries between the crystallites. These grain boundaries consist of a mixture of sp<sup>2</sup>- and sp<sup>3</sup>-bonded carbon.

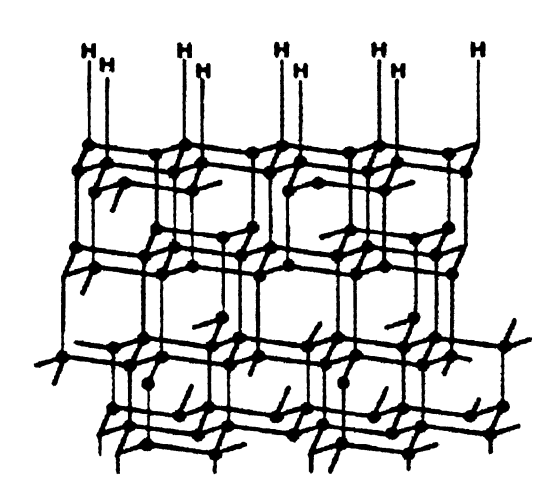


**Figure 1.4** Schematic bonding arrangement of sp<sup>3</sup>- bonded diamond.

Diamond is naturally an insulating material, so in order for it to be electrically conducting, it must be doped. Boron dopant atoms substitute for carbon atoms in the growing crystal lattice, which produces *p-type* semiconductivity with an acceptor level of 0.37 eV above the valence band.<sup>96</sup> Resistivities as low as 0.01 Ω-cm have been reported for degenerately boron-doped films, making them useful as electrochemical electrodes.<sup>96-109</sup> The surface carbon atoms are stabilized by strong covalent bonds with hydrogen for films deposited from hydrogen-rich source gas mixtures, as illustrated in Figure 1.4. Diamond can also be made *n-type* by doping with nitrogen<sup>110</sup> or phosphorus<sup>111-113</sup>. The deposition and properties of diamond with different dopants, such as sulfur, boron, nitrogen and phosphorus, have been studied by Haubner.<sup>114</sup>

The use of electrically conductive boron-doped diamond (BDD) as an electrode material is a field of research that had its beginnings back in the early 1990s. 115-117 There are three types of polycrystalline BDD: microcrystalline, nanocrystalline and ultrananocrystalline. Butler and Sumant recently reviewed the growth, characteristics, and applications of chemical vapor deposited ultrananocrystalline and nanocrystalline diamond films. 118 Angus et al. also reported on the growth, electrochemical properties and applications of diamond films. 119-127 Their recent finding regarding the surface conductivity of hydrogenterminated diamond may enable a new class of sensors. 128-130 Compton and coworkers also worked on the fabrication, characterization and application (e.g., metal ion analysis) of boron-doped diamond electrodes. 131-135 Moreover, Swain and Fujishima groups have been reporting on the deposition and application of boron-doped diamond electrodes in electroanalysis in the last two decades. 96, 99, 108, 109, 136-161 Much of the work, so far, has involved the characterization of the physical and electrochemical properties of boron-doped diamond and its electrochemical response toward a variety of aqueous and nonaqueous redox systems. From these results, it can be concluded that high-quality diamond, which means minimal nondiamond carbon impurity content, low secondary nucleation density, and hydrogen surface termination, offers significant advantages over other carbon and metal electrodes in terms of a wide potential window, lower and stable background current, fouling resistance, low limits of detection, and better robustness. 96, 109, 139, 155, 162

#### 1.2.2.2 Optically Transparent Boron-Doped Diamond Electrodes

Another unique property of diamond is its optical transparency. Diamond (undoped) has one of the widest optical windows of any material, extending from the band gap absorption edge (~225 nm) deep into the far infrared (~30 cm<sup>-1</sup>). <sup>163</sup> Factors that influence the optical throughput of diamond include the defect density, dopant type and doping level, film thickness and grain size (roughness). Adding boron dopant to improve the electrical conductivity reduces the optical throughput in isolated regions of the spectrum. It is, therefore, essential to establish a balance between the electrical and optical properties of boron-doped diamond in order to make the material a useful OTE. By adjusting the CVD growth conditions, it is possible to manipulate and optimize this balance.

The versatility of boron-doped diamond, both as an electrode and an optically transparent it material. makes obvious choice for an spectroelectrochemical measurements. 164 In general, diamond offers several advantages over other commonly used OTEs, including (1) a wide optical window extending from near UV into far-IR regions of the electromagnetic spectrum, (2) a wide working potential window and low background current, (3) stability during both cathodic and anodic polarization even at high current density and potential, (4) reproducibility of the electrical, optical and electrochemical properties from batch-to-batch, and (5) resistance to fouling because of a nonpolar, hydrogen-terminated surface. 164

Diamond OTEs have been employed by several groups in the spectroelectrochemical measurements. Martin and Morrison used internal reflection IR spectroelectrochemical measurements to study the types of carbonoxygen functional groups formed on the diamond surface during anodic polarization. 165, 166 Zhang et al. reported the use of a boron-doped diamondcoated platinum mesh electrode in the spectroelectrochemical measurement of high-potential redox species in aqueous solutions. 167 Our group has been developing optically transparent diamond electrodes for applications in the spectroelectrochemical measurements for some time now. 164, 168-171 Both freestanding diamond disks and diamond thin film deposited on guartz or undoped Si have been prepared. characterized and utilized in transmission spectroelectrochemical measurements. Zak et al. characterized a free-standing diamond disk in a thin-layer spectroelectrochemical cell for UV-Vis transmission measurements of Fe(CN)<sub>6</sub>-3/-4 and methyl viologen. Haymond et al. applied the free-standing diamond disk to study ferrocene in acetonitrile. Their work demonstrated that the boron-doped diamond is a practical OTE material for reproducible spectroelectrochemical measurements both in aqueous and nonaqueous media. However, due to the large thickness (380  $\mu$ m), the transparency was limited. In general, the low transparency, the long deposition time and laborious mechanical polishing needed to smooth the surface are limitations of this OTE architecture. Stotter et al. reported on the preparation and characterization of a thin film of optically transparent boron-doped diamond deposited on quartz for UV-Vis spectroelectrochemical measurements. 169

Absorption spectra of chlorpromazine and Fe(CN)<sub>6</sub>-3/-4 were recorded at different potentials, and the spectral changes were correlated with alterations in redox state of the molecules. Stotter et al. also compared the electrical, optical, and electrochemical properties of two optically transparent electrodes: diamond and ITO. 164 Boron-doped diamond has also been deposited on undoped silicon and been used in preliminary mid-IR spectroelectrochemical studies of cytochrome c. Such measurements allow one to probe the amino acid side chain and peptide backbone vibrations as a function of the redox state of the protein. 171 The preparation and application of a diamond/Si OTE in the mid- and far-IR transmission spectroelectrochemical measurements was recently reported. 78, 172 The results represent a first-step toward the ultimate goal of applying the spectroelectrochemical method study metal-ligand vibrations to in metalloproteins.

## 1.3 The Importance of Studying Structure-Function Relationships of Metalloproteins

Metalloproteins, about one-third of all proteins, are biomolecules that contain metal cofactors. A metal cofactor is either loosely or tightly bound to a protein and can be essential for the protein's biological functions. Metalloproteins are generally composed of protein atoms (carbon, nitrogen, oxygen, hydrogen, sulfur) and metal ions, such as iron, copper, calcium, zinc, magnesium, and so on. Iron and copper metalloproteins are usually referred to electron-transfer redox proteins, such as mononuclear copper proteins (cupredoxins),

mononuclear iron proteins (rubredoxin and desulforedoxin), iron-sulfur proteins (ferredoxins), and heme proteins (cytochromes). Hemoglobin, for example, which carries oxygen in the bloodstream, is an iron-containing metalloprotein.

Metalloproteins are involved in all fundamental biological processes including respiration, photosynthesis, regulation of transcription and translation, and metabolism.<sup>173</sup> Thus, metalloproteins make life on Earth possible and the ability to understand and ultimately control the binding and activity of protein metal sites is of great biological and medical importance. For example, myoglobin functions to transport and store oxygen and it has been used as a model system for the study of heme proteins. This protein has been studied extensively by a variety of techniques, such as spectroscopy, crystallography, and computation.<sup>174-183</sup>

However, the structure and its relationship to the function of many metalloproteins is still unclear. Due to their biological importance, structure-function relationships of metalloproteins are of considerable interest. Head-186 The metal ions in metalloproteins are critical to the protein's function, structure and stability. In fact, numerous essential biological functions require metal ions, and most of the metal ion functions involve metalloproteins. Metal-substituted heme proteins, which are created by replacing the heme iron with copper, cobalt or manganese, have been studied to elucidate the functional role of the heme iron in biological processes. Her-190 Biological ligands that bind to metalloproteins, such

as NO, O<sub>2</sub>, CO and H<sub>2</sub>, are very important in order for the metalloproteins to function properly in respiration, catalysis and signal transduction.<sup>182</sup> One of the major structural determinants of heme protein functional properties is the identity of the axial ligands of the protein which form the coordination environment of the heme iron.<sup>191</sup> The ligand dissociation pathways and protein structural change are key issues in understanding protein function.<sup>192</sup> It is almost certain that there are intermediate states along the pathway. Site-directed mutagenesis or semi-synthesis have been employed to change the axial ligands of heme proteins in order to study their functions.<sup>193-201</sup>

#### 1.4 Na<sup>+</sup>-Translocating NADH:Quinone Oxidoreductase

Vibrio cholerae, a motile bacterium with a single polar flagellum, is a causative agent of the potentially lethal disease cholera. The ability of the bacterium to use sodium in bioenergetic processes plays a key role in both adaptation to different environments and pathogenic function. This halophilic organism has a strict requirement of Na<sup>+</sup> for its growth, with an optimal pH ranging from 7 to 9 depending on the salinity. The enzyme that transports Na<sup>+</sup> across the cell membrane is essential for providing energy to the cell and for maintaining a constant intracellular environment.

Na<sup>+</sup>-translocating NADH:quinone oxidoreductase (Na<sup>+</sup>-NQR) acts as a redox-driven sodium pump in prokaryotes, such as marine bacteria (e.g., Vibrio alginolyticus) and human pathogenic bacteria (e.g., Vibrio cholerae).<sup>204</sup> This

membrane-bound enzyme couples the electron transfer from NADH to ubiquinone with Na<sup>+</sup> translocation across the membrane. It catalyzes the same redox reaction as the H<sup>+</sup>-pumping NADH:quinone oxidoreductase (complex I). However, the two enzymes share no homology.<sup>205</sup> The efficiency of Na<sup>+</sup> translocation by the Na<sup>+</sup>-NQR has been shown to be 1 Na<sup>+</sup>/ 1 e<sup>-</sup>.<sup>206</sup>

NADH + 
$$H_{in}^+$$
 Q + 2  $Na_{in}^+$   $\rightarrow$  NAD+ QH<sub>2</sub> + 2  $Na_{out}^+$ 

The electrochemical sodium gradient generated by Na<sup>+</sup>-NQR provides the energy for cellular metabolic function such as driving bacterial flagellum and transporting nutrients.<sup>207, 208</sup>

The mechanism of energy transformation between the redox transitions and sodium translocation across the membrane of Na<sup>+</sup>-NQR is still unknown. Na<sup>+</sup>-NQR is a favorable system to study the mechanism of a redox-driven ion pump. For example, as the redox transitions often involve H<sup>+</sup> uptake and release, the concentration of Na<sup>+</sup> can be changed over a wide range without changing the pH or causing a deleterious effect, allowing the variables to be examined independently. We would like to use the transmission spectroelectrochemical method together with global nonlinear regression analysis, to characterize the redox potentials of the cofactors in Na<sup>+</sup>-NQR and to determine their Na<sup>+</sup> sensitivity. The spectra with the global fitting can also resolve redox centers with similar thermodynamic parameters.

#### 1.5 Specific Aims

The long-term goal of this project is to develop a transmission spectroelectrochemical method using a diamond OTE to study structure-function relationships of redox-linked metalloproteins. We desire to use the technique to elucidate structural changes in redox systems as a function of the oxidation state. The specific aims of the research are listed below:

- 1. To investigate the electrochemical response of cytochrome c at boron-doped diamond electrodes as a function of surface chemistry, film morphology and solution pH. This aim will test the hypothesis that boron-doped diamond electrodes with different surface terminations should exhibit different performance in electrochemistry of cytochrome c;
- 2. To characterize a thin-layer transmission cell and study spectroelectrochemical behavior of model redox proteins in the cell;
- 3. To apply the spectroelectrochemical method together with global regression analysis to study a multicomponent redox protein, Na<sup>+</sup>-translocating NADH:quinone oxidoreductase. This aim will test the hypothesis that the spectroelectrochemical titrations can be used to determine redox potentials for the protein with multiple cofactors.

#### 1.6 Organization of the Dissertation

Chapter 1 gives background information about spectroelectrochemical methods, describes development of optically transparent boron-doped diamond electrodes and introduces the targeted redox protein. Chapter 2 details the experimental parameters and procedures used in the work, including the methods, instrumentation and materials.

Chapter 3 presents the direct electrochemistry of horse heart cytochrome c recorded with UNCD and MCD electrodes. A key finding was that well-defined electrochemical behavior was observed at oxidized boron-doped diamond electrode surfaces, but not at hydrogen-terminated electrodes. In Chapter 4, a specially designed thin-layer transmission cell is reported. It was electrochemically characterized with a glassy carbon electrode and employed in the spectroelectrochemical measurements of several model redox proteins. In Chapter 5, the spectroelectrochemical method and global nonlinear regression analysis were employed to study a redox protein (Na\*-NQR) with several cofactors.

Finally, Chapter 6 summarizes the key findings from this work and provides some future perspectives.

#### 1.7 References

- (1) Kuwana, T.; Darlington, K. R.; Leedy, D. W. *Anal. Chem.* **1964**, *36*, 2023-2025.
- (2) Heineman, W. R. Anal. Chem. 1978, 50, 390A-402A.
- (3) Heineman, W. R. J. Chem. Educ. 1983, 60, 305-308.
- (4) Heineman, W. R.; Hawkridge, F. M.; Blount, H. N. In *Electroanalytical Chemistry*; Bard, A. J., Ed.; Marcel Dekker: New York, 1984; Vol. 13, pp 1-113.
- (5) Bard, A. J.; Faulkner, L. R. In *Electrochemical Methods: Fundamentals and Applications*, 2 ed.; John Wiley & Sons: New York, 2001, pp 680-735.
- (6) Kaim, W.; Klein, A. Spectroelectrochemistry; Royal Society of Chemistry 2008.
- (7) Wansapura, C. M.; Seliskar, C. J.; Heineman, W. R. *Anal. Chem.* **2007**, *79*, 5594-5600.
- (8) Conklin, S. D.; Heineman, W. R.; Seliskar, C. J. *Electroanalysis* **2007**, *19*, 523-529.
- (9) Heineman, W. R.; Seliskar, C. J.; Morris, L. K.; Andria, S. E.; Wansapura, C.; Shtoyko, T. *ECS Trans.* **2006**, *3*, 5-12.
- (10) Shtoyko, T.; Richardson, J. N.; Seliskar, C. J.; Heineman, W. R. *Electrochim. Acta* **2005**, *50*, 3191-3199.
- (11) Conklin, S. D.; Heineman, W. R.; Seliskar, C. J. *Electroanalysis* **2005**, *17*, 1433-1440.
- (12) Andria, S. E.; Richardson, J. N.; Kaval, N.; Zudans, I.; Seliskar, C. J.; Heineman, W. R. *Anal. Chem.* **2004**, *76*, 3139-3144.
- (13) Stegemiller, M. L.; Heineman, W. R.; Seliskar, C. J.; Ridgway, T. H.; Bryan, S. A.; Hubler, T.; Sell, R. L. *Environ. Sci. Technol.* **2003**, *37*, 123-130.
- (14) Monk, D. J.; Ridgway, T. H.; Heineman, W. R.; Seliskar, C. J. *Electroanalysis* **2003**, *15*, 1198-1203.
- (15) Kaval, N.; Seliskar, C. J.; Heineman, W. R. *Anal. Chem.* **2003**, 75, 6334-6340.

- (16) Heineman, W. R.; Seliskar, C. J.; Richardson, J. N. *Aust. J. Chem.* **2003**, 56, 93-102.
- (17) Richardson, J. N.; Dyer, A. L.; Stegemiller, M. L.; Zudans, I.; Seliskar, C. J.; Heineman, W. R. *Anal. Chem.* **2002**, *74*, 3330-3335.
- (18) Maizels, M.; Seliskar, C. J.; Heineman, W. R.; Bryan, S. A. *Electroanalysis* **2002**, *14*, 1345-1352.
- (19) Ross, S. E.; Seliskar, C. J.; Heineman, W. R.; Aryol, S.; Nevin, J. H. *Proc. Electrochem. Soc.* **2001**, *2001-18*, 499-510.
- (20) Gao, L.; Seliskar, C. J.; Heineman, W. R. *Electroanalysis* **2001**, *13*, 613-620.
- (21) Slaterbeck, A. F.; Stegemiller, M. L.; Seliskar, C. J.; Ridgway, T. H.; Heineman, W. R. *Anal. Chem.* **2000**, *72*, 5567-5575.
- (22) Ross, S. E.; Seliskar, C. J.; Heineman, W. R. *Anal. Chem.* **2000**, 72, 5549-5555.
- (23) Maizels, M.; Seliskar, C. J.; Heineman, W. R. *Electroanalysis* **2000**, *12*, 1356-1362.
- (24) DiVirgilio-Thomas, J. M.; Heineman, W. R.; Seliskar, C. J. *Anal. Chem.* **2000**, *72*, 3461-3467.
- (25) Slaterbeck, A. F.; Ridgway, T. H.; Seliskar, C. J.; Heineman, W. R. *Anal. Chem.* **1999**. *71*. 1196-1203.
- (26) Gao, L.; Seliskar, C. J.; Heineman, W. R. *Anal. Chem.* **1999**, *71*, 4061-4068.
- (27) Slaterbeck, A. F.; Shi, Y.; Seliskar, C. J.; Ridgway, T. H.; Heineman, W. R. *Proc. Electrochem. Soc.* **1997**, *97-19*, 50-60.
- (28) Shi, Y.; Slaterbeck, A. F.; Seliskar, C. J.; Heineman, W. R. *Anal. Chem.* **1997**, *69*, 3679-3686.
- (29) Shi, Y.; Seliskar, C. J.; Heineman, W. R. *Anal. Chem.* **1997**, *69*, 4819-4827.
- (30) Doherty, W. J., III; Wysocki, R. J., Jr.; Armstrong, N. R.; Saavedra, S. S. *J. Phys. Chem. B* **2006**, *110*, 4900-4907.
- (31) Doherty, W. J., III; Wysocki, R. J.; Armstrong, N. R.; Saavedra, S. S. *Macromolecules* **2006**, *39*, 4418-4424.

- (32) Araci, Z. O.; Runge, A. F.; Doherty, W. J., III; Saavedra, S. S. *Isr. J. Chem.* **2006**, *46*, 249-255.
- (33) Ge, C.; Doherty, W. J.; Mendes, S. B.; Armstrong, N. R.; Saavedra, S. S. *Talanta* **2005**, *65*, 1126-1131.
- (34) Runge, A. F.; Saavedra, S. S. Langmuir 2003, 19, 9418-9424.
- (35) Doherty, W. J., III; Donley, C. L.; Armstrong, N. R.; Saavedra, S. S. *Appl. Spectrosc.* **2002**, *56*, 920-927.
- (36) Dunphy, D. R.; Mendes, S. B.; Saavedra, S. S.; Armstrong, N. R. *Anal. Chem.* **1997**, *69*, 3086-3094.
- (37) Lopez-Palacios, J.; Colina, A.; Heras, A.; Ruiz, V.; Fuente, L. *Anal. Chem.* **2001**, *73*, 2883-2889.
- (38) Ruiz, V.; Colina, A.; Heras, A.; Lopez-Palacios, J.; Seeber, R. *Helv. Chim. Acta* **2001**, *84*, 3628-3642.
- (39) Colina, A.; Lopez-Palacios, J.; Heras, A.; Ruiz, V.; Fuente, L. *J. Electroanal. Chem.* **2003**, *553*, 87-95.
- (40) Lopez-Palacios, J.; Heras, A.; Colina, A.; Ruiz, V. *Electrochim. Acta* **2004**, *49*, 1027-1033.
- (41) Ruiz, V.; Colina, A.; Heras, A.; Lopez-Palacios, J. *Electrochim. Acta* **2004**, *50*, 59-67.
- (42) Lopez-Palacios, J.; Munoz, E.; Heras, M. A.; Colina, A.; Ruiz, V. *Electrochim. Acta* **2006**, *52*, 234-239.
- (43) Orcajo, O.; Ventosa, E.; Martinez, A.; Colina, A.; Heras, A.; Ruiz, V.; Lopez-Palacios, J. *J. Electroanal. Chem.* **2006**, *596*, 95-100.
- (44) Ruiz, V.; Colina, A.; Heras, A.; Lopez-Palacios, J. *Polym. Degrad. Stab.* **2006**, *91*, 3117-3123.
- (45) Palacios, R. E.; Fan, F.-R. F.; Bard, A. J.; Barbara, P. F. *J. Am. Chem. Soc.* **2006**, *128*, 9028-9029.
- (46) Lei, C.; Hu, D.; Ackerman, E. J. Chem. Commun. 2008, 5490-5492.
- (47) Moss, D.; Nabedryk, E.; Breton, J.; Mantele, W. Eur. J. Biochem. 1990, 187, 565-572.
- (48) Schlereth, D. D.; Mantele, W. Biochemistry 1992, 31, 7494-7502.

- (49) Brischwein, M.; Scharf, B.; Engelhard, M.; Mantele, W. *Biochemistry* **1993**, 32, 13710-13717.
- (50) Leonhard, M.; Mantele, W. *Biochemistry* **1993**, *32*, 4532-4538.
- (51) Mantele, W. Trends Biochem. Sci. 1993, 18, 197-202.
- (52) Schlereth, D. D.; Fernandez, V. M.; Mantele, W. *Biochemistry* **1993**, 32, 9199-9208.
- (53) Schlereth, D. D.; Mantele, W. Biochemistry 1993, 32, 1118-1126.
- (54) Hellwig, P.; Rost, B.; Kaiser, U.; Ostermeier, C.; Michel, H.; Mantele, W. *FEBS Lett.* **1996**, *385*, 53-57.
- (55) Behr, J.; Hellwig, P.; Mantele, W.; Michel, H. *Biochemistry* **1998**, *37*, 7400-7406.
- (56) Hellwig, P.; Behr, J.; Ostermeier, C.; Richter, O. M.; Pfitzner, U.; Odenwald, A.; Ludwig, B.; Michel, H.; Mantele, W. *Biochemistry* **1998**, *37*, 7390-7399.
- (57) Hellwig, P.; Ostermeier, C.; Michel, H.; Ludwig, B.; Mantele, W. *Biochim. Biophys. Acta, Bioenerg.* **1998**, *1409*, 107-112.
- (58) Baymann, F.; Robertson, D. E.; Dutton, P. L.; Mantele, W. *Biochemistry* **1999**, *38*, 13188-13199.
- (59) Hellwig, P.; Grzybek, S.; Behr, J.; Ludwig, B.; Michel, H.; Mantele, W. *Biochemistry* **1999**, *38*, 1685-1694.
- (60) Hellwig, P.; Mogi, T.; Tomson, F. L.; Gennis, R. B.; Iwata, J.; Miyoshi, H.; Mantele, W. *Biochemistry* **1999**, *38*, 14683-14689.
- (61) Hellwig, P.; Soulimane, T.; Buse, G.; Mantele, W. *FEBS Lett.* **1999**, *458*, 83-86.
- (62) Hellwig, P.; Soulimane, T.; Buse, G.; Mantele, W. *Biochemistry* **1999**, *38*, 9648-9658.
- (63) Kuglstatter, A.; Hellwig, P.; Fritzsch, G.; Wachtveitl, J.; Oesterhelt, D.; Mantele, W.; Michel, H. FEBS Lett. 1999, 463, 169-174.
- (64) Taneva, S. G.; Kaiser, U.; Donchev, A. A.; Dimitrov, M. I.; Mantele, W.; Muga, A. *Biochemistry* **1999**, *38*, 9640-9647.
- (65) Friedrich, T.; Brors, B.; Hellwig, P.; Kintscher, L.; Rasmussen, T.; Scheide, D.; Schulte, U.; Mantele, W.; Weiss, H. *Biochim. Biophys. Acta, Bioenerg.* **2000**, *1459*, 305-309.

- (66) Hellwig, P.; Scheide, D.; Bungert, S.; Mantele, W.; Friedrich, T. *Biochemistry* **2000**, *39*, 10884-10891.
- (67) Hellwig, P.; Rost, B.; Mantele, W. Spectrochim. Acta, Part A 2001, 57A, 1123-1131.
- (68) Hellwig, P.; Pfitzner, U.; Behr, J.; Rost, B.; Pesavento, R. P.; Donk, W. v.; Gennis, R. B.; Michel, H.; Ludwig, B.; Mantele, W. *Biochemistry* **2002**, *41*, 9116-9125.
- (69) Hellwig, P.; Soulimane, T.; Mantele, W. *Eur. J. Biochem.* **2002**, 269, 4830-4838.
- (70) Ritter, M.; Anderka, O.; Ludwig, B.; Mantele, W.; Hellwig, P. *Biochemistry* **2003**, *42*, 12391-12399.
- (71) Wille, G.; Ritter, M.; Friedemann, R.; Mantele, W.; Hubner, G. *Biochemistry* **2003**, *42*, 14814-14821.
- (72) Ritter, M.; Palsdottir, H.; Abe, M.; Mantele, W.; Hunte, C.; Miyoshi, H.; Hellwig, P. *Biochemistry* **2004**, *43*, 8439-8446.
- (73) Haas Alexander, H.; Sauer Ursula, S.; Gross, R.; Simon, J.; Mantele, W.; Lancaster, C. R. D. *Biochemistry* **2005**, *44*, 13949-13961.
- (74) Mileni, M.; Haas, A. H.; Mantele, W.; Simon, J.; Lancaster, C. R. D. *Biochemistry* **2005**, *44*, 16718-16728.
- (75) Bernad, S.; Mantele, W. Anal. Biochem. 2006, 351, 214-218.
- (76) Hellwig, P.; Bohm, A.; Pfitzner, U.; Mantele, W.; Ludwig, B. *Biochim. Biophys. Acta* **2008**, *1777*, 220-226.
- (77) Berthomieu, C.; Marboutin, L.; Dupeyrat, F.; Bouyer, P. *Biopolymers* **2006**, *82*, 363-367.
- (78) Dai, Y.; Swain, G.; Porter, M. D.; Zak, J. Anal. Chem. 2008, 80, 14-22.
- (79) Murray, R. W.; Heineman, W. R.; O'Dom, G. W. *Anal. Chem.* **1967**, 39, 1666-1668.
- (80) Petek, M.; Neal, T. E.; Murray, R. W. Anal. Chem. 1971, 43, 1069-1074.
- (81) Blaedel, W. J.; Boyer, S. L. Anal. Chem. 1973, 45, 258-263.
- (82) Norvell, V. E.; Mamantov, G. Anal. Chem. 1977, 49, 1470-1472.
- (83) Sorrels, J. W.; Dewald, H. D. Anal. Chem. 1990, 62, 1640-1643.

- (84) Yildiz, A.; Kissinger, P. T.; Reilley, C. N. Anal. Chem. 1968, 40, 1018-1024.
- (85) Benken, W. v.; Kuwana, T. Anal. Chem. 1970, 42, 1114-1116.
- (86) DeAngelis, T. P.; Hurst, R. W.; Yacynych, A. M.; Mark, H. B.; Jr.; William R, H.; Mattson, J. S. *Anal. Chem.* **1977**, *49*, 1395-1398.
- (87) Zak, J.; Porter, M. D.; Kuwana, T. Anal. Chem. 1983, 55, 2219-2222.
- (88) Anjo, D. M.; Brown, S.; Wang, L. Anal. Chem. 1993, 65, 317-319.
- (89) Donner, S.; Li, H.-W.; Yeung, E. S.; Porter, M. D. *Anal. Chem.* **2006**, *78*, 2816-2822.
- (90) Armstrong, N. R.; Lin, A. W. C.; Fujihira, M.; Kuwana, T. *Anal. Chem.* **1976**, *48*, 741-750.
- (91) Ginley, D. S.; Bright, C. MRS Bulletin 2000, 25, 15-18.
- (92) Donley, C.; Dunphy, D.; Paine, D.; Carter, C.; Nebesny, K.; Lee, P.; Alloway, D.; Armstrong, N. R. *Langmuir* **2002**, *18*, 450-457.
- (93) Haacke, G. Ann. Rev. Mater. Sci. 1977, 7, 73-93.
- (94) Fischer, A. Ph. D. dissertation, Michigan State University, East Lansing, MI, 2005.
- (95) Pankove, J. I.; Qiu, C. In *Synthetic Diamond: Emerging CVD Science and Technology*; Spear, K. E., Dismukes, J. P., Eds.; John Wiley & Sons: New York, 1994.
- (96) Swain, G. M.; Anderson, A. B.; Angus, J. C. MRS Bulletin 1998, 23, 56-59.
- (97) Swain, G. M. In *Electroanalytical Chemistry*; Bard, A. J., Rubinstein, I., Eds.; Marcel Dekker, 2004; Vol. 22, pp 182-277.
- (98) Swain, G. M. In *Thin-Film Diamond II (Semiconductors and Semimetals)*; Nebel, C. E., Ristein, J., Eds.; Elsevier, 2004; Vol. 77, pp 121-148.
- (99) Sonthalia, P.; McGaw, E.; Show, Y.; Swain, G. M. *Anal. Chim. Acta* **2004**, *522*, 35-44.
- (100) Fischer, A. E.; Show, Y.; Swain, G. M. Anal. Chem. 2004, 76, 2553-2560.
- (101) Bennett, J. A.; Wang, J.; Show, Y.; Swain, G. M. J. Electrochem. Soc. **2004**, *151*, E306-E313.
- (102) Haymond, S.; Babcock, G. T.; Swain, G. M. *Electroanalysis* **2003**, *15*, 249-253.

- (103) Show, Y.; Witek, M. A.; Sonthalia, P.; Swain, G. M. Chem. Mater. 2003, 15, 879-888.
- (104) Chen, Q.; Gruen, D. M.; Krauss, A. R.; Corrigan, T. D.; Witek, M.; Swain, G. M. *J. Electrochem. Soc.* **2001**, *148*, E44-E51.
- (105) Granger, M. C.; Witek, M.; Xu, J.; Wang, J.; Hupert, M.; Hanks, A.; Koppang, M. D.; Butler, J. E.; Lucazeau, G.; Mermoux, M.; Strojek, J. W.; Swain, G. M. Anal. Chem. 2000, 72, 3793-3804.
- (106) Koppang, M. D.; Witek, M.; Blau, J.; Swain, G. M. *Anal. Chem.* **1999**, *71*, 1188-1195.
- (107) Granger, M. C.; Swain, G. M. J. Electroanal. Chem. 1999, 146, 4551-4558.
- (108) Xu, J.; Swain, G. M. Anal. Chem. 1998, 70, 1502-1510.
- (109) Xu, J.; Granger, M. C.; Chen, Q.; Strojek, J. W.; Lister, T. E.; Swain, G. M. *Anal. Chem.* **1997**, *69*, 591A-597A.
- (110) James, B.; Carlisle, J. A.; Auciello, O.; Gruen, D. M.; Gibson, J. M. *Appl. Phys. Lett.* **2002**, *81*, 2235-2237.
- (111) Okano, K.; Kiyota, H.; Iwasaki, T.; Nakamura, Y.; Akiba, Y.; Kurosu, T.; Iida, M.; Nakamura, T. *Appl. Phys. A:Mater.* **1990**, *51*, 344-346.
- (112) Koizumi, S.; Kamo, M.; Sato, Y.; Ozaki, H.; Inuzuka, T. *Appl. Phys. Lett.* **1997**, *71*, 1065-1067.
- (113) Koizumi, S. Phys. Status Solidi A 1999, 172, 71-78.
- (114) Haubner, R. *Diam. Relat. Mater.* **2005**, *14*, 355-363.
- (115) Bachmann, P. K.; Leers, D.; Lydtin, H. Diam. Relat. Mater. 1991, 1, 1-12.
- (116) Liu, H.; Dandy, D. S. Diam. Relat. Mater. 1995, 4, 1173-1188.
- (117) Ashfold, M. N. R.; May, P. W.; Rego, C. A.; Everitt, N. M. *Chem. Soc. Rev.* **1994**, 21-30.
- (118) Butler, J. E.; Sumant, A. V. Chemical Vapor Deposition 2008, 14, 145-160.
- (119) Martin, H. B.; Eaton, S. C.; Landau, U.; Angus, J. C. *Diamond Electrochem.* **2005**, 26-50.
- (120) Angus, J. C.; Pleskov, Y. V.; Eaton, S. C. Semiconductors and Semimetals 2004, 77, 97-119.

- (121) Eaton, S. C.; Anderson, A. B.; Angus, J. C.; Evstefeeva, Y. E.; Pleskov, Y. V. *Diamond Relat. Mater.* **2003**, *12*, 1627-1632.
- (122) Albu, T. V.; Anderson, A. B.; Angus, J. C. *J. Electrochem. Soc.* **2002**, *149*, E143-E147.
- (123) Angus, J. C.; Martin, H. B.; Landau, U.; Evstefeeva, Y. E.; Miller, B.; Vinokur, N. New Diamond Front. Carbon Technol. 1999, 9, 175-187.
- (124) Martin, H. B.; Smith, B. A.; Angus, J. C.; Landau, U.; Anderson, A. B. *Mater. Res. Soc. Symp. Proc.* **1999**, *555*, 217-226.
- (125) Angus, J. C.; Evans, E. A. *Mater. Res. Soc. Symp. Proc.* **1994**, *349*, 385-390.
- (126) Angus, J. C.; Argoitia, A.; Gat, R.; Li, Z.; Sunkara, M.; Wang, L.; Wang, Y. *Thin Film Diamond* **1994**, 1-14.
- (127) Angus, J. C. Synth. Diamond: Emerging CVD Sci. Technol. 1994, 21-39.
- (128) Chakrapani, V.; Anderson, A. B.; Angus, J. C. AIChE Annual Meeting, Conference Proceedings, Cincinnati, OH, United States, Oct. 30-Nov. 4, 2005 2005, 395c/391-395c/310.
- (129) Chakrapani, V.; Angus, J. C.; Anderson, A. B.; Sumanasekera, G. U. *Mater. Res. Soc. Symp. Proc.* **2007**, *956*, 89-96.
- (130) Chakrapani, V.; Angus, J. C.; Anderson, A. B.; Wolter, S. D.; Stoner, B. R.; Sumanasekera, G. U.; Landstrass, M. I.; Ravi, K. V.; Maier, F.; Riedel, B.; Mantel, J.; Ristein, J.; Ley, L. Science (Washington, DC, United States) 2007, 318, 1424-1430.
- (131) Toghill, K. E.; Wildgoose, G. G.; Moshar, A.; Mulcahy, C.; Compton, R. G. *Electroanalysis* **2008**, *20*, 1731-1737.
- (132) Rassaei, L.; Sillanpaa, M.; French, R. W.; Compton, R. G.; Marken, F. *Electroanalysis* **2008**, *20*, 1286-1292.
- (133) Omanovic, D.; Kwokal, Z.; Goodwin, A.; Lawrence, A.; Banks, C. E.; Compton, R. G.; Komorsky-Lovric, S. *J. Iran. Chem. Soc.* **2006**, *3*, 128-139.
- (134) Lawrence, N. S.; Pagels, M.; Meredith, A.; Jones, T. G. J.; Hall, C. E.; Pickles, C. S. J.; Godfried, H. P.; Banks, C. E.; Compton, R. G.; Jiang, L. *Talanta* **2006**, *69*, 829-834.
- (135) Ji, X.; Buzzeo, M. C.; Banks, C. E.; Compton, R. G. *Electroanalysis* **2006**, *18*, 44-52.

- (136) Wang, Y.; Novotny, M.; Quaiserova-Mocko, V.; Swain, G. M.; Wang, D. H. *Am. J. Physiol.* **2008**, *294*, R1517-R1523.
- (137) Muna, G. W.; Swope, V. M.; Swain, G. M.; Porter, M. D. *J. Chromatogr., A* **2008**, *1210*, 154-159.
- (138) Song, Y.; Swain, G. M. Anal. Chem. 2007, 79, 2412-2420.
- (139) McGaw, E. A.; Swain, G. M. Anal. Chim. Acta 2006, 575, 180-189.
- (140) Rao, T. N.; Yagi, I.; Miwa, T.; Tryk, D. A.; Fujishima, A. *Anal. Chem.* **1999**, 71, 2506-2511.
- (141) Yamada, D.; Ivandini, T. A.; Komatsu, M.; Fujishima, A.; Einaga, Y. *J. Electroanal. Chem.* **2008**, *615*, 145-153.
- (142) Wei, M.; Zhou, Y.; Zhi, J.; Fu, D.; Einaga, Y.; Fujishima, A.; Wang, X.; Gu, Z. *Electroanalysis* **2008**, *20*, 137-143.
- (143) Wei, M.; Sun, L.-G.; Xie, Z.-Y.; Zhii, J.-F.; Fujishima, A.; Einaga, Y.; Fu, D.-G.; Wang, X.-M.; Gu, Z.-Z. *Adv. Funct. Mater.* **2008**, *18*, 1414-1421.
- (144) Preechaworapun, A.; Ivandini, T. A.; Suzuki, A.; Fujishima, A.; Chailapakul, O.; Einaga, Y. *Anal. Chem.* **2008**, *80*, 2077-2083.
- (145) Kondo, T.; Tamura, A.; Fujishima, A.; Kawai, T. *ECS Trans.* **2008**, *16*, 465-473.
- (146) Kondo, T.; Niwano, Y.; Tamura, A.; Ivandini, T. A.; Einaga, Y.; Tryk, D. A.; Fujishima, A.; Kawai, T. *Electroanalysis* **2008**, *20*, 1556-1564.
- (147) Chiku, M.; Ivandini, T. A.; Kamiya, A.; Fujishima, A.; Einaga, Y. *J. Electroanal. Chem.* **2008**, *612*, 201-207.
- (148) Tryk, D. A.; Tachibana, H.; Inoue, H.; Fujishima, A. *Diam. Relat. Mater.* **2007**, *16*, 881-887.
- (149) Terashima, C.; Fujishima, A. Compr. Anal. Chem. 2007, 49, 211-232.
- (150) Spataru, T.; Spataru, N.; Fujishima, A. Talanta 2007, 73, 404-406.
- (151) Ivandini, T. A.; Sato, R.; Makide, Y.; Fujishima, A.; Einaga, Y. *Anal. Chem.* **2006**, *78*, 6291-6298.
- (152) Dragoe, D.; Spataru, N.; Kawasaki, R.; Manivannan, A.; Spataru, T.; Tryk, D. A.; Fujishima, A. *Electrochim. Acta* **2006**, *51*, 2437-2441.
- (153) Fujishima, A.; Einaga, Y.; Rao, T. N.; Tryk, D. A. *Diamond Electrochemistry*, 2005.

- (154) Rao, T. N.; Sarada, B. V.; Fujishima, A. Advances in Surface Treatment: Research & Applications (ASTRA), Proceedings of the International Conference, Hyderabad, India, Nov. 3-6, 2003 2004, 716-722.
- (155) Rao, T. N.; Loo, B. H.; Sarada, B. V.; Terashima, C.; Fujishima, A. *Anal. Chem.* **2002**, *74*, 1578-1583.
- (156) Yagi, I.; Notsu, H.; Kondo, T.; Tryk, D. A.; Fujishima, A. *J. Electroanal. Chem.* **1999**, *473*, 173-178.
- (157) Quaiserova-Mocko, V.; Novotny, M.; Schaefer, L. S.; Fink, G. D.; Swain, G. M. *Electrophoresis* **2008**, *29*, 441-447.
- (158) Park, J.; Quaiserova-Mocko, V.; Patel, B. A.; Novotny, M.; Liu, A.; Bian, X.; Galligan, J. J.; Swain, G. M. *Analyst (Cambridge, United Kingdom)* **2008**, 133, 17-24.
- (159) Park, J.; Galligan, J. J.; Fink, G. D.; Swain, G. M. *J. Physiol.* **2007**, *584*, 819-834.
- (160) Novotny, M.; Quaiserova-Mocko, V.; Wehrwein, E. A.; Kreulen, D. L.; Swain, G. M. J. Neurosci. Methods 2007, 163, 52-59.
- (161) Song, Y.; Swain, G. M. Anal. Chim. Acta 2007, 593, 7-12.
- (162) Fujishima, A.; Rao, T. N.; Try, D. A. *Proc.-Electrochem. Soc.* **2000**, 99-32, 383-388.
- (163) Zaitsev, A. M. Optical Properties of Diamond; Springer-Verlag: Berlin, 2001.
- (164) Stotter, J.; Show, Y.; Wang, S.; Swain, G. Chem. of Mater. 2005, 17, 4880-4888.
- (165) Martin, H. B.; Morrison, P. W. *Electrochem. and Solid-State Lett.* **2001**, *4*, E17-E20.
- (166) Martin, H. B.; Morrison, P. W., Jr. *Proc. Electrochem. Soc.* **2002**, 2001-25, 66-73.
- (167) Zhang, Y.; Kato, Y.; Yoshihara, S.; Watanabe, T. *J. Electroanal. Chem.* **2007**, *603*, 135-141.
- (168) Zak, J. K.; Butler, J. E.; Swain, G. M. Anal. Chem. 2001, 73, 908-914.
- (169) Stotter, J.; Zak, J.; Behler, Z.; Show, Y.; Swain, G. M. *Anal. Chem.* **2002**, 74, 5924-5930.

- (170) Haymond, S.; Zak, J. K.; Show, Y.; Butler, J. E.; Babcock, G. T.; Swain, G. M. *Anal. Chim. Acta* **2003**, *500*, 137-144.
- (171) Stotter, J.; Haymond, S.; Zak, J. K.; Show, Y.; Cvackova, Z.; Swain, G. M. *Interface* **2003**, *12*, 33-38.
- (172) Dai, Y.; Proshlyakov, D. A.; Zak, J. K.; Swain, G. M. *Anal. Chem.* **2007**, *79*, 7526-7533.
- (173) Degtyarenko, K. In *Encyclopedia of Genetics, Genomics, Proteomics and Bioinformatics*; Lynn Jorde, P. L., Mike Dunn and Shankar Subramaniam Ed.; John Wiley & Sons, Inc., 2005.
- (174) Austin, R. H.; Beeson, K. W.; Eisenstein, L.; Frauenfelder, H.; Gunsalus, I. C. *Biochemistry* **1975**, *14*, 5355-5373.
- (175) Alben, J. O.; Beece, D.; Bowne, S. F.; Doster, W.; Eisenstein, L.; Frauenfelder, H.; Good, D.; McDonald, J. D.; Marden, M. C.; et al. *Proc. Natl. Acad. Sci. U. S. A.* 1982, 79, 3744-3748.
- (176) Tilton, R. F., Jr.; Singh, U. C.; Weiner, S. J.; Connolly, M. L.; Kuntz, I. D., Jr.; Kollman, P. A.; Max, N.; Case, D. A. J. Mol. Biol. 1986, 192, 443-456.
- (177) Elber, R.; Karplus, M. Science (Washington, D. C., 1883-) 1987, 235, 318-321.
- (178) Powers, L.; Chance, B.; Chance, M.; Campbell, B.; Friedman, J.; Khalid, S.; Kumar, C.; Naqui, A.; Reddy, K. S.; Zhou, Y. *Biochemistry* **1987**, *26*, 4785-4796.
- (179) Carlson, M. L.; Regan, R. M.; Gibson, Q. H. *Biochemistry* **1996**, *35*, 1125-1136.
- (180) Scott, E. E.; Gibson, Q. H. Biochemistry 1997, 36, 11909-11917.
- (181) Chu, K.; Berendzen, J.; Sweet, R. M.; Schlichting, I. *Biophys. J.* **1999**, *77*, 2153-2174.
- (182) Chu, K.; Vojtchovsky, J.; McMahon, B. H.; Sweet, R. M.; Berendzen, J.; Schlichting, I. *Nature* **2000**, *403*, 921-923.
- (183) Antonini, E.; Brunori, M. *Hemoglobin and myoglobin in their reactions with ligands*; North-Holland Pub. Co.: Amsterdam, 1971.
- (184) Ortiz de Montellano, P. R. Acc. Chem. Res. 1987, 20, 289-294.
- (185) Dawson, J. H. Science 1988, 240, 433-439.

- (186) Barker, P. D.; Ferrer, J. C.; Mylrajan, M.; Loehr, T. M.; Feng, R.; Konishi, Y.; Funk, W. D.; MacGillivray, R. T.; Mauk, A. G. *Proc. Natl. Acad. Sci. U. S. A.* 1993, 90, 6542-6546.
- (187) Fabry, T. L.; Simo, C.; Javaherian, K. *Biochim. Biophys. Acta* **1968**, *160*, 118-122.
- (188) Zomzely, C. E.; Roberts, S.; Peache, S. *Proc. Natl. Acad. Sci. U. S. A.* **1970**, *67*, 644-651.
- (189) Yonetani, T.; Drott, H. R.; Leigh, J. S., Jr.; Reed, G. H.; Waterman, M. R.; Asakura, T. *J. Biol. Chem.* **1970**, *245*, 2998-3003.
- (190) Miller, L. M.; Chance, M. R. *Biochemistry* **1995**, *34*, 10170-10179.
- (191) Lloyd, E.; Hildebrand, D. P.; Tu, K. M.; Mauk, A. G. J. Am. Chem. Soc. 1995, 117, 6434-6438.
- (192) Nishihara, Y.; Sakakura, M.; Kimura, Y.; Terazima, M. *J. Am. Chem. Soc.* **2004**, *126*, 11877-11888.
- (193) Sorrell, T. N.; Martin, P. K.; Bowden, E. F. *J. Am. Chem. Soc.* **1989**, *111*, 766-767.
- (194) Carver, T. E.; Rohlfs, R. J.; Olson, J. S.; Gibson, Q. H.; Blackmore, R. S.; Springer, B. A.; Sligar, S. G. *J. Biol. Chem.* **1990**, *265*, 20007-20020.
- (195) Pakrasi, H.; De Ciechi, P.; Whitmarsh, J. *EMBO J.* **1991**, *10*, 1619-1627.
- (196) Adachi, S.; Nagano, S.; Watanabe, Y.; Ishimori, K.; Morishima, I. *Biochem. Biophys. Res. Commun.* **1991**, *180*, 138-144.
- (197) Van Dyke, B. R.; Bakan, D. A.; Glover, K. A. M.; Hegenauer, J. C.; Saltman, P.; Springer, B. A.; Sligar, S. G. *Proc. Natl. Acad. Sci. U. S. A.* 1992, 89, 8016-8019.
- (198) Adachi, S.; Nagano, S.; Ishimori, K.; Watanabe, Y.; Morishima, I.; Egawa, T.; Kitagawa, T.; Makino, R. *Biochemistry* **1993**, 32, 241-252.
- (199) Smulevich, G.; Hu, S.; Rodgers, K. R.; Goodin, D. B.; Smith, K. M.; Spiro, T. G. *Biospectroscopy* **1996**, *2*, 365-376.
- (200) Ozaki, S.-i.; Roach, M. P.; Matsui, T.; Watanabe, Y. *Acc. Chem. Res.* **2001**, *34*, 818-825.
- (201) Smulevich, G. Physical Chemistry 2006, Proceedings of the International Conference on Fundamental and Applied Aspects of Physical Chemistry, 8th, Belgrade, Serbia, Sept. 26-29, 2006 2006, 1, 31-37.

- (202) Hase, C. C.; Barquera, B. Biochim. Biophys. Acta 2001, 1505, 169-178.
- (203) Miller, C. J.; Drasar, B. S.; Feachem, R. G. J. Hyg. 1984, 93, 475-495.
- (204) Turk, K.; Puhar, A.; Neese, F.; Bill, E.; Fritz, G.; Steuber, J. *J. Biol. Chem.* **2004**, *279*, 21349-21355.
- (205) Juarez, O.; Morgan, J. E.; Barquera, B. *J. Biol. Chem.* **2009**, *284*, 8963-8972.
- (206) Bogachev, A. V.; Bertsova, Y. V.; Aitio, O.; Permi, P.; Verkhovsky, M. I. *Biochemistry* **2007**, *46*, 10186-10191.
- (207) Barquera, B.; Zhou, W.; Morgan, J. E.; Gennis, R. B. *Proc. Natl. Acad. Sci. U. S. A.* **2002**, *99*, 10322-10324.
- (208) Barquera, B.; Hellwig, P.; Zhou, W.; Morgan, J. E.; Hase, C. C.; Gosink, K. K.; Nilges, M.; Bruesehoff, P. J.; Roth, A.; Lancaster, C. R. D.; Gennis, R. B. *Biochemistry* **2002**, *41*, 3781-3789.

## **CHAPTER 2**

## **EXPERIMENTAL METHODS**

## 2.1 Electrode Materials

## 2.1.1 Boron-Doped Diamond

The diamond thin-film electrode was deposited by microwave-assisted chemical vapor deposition (1.5 kW, 2.54 GHz, Astex, Inc., Lowell, MA).<sup>1</sup> The diagram of a typical reactor is shown in Figure 2.1.

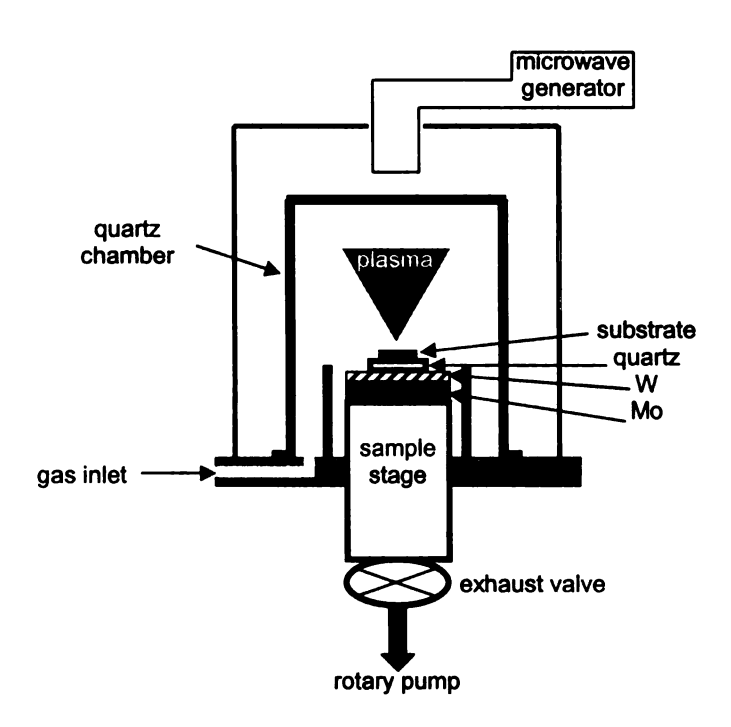


**Figure 2.1** A diagram of a microwave plasma-assisted CVD reactor used to grow boron-doped diamond thin-film electrodes.

All source gases were ultrahigh purity (99.999%) grade (CH<sub>4</sub> and H<sub>2</sub> from AGA Specialty Gas, Cleveland, OH; Ar from BOC Group, Inc., Murray Hill, NJ; 0.1% B<sub>2</sub>H<sub>6</sub> diluted in H<sub>2</sub> from Matheson Gas Products, Inc.). The gases were introduced into the chamber at controlled rates regulated by mass flow controllers. The microwave plasma was then ignited inside a quartz cavity with the flowing source gas mixture. The plasma contains the reactive species important for growth. The pressure of the chamber was regulated using a throttle exhaust valve in series with a rotary pump.

Before growth, the silicon substrate was mechanically scratched for 5 min on a felt polishing pad using a 100 nm diameter diamond powder (Diamond Innovations, Worthington, OH) suspended in ultrapure water. The scratched substrate was then ultrasonically cleaned for 5 min each in ultrapure water, 2-propanol, acetone, 2-propanol, and ultrapure water to remove polishing debris from the surface, partially from the scratches or striations. The substrate was then dried and examined under an Olympus BX60M optical microscope (Olympus America, Inc.) for cleanliness. Embedded diamond powder particles as well as the scratching defects serve as the initial nucleation sites for diamond growth. For the quartz substrate, it was scratched similarly as the silicon substrate using a 100 nm diameter diamond (Diamond Innovations, Worthington, OH) / water suspension prior to diamond deposition, but on a UltraPrep<sup>TM</sup> diamond lapping film disc (Buehler, Lake Bluff, IL). The cleaning steps were the same as those for the silicon substrate.

## 2.1.1.1 Ultrananocrystalline and Microcrystalline Boron-Doped Diamond Electrodes (UNCD and MCD)

UNCD and MCD thin films (not optically transparent) were deposited on highly conductive p-type Si (100) substrates ( $\sim 10^{-3} \Omega$ -cm, 0.05 cm thick × 1 cm<sup>2</sup> area, Virginia Semiconductor, Inc., Fredericksburg, VA). The UNCD films were deposited using gas flow rates of 1, 94, 5 sccm for  $CH_4$ , Ar,  $H_2$ , respectively. Deposition was accomplished using a power of 800 W, a system pressure of 140 Torr, a substrate temperature of ~750 °C and a deposition time of 2 h. The MCD films were deposited using a 0.5% CH<sub>4</sub>/H<sub>2</sub> (v/v) source gas mixture, a total gas flow of 200 sccm, 1 kW of microwave power, a system pressure of 45 Torr, a substrate temperature of ~750 °C and a growth time of 10 h. Both the UNCD and MCD films were boron-doped during deposition by adding 10 ppm B<sub>2</sub>H<sub>6</sub> to the source gas mixture. The specific deposition conditions used for growth of each diamond type are listed in Table 2.1. Following the deposition, the CH₄ and B₂H<sub>6</sub> gas flows were stopped, and the films remained exposed to the Ar/H<sub>2</sub> (UNCD) or H<sub>2</sub> (MCD) plasma for an additional 10 min. The plasma power and pressure were slowly reduced over a 15 min period to cool the samples in the presence of atomic hydrogen to a temperature below 300 °C. Post growth annealing in atomic hydrogen is essential for etching away adventitious nondiamond carbon impurity, minimizing dangling bonds, and ensuring full hydrogen termination. The plasma power was then turned off and the films were cooled to room temperature under a flow of Ar/H<sub>2</sub> (UNCD) or H<sub>2</sub> (MCD). Both film types had a nominal boron dopant concentration in the high  $10^{19}$  to low  $10^{20}$  B/cm<sup>3</sup> range, and a film resistivity of ~0.01  $\Omega$ -cm, or less.

**Table 2.1** Growth conditions for UNCD and MCD thin films deposited on *p-type* Si.

	UNCD	MCD
Gas Mixture	Ar/H <sub>2</sub> /CH <sub>4</sub> /B <sub>2</sub> H <sub>6</sub>	CH <sub>4</sub> /H <sub>2</sub> /B <sub>2</sub> H <sub>6</sub>
<b>Total Gas Flow</b>	100 sccm	200 sccm
<b>Methane Concentration</b>	1% CH₄	0.5% CH₄
Dopant	10 ppm B₂H <sub>6</sub>	10 ppm B <sub>2</sub> H <sub>6</sub>
Microwave Power	800 W	1000 W
<b>Chamber Pressure</b>	140 Torr	45 Torr
Substrate Temperature	~750°C	~750°C
Growth Time	2 h	10 h

After growth, the diamond films were chemically cleaned to remove adventitious metal and sp²-bonded nondiamond carbon impurities from the surface. A two-step procedure was employed: (i) exposure to warm 3:1 HCI/HNO<sub>3</sub> (v/v) for 30 min followed by a rinse with ultrapure water and (ii) exposure to warm 30% hydrogen peroxide (CCI) for 30 min followed by a rinse with ultrapure water. The acid oxidatively removes metallic impurity while the hydrogen peroxide effectively removes nondiamond sp² carbon impurity. These chemical treatments introduce surface carbon-oxygen functionalities, and such a surface is referred to as oxygen-terminated. To regenerate the hydrogen-terminated surface, the diamond films were placed back into the CVD reactor for a 30-min hydrogen-plasma treatment. The conditions were as follows: a microwave power of 1000 W, a system pressure of 35 torr, and hydrogen gas

flow of 200 sccm. The films were slowly cooled in atomic hydrogen, as described above, over a 15-min period.

# 2.1.1.2 UV-Vis Transparent Boron-Doped Diamond Electrode (Diamond/Quartz OTE)

The UV-Vis optically transparent diamond thin film was deposited on quartz using a CH<sub>4</sub>/H<sub>2</sub>/B<sub>2</sub>H<sub>6</sub> source gas mixture consisting of 0.5% CH<sub>4</sub>/H<sub>2</sub> with 10 ppm B<sub>2</sub>H<sub>6</sub> added for boron doping, a total gas flow of 100 sccm, a power of 600 W, a system pressure of 45 torr, a substrate temperature of ~450 °C (roughly estimated with an optical pyrometer), and a growth time of 1 h. The growth conditions are listed in Table 2.2. At the end of the deposition period, the film remained exposed to a hydrogen plasma for an additional 10 min at 600 W and 45 Torr. The plasma power and pressure were then slowly reduced over a 15min period to cool the samples in the presence of atomic hydrogen. The 1-h film was estimated to be 500 nm thick with an electrical resistivity of ~0.026 Ω-cm and an optical transparency of 45-60% between 300 and 800 nm.<sup>2</sup> The diamond film received no pretreatment prior to use other than a 20 min soak in distilled isopropanol. The current flow was laterally through the film with an ohmic contact made along the edge of the electrode. To improve the conductivity, a metallic layer (50Å Ti, 200Å Au) was deposited on the surface of the film outside the electrochemical cavity.

**Table 2.2** Growth conditions for UV-Vis optically transparent diamond electrode.

Diamond/quartz OTE		
Gas Mixture	CH <sub>4</sub> /H <sub>2</sub> /B <sub>2</sub> H <sub>6</sub>	
<b>Total Gas Flow</b>	100 sccm	
<b>Methane Concentration</b>	0.5% CH₄	
Dopant	10 ppm B₂H <sub>6</sub>	
Microwave Power	600 W	
Chamber Pressure	45 Torr	
Substrate Temperature	~450°C	
<b>Growth Time</b>	1 h	

## 2.1.2 Glassy Carbon

The glassy carbon electrode (Tokai, GC-20) was prepared by polishing to a mirror-like finish with successively smaller grades of alumina powder slurried in ultrapure water (1.0, 0.3, and 0.05  $\mu$ m). The polishing was carried out by hand on individual felt polishing pads. After each polishing step, the electrode was rinsed thoroughly with ultrapure water and then ultrasonically cleaned in the same medium for 20 min to remove polishing debris and clean the surface.

## 2.1.3 Gold Minigrid

The gold minigrid electrode (Precision Eforming LLC, MG44, 55% transmission) was modified prior to use by oxidizing in a freshly prepared concentrated  $H_2SO_4$ :30%  $H_2O_2$  (3:1 v/v) solution for 30 min followed by incubation in 2 mM cysteamine for 2 h.

#### 2.2 Cyclic Voltammetric Experiments

All electrochemical measurements were performed at room temperature in a single compartment glass cell using a computer-controlled potentiostat (Model 900, CH Instruments, Inc., Austin, TX). A standard three-electrode configuration was employed, as shown in Figure 2.2.<sup>3</sup>

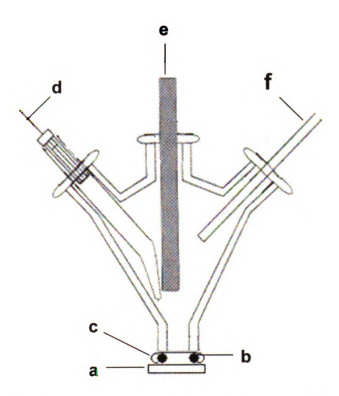


Figure 2.2 Design of the single-compartment, three-electrode electrochemical cell with (a) the diamond film working electrode, (b) o-ring seal, (c) rubber spacer (and nickel foil), (d) reference electrode inside a glass capillary tube with a cracked tip, (e) carbon rod counter electrode, and (f) input for nitrogen purge gas.

The electrochemical cell was housed inside a grounded Faraday cage for electrical shielding. The working electrode was clamped against a clean Viton® oring (*i.d.* 0.5 cm) at the bottom of the cell to confine the solution. The o-ring was sonicated for 10 min in ultrapure water, rinsed with distilled isopropyl alcohol

(IPA), and dried under a steam of N<sub>2</sub> before use. Electrical contact was made to the diamond working electrode by scratching the backside of the Si substrate with a diamond scribe, and then cleaning and coating the area with graphite from a pencil to ensure good ohmic contact with the copper current-collector plate. The geometric area of the electrode exposed to the solution was 0.2 cm<sup>2</sup>. The electrode was cleaned prior to use by soaking in IPA for 20 min.<sup>4, 5</sup> After decanting the IPA and rinsing thoroughly with distilled water, the cell was filled with the electrolyte solution of interest. A silver/silver chloride reference electrode (4 M KCl saturated with AgCl, E<sup>o</sup> = -45 mV vs. SCE) was used, which was placed inside a cracked–glass capillary filled with 1 M KCl and positioned in close proximity to the working electrode. A large area carbon rod served as the counter electrode and was positioned normal to the working electrode.

## 2.3 Electrochemical Kinetics

The apparent heterogeneous electron-transfer rate constant,  $k_{app}^o$  was determined from the scan rate dependence of  $\Delta E_p$  using Nicholson's theoretical method.<sup>6</sup> According to the theory,  $\Delta E_p$  for an electrochemical reaction is dependent on the scan rate (v, V/s), transfer coefficient ( $\alpha$ ) and heterogeneous electron-transfer rate constant ( $k_{app}^o$ , cm/s). The behavior of quasireversible reactions can be described by the equation:

$$\psi = \frac{\left(\frac{D_O}{D_R}\right)^{\alpha/2} k_{app}^{o}}{\left(\pi D_O f v\right)^{1/2}}$$

Where  $D_O$  and  $D_R$  are the diffusion coefficients of the oxidized and reduced species (cm²/s), respectively, f is the Faraday constant divided by the ideal gas constant and temperature (F/RT), and  $\Psi$  is a dimensionless parameter. From the relationship between  $\Psi$  and  $\Delta E_p$ ,  $k_{app}^O$  can be calculated from the above equation at different scan rates. In this research,  $\Delta E_p$  varied over the scan rate range tested and the apparent heterogeneous electron-transfer rate constant,  $k_{app}^O$ , was statistically determined from data at several scan rates.

## 2.4 X-ray Photoelectron Spectroscopy (XPS)

XPS was used to determine the oxygen and carbon atomic ratios (O/C) on diamond surface. The SPS spectra were obtained using a Physical Electronics PHI 5400 XPS spectrometer with a Mg X-ray source. A take-off angle of 45 degrees was used for all measurements at a base pressure less than 5 x 10<sup>-9</sup> Torr. Software provided with the instrument was used to deconvolute the peaks and integrate peak areas. The relative atomic percentage of each element was estimated from peak areas using atomic sensitivity factors specific for the PHI 5400 instrument.

#### 2.5 Spectroelectrochemical Measurements

#### 2.5.1 Thin-Layer Spectroelectrochemical Cell

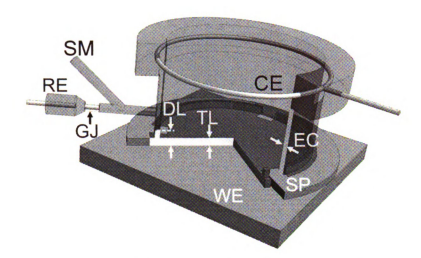


Figure 2.3 Diagram of the thin-layer transmission spectroelectrochemical cell. A thin layer (TL) is formed between the working electrode (WE) and the transmission window (not shown) and its thickness is determined by the spacer (SP). The thin layer is connected to the Pt counter electrode (CE) via electrolyte capillary (EC) between the transmission window and outer cell body. A miniature Ag/AgCI reference electrode (RE) is also connected to the electrolyte capillary via a cracked glass junction (GJ). Reference electrode capillary is also used for loading sample (SM), which is exhausted via a similar capillary on the opposite side (not shown).

The new transmission thin-layer cell design (Figure 2.3) builds upon an original design (Mantelle *et al.*<sup>10</sup>) with major modifications to meet desired criteria for thin-layer cells. The electrochemical volume of the cell is defined by the narrow space between two planes – typically a working electrode (front) and a transmission window (back; 9 mm dia. x 5 mm, CaF<sub>2</sub> used in this work) separated by a Kapton<sup>®</sup> polyimide film spacer of the desired thickness (7.5 to 75 μm). A platinum wire ring outside the sealed cavity was used to establish electric contact with the working electrode surface. The cell was equipped with a

miniature Ag/AgCl reference electrode for aqueous solution measurements. The reference electrode was connected to the side of the back window between the working and counter electrodes via a cracked glass junction and a 1 mm dia. capillary. Another Pt wire was employed as the counter electrode. It was either located in a 1x1 mm groove encircling the back transmission window or coiled in a separate compartment that was connected to that groove through a PEEK frit (1.5 mm dia.).

For aerobic measurements, the analyte solution was loaded into the electrochemical cavity by placing a small sample volume (5-10  $\mu$ L) in the center of the working electrode immediately prior to assembling the cell. Then the volume around the window was filled with the supporting electrolyte. For anaerobic measurements, the cell was pre-filled with electrolyte solution and assembled aerobically. The cell was then deoxygenated by injecting 1-2 mL of an oxygen-free buffer using a syringe via a capillary port, which opened onto the sides of the back window close to the working electrode. Excess solution was drained via another port located at a diametrically opposing sides of the window. Finally, several volumes of oxygen-free analyte were then injected into the cavity and the cell was sealed.

## 2.5.2 Potential Step Method

Spectroelectrochemical measurements were made by stepping the potential from a value where the redox system is stable (e.g., reduced form) to

values at which a redox reaction (e.g., oxidation) occurs. An absorbance spectrum was collected at each potential after an equilibration period (usually 1 min), as depicted in Figure 2.4.

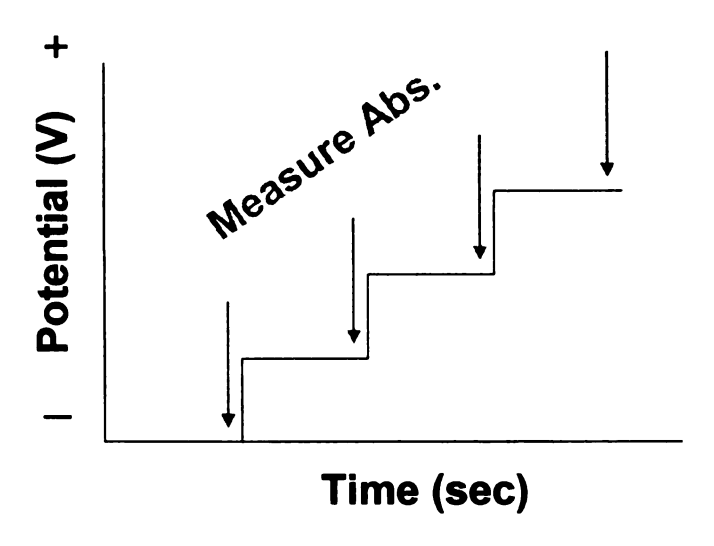


**Figure 2.4** Scheme for measuring the steady-state absorbance of a redox analyte as a function of the potential in a spectroelectrochemical measurement. An absorbance spectrum was recorded at each potential, as indicated by the arrows.

Absorbance difference spectra were then generated by subtracting the spectrum for the unreacted redox system from the spectrum obtained at each potential. Small absorbance changes that occur during the transition between redox states are not always detectable in the individual spectra. However, they are in difference absorbance spectra. Figure 2.5 shows an idealized difference spectrum with the negative-going bands reflective of the initial state, A, and positive-going bands reflective of product state B.<sup>11</sup>

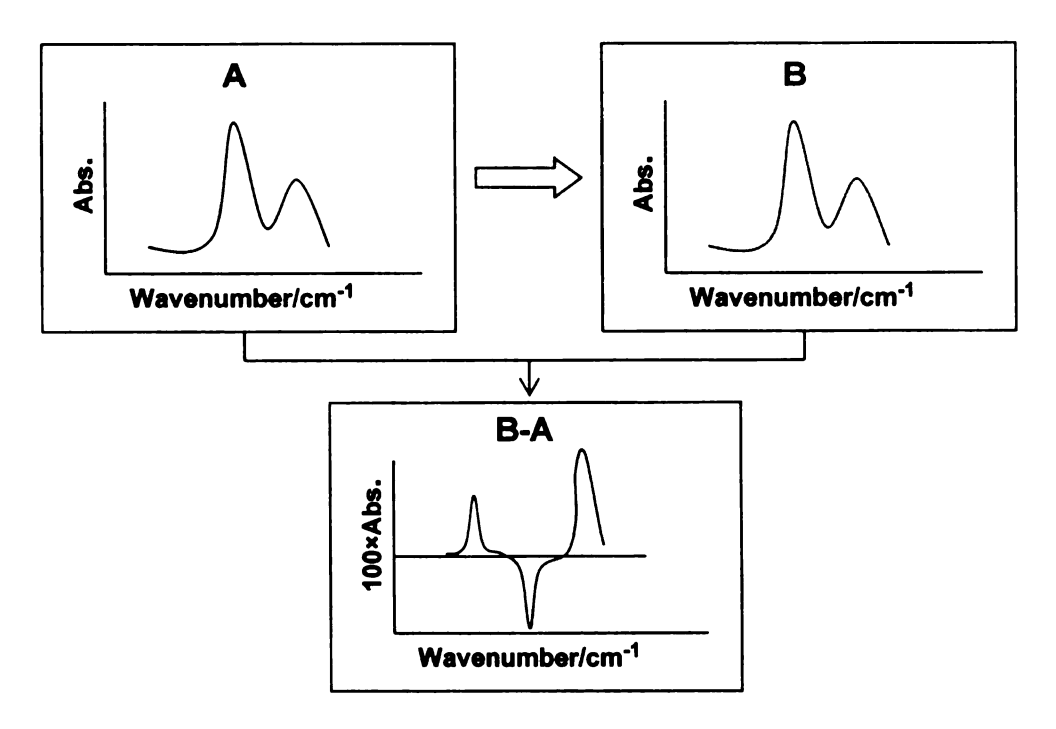


**Figure 2.5** Principle of difference absorbance spectroscopy. The difference spectrum B-A is generated by subtracting spectrum of initial state A from spectrum of product state B.<sup>11</sup>

For redox proteins with multiple cofactors, sufficient time (~10-20 min) should be given at each potential before measuring the spectrum. Due to the length of such an experiment, it is necessary to discriminate reversible electrochemical response from irreversible background changes (e.g., photoreactions). To accomplish this, potential step method was revised. Absorbance spectra at a reference potential were recorded before and after each potential step after an equilibration period (e.g., 20 min), as depicted in Figure 2.6. The difference absorbance spectrum is generated by subtracting the average spectrum at the reference potential right before and after each potential step.

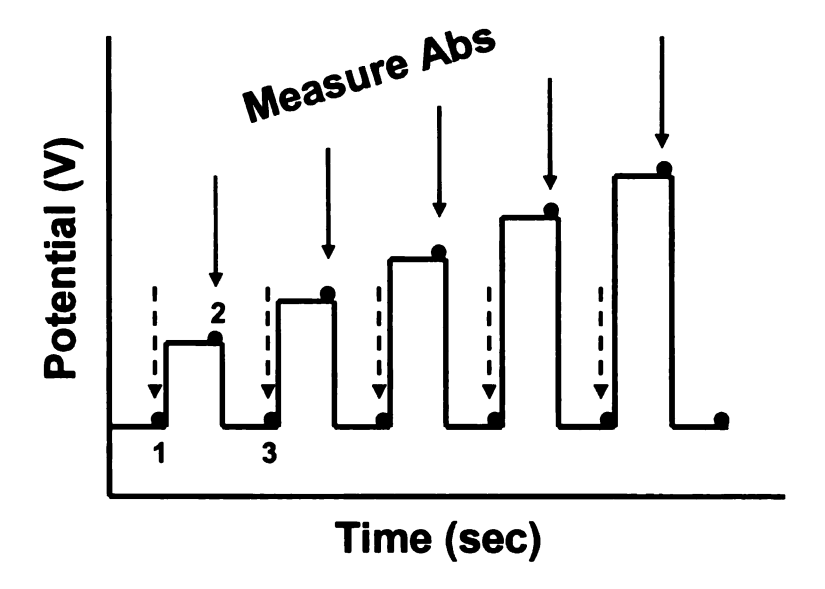


**Figure 2.6** Potential-time profile for potential step studies of Na<sup>+</sup>-NQR. Absorbance spectra at the reference potential (dashed arrow) were recorded before and after each potential step (solid arrow). The difference absorbance spectrum was generated by subtracting the average of the absorbance spectra at reference potential from absorbance spectrum at each potential (e.g.,  $\Delta A = A_2 - (A_1 + A_3)/2$ ).

## 2.5.3 UV-Vis Spectroelectrochemical Measurements

The electrochemical measurements were performed at room temperature using a computer-controlled potentiostat (Model 760B, CH Instruments, Inc., Austin, TX). All potentials are reported with respect to the Ag/AgCl electrode (3 M KCl) unless otherwise specified. For chronoamperometric measurements, UV-Vis spectra were recorded continuously at 0.3-s intervals using a Hewlett Packard 8453 diode array spectrophotometer (Agilent Technologies, Santa Clara, CA). The start of the optical and amperometric measurement was electronically synchronized. For spectroelectrochemical studies of Na<sup>†</sup>-NQR, UV-Vis measurements were performed using a custom-built UV-Vis spectrophotometer

with a CCD detector. This setup, with a low intensity probe light minimized photoinduced damage in the thin layer.

## 2.6 Global Regression Analysis

Global nonlinear regression analysis was employed to resolve redox potentials and spectra of multiple redox centers with similar potentials and spectral signatures. Several model spectra are first generated with various intensities and shapes at different wavelength. Second, Nernst functions are used to describe the relationship of several variables: applied potential (E), redox potential (E<sub>m</sub>), number of electrons transferred (n), and temperature (T). Then a model 3D surface can be created by combining the model spectra and Nernst functions. The spectroelectrochemical data were simulated with the modeled surface. Specifically, in this research, several models of three to five redox transitions involving one to three transferred electrons were applied to the high resolution spectroelectrochemical data.

#### 2.7 Chemicals

All chemicals were reagent grade quality, or better, and were used without further purification. Solutions of potassium ferrocyanide (Aldrich) in 1 M potassium chloride (CCI) were prepared fresh daily with ultrapure water (~18  $M\Omega$ -cm) from a commercial water purification system (Barnstead E-pure).

Stock solutions of cytochrome c (in 0.3 M NaCl, 10 mM Tris-HCl buffer, pH 7) were prepared by chromatographically purifying and concentrating horse heart cytochrome c (Sigma Aldrich Chemical Co.,). 12, 13 Cytochrome c concentrations were determined spectrophotometrically at 550 nm from the difference in the absorbance of the ferrous and ferric forms of the protein using Δε<sub>550</sub>=21 mM<sup>-1</sup>cm<sup>-1</sup> <sup>1</sup>. <sup>14, 15</sup> Ferricytochrome c was reduced by adding a non-quantitative small amount of sodium dithionite. The Tris-HCI buffer can be exchanged by repeated dilution and centrifugations using an Amicon<sup>®</sup> Ultra-15 Centrifugal filter device (Millipore). The phosphate buffer solutions were prepared by mixing appropriate amounts of K<sub>2</sub>HPO<sub>4</sub> (CCI) and KH<sub>2</sub>PO<sub>4</sub> (Spectrum) to obtain the desired concentration and pH. It is worth mentioning that the glassware and o-rings exposed to the cytochrome c solutions were rinsed with 0.1 M HCl solution before the final cleaning step. For cytochrome c-cyanide measurements, a small aliquot of stock KCN solution was added to the cytochrome c solution and pre-incubated for 30 min prior to the experiment.

Horse heart myoglobin (metMb) (Sigma) was dissolved in 0.1 M sodium phosphate buffer solution (pH 7) and centrifuged for 10 min to remove undissolved material. The supernatant was then purified on a Sephadex G-75 column (100 mm × 15 mm). The concentration of metMb was determined spectroscopically, either by reducing an aliquot of metMb with solid sodium dithionite to the ferrous form deoxyMb ( $\varepsilon_{435}$ =121 mM<sup>-1</sup>cm<sup>-1</sup>) or by converting deoxyMb further to the CO-bound form MbCO ( $\varepsilon_{424}$ =207 mM<sup>-1</sup>cm<sup>-1</sup>,  $\varepsilon_{540}$ =15.4 mM<sup>-1</sup>

 $^{1}$ cm $^{-1}$  and  $\epsilon_{579}$ =13.9 mM $^{-1}$ cm $^{-1}$ ). The metMb sample was degassed 6-8 cycles between Ar gas and mild vacuum while stirring. MetMb was reduced to deoxyMb with a minimal amount of sodium dithionite solution freshly prepared with oxygenfree water with the reduction being monitored spectroscopically. Gas-tight syringes, flushed with Ar gas/diluted sodium dithionite solution, were used in subsequent sample handling.

The stock solution of Na<sup>+</sup>-translocating NADH:quinone oxidoreductase (Na<sup>+</sup>-NQR) in 50 mM sodium phosphate buffer (or 50 mM Tris buffer) (pH 8), 100 mM NaCl, 1 mM EDTA, 5% glycerol and 0.05% dodecylmaltoside (DDM) was received from the Barquera group. <sup>16</sup> It was diluted to the desired protein and Na<sup>+</sup> concentrations for the electrochemical studies. EDTA helps to sequester metal ion impurities in solution; glycerol is used to minimize damage by ice crystals in frozen solution; and DDM is used to extract the protein from the membrane and helps protein solubilization.

All glassware and storage bottles were cleaned in a three-step manner: KOH/ethanol bath, alconox/ultrapure water solution, and ultrapure water rinse. The cleaned glassware was then dried in an oven at ~50 °C.

### 2.8 References

- (1) Swain, G. M. In *Electroanalytical Chemistry*; Bard, A. J., Rubinstein, I., Eds.; Marcel Dekker, 2004; Vol. 22, pp 182-277.
- (2) Stotter, J.; Zak, J.; Behler, Z.; Show, Y.; Swain, G. M. *Anal. Chem.* **2002**, 74, 5924-5930.
- (3) Granger, M. C.; Witek, M.; Xu, J.; Wang, J.; Hupert, M.; Hanks, A.; Koppang, M. D.; Butler, J. E.; Lucazeau, G.; Mermoux, M.; Strojek, J. W.; Swain, G. M. *Anal. Chem.* **2000**, *72*, 3793-3804.
- (4) Show, Y.; Witek, M. A.; Sonthalia, P.; Swain, G. M. *Chem. Mater.* **2003**, *15*, 879-888.
- (5) Ranganathan, S.; Kuo, T.-C.; McCreery, R. L. *Anal. Chem.* **1999**, *71*, 3574-3580.
- (6) Nicholson, R. S. Anal. Chem. 1965, 37, 1351-1355.
- (7) Yagi, I.; Notsu, H.; Kondo, T.; Tryk, D. A.; Fujishima, A. *J. Electroanal. Chem.* **1999**, *473*, 173-178.
- (8) Armstrong, F. A.; Hill, H. A. O.; Walton, N. J. *Acc. Chem. Res.* **1988**, *21*, 407-413.
- (9) Mori, Y.; Kawarada, H.; Hiraki, A. Appl. Phys. Lett. 1991, 58, 940-941.
- (10) Moss, D.; Nabedryk, E.; Breton, J.; Mantele, W. *Eur. J. Biochem.* **1990**, *187*, 565-572.
- (11) Zscherp, C.; Barth, A. *Biochemistry* **2001**, *40*, 1875-1883.
- (12) Brautigan, D. L.; Ferguson-Miller, S.; Margoliash, E. *J. Biol. Chem.* **1978**, 253, 130-139.
- (13) Brautigan, D. L.; Ferguson-Miller, S.; Margoliash, E.; Sidney, F.; Lester, P. *Methods Enzymol.* **1978**, *53*, 128-164.
- (14) Massey, V. Biochim. Biophys. Acta 1959, 34, 255-256.
- (15) Van Buuren, K. J. H.; Van Gelder, B. F.; Wilting, J.; Braams, R. *Biochim. Biophys. Acta* **1974**, 333, 421-429.
- (16) Barquera, B.; Zhou, W.; Morgan, J. E.; Gennis, R. B. *Proc. Natl. Acad. Sci. U. S. A.* **2002**, *99*, 10322-10324.

## **CHAPTER 3**

# C AT BORON-DOPED DIAMOND ELECTRODES

## 3.1 Introduction

## 3.1.1 Electrochemical Studies of Cytochrome c

Electron-transfer reactions play an important role in many biological processes. Cytochrome c is a small (12,384 Da), water-soluble protein that functions as an electron carrier in the final step of electron transport during oxidative phosphorylation. It has been studied extensively as a model system for biological electron transfer. It contains a c-type heme prosthetic group, which is covalently linked to the polypeptide chain via thioether bonds through two cysteine residues. The structure of the heme c is shown in Figure 3.1. The Fe atom of heme c is also bonded to two axial ligands (histidine and methionine), above and below the heme plane, in addition to the four nitrogen atoms of the planar porphyrin ring system.

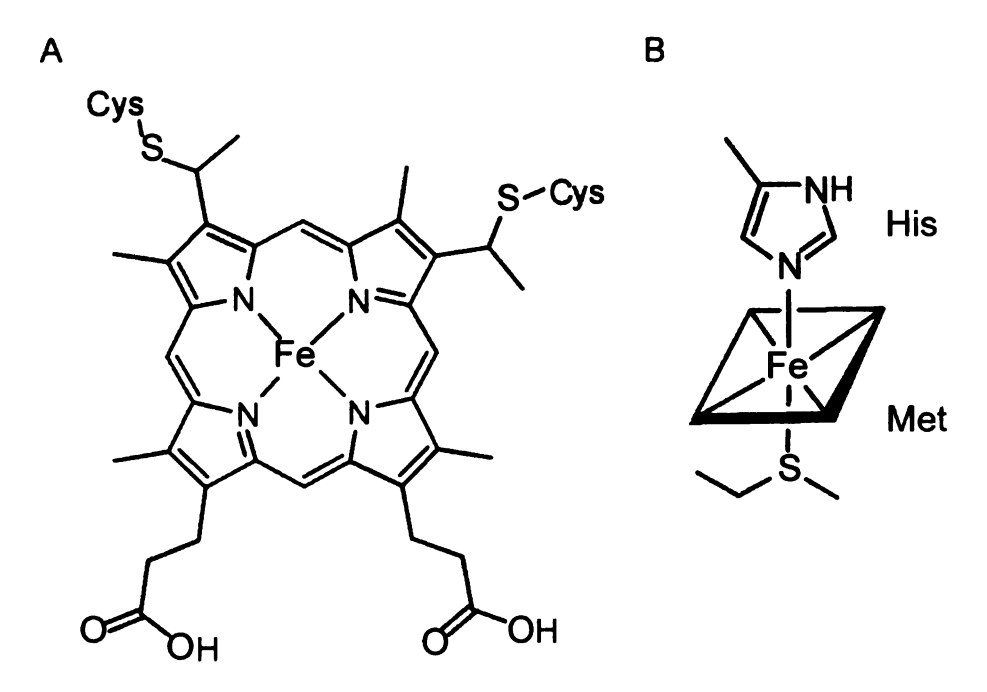


**Figure 3.1** Heme c structure of cytochrome c. (A) Planar porphyrin ring system; (B) heme Fe is also bonded to histidine (His) and methionine (Met) axial ligands.

The heme group is largely embedded within the hydrophobic interior of the globular polypeptide, leaving an edge exposed to solvent. The Fe readily accepts and releases an electron and the electron transfer is believed to occur at the solvent-exposed edge of the heme by an outer-sphere mechanism, which is only 0.6% of the total surface area of the molecule. The large dipole moment of cytochrome c and the electrostatic field of its physiological redox partners cause the heme to be guided into the proper orientation for effective electron transfer. c

The importance of cytochrome c in the respiratory chain of mitochondria has inspired biologists and biochemists to elucidate the mechanism of interprotein electron-transfer process.<sup>6</sup> The first reports on direct electron transfer between cytochrome c and a solid electrode appeared in 1977. Eddowes and Hill

demonstrated, by cyclic voltammetry, quasi-reversible electron transfer at a 4,4'-bipyridyl-modified gold electrode.<sup>7</sup> At the same time, Yeh and Kuwana showed by cyclic voltammetry that direct electron transfer was possible at a tin-doped indium oxide electrode.<sup>8</sup> Since their pioneering work, significant advances in the electrochemistry of redox proteins have been made.

Surface modification with promoters is the most popular method employed for achieving quasi-reversible electrode kinetics. Cytochrome c has been studied using voltammetric methods under diffusion control and in a surface confined state. Numerous chemically-functionalized electrode materials have been used: self-assembled monolayer(SAM)-,9-12 polymer brush-,13 or gold nanoparticles-14, <sup>15</sup> modified gold, single-<sup>16</sup>/multi-<sup>17</sup> walled carbon nanotubes-, fullerene films-<sup>18</sup> or DNA-19 modified glassy carbon, clay-modified pyrolytic graphite, 20 aminenanodiamonds<sup>21</sup> and NHS ester-modified terminated boron-doped nanocrystalline diamond.<sup>22</sup> The modifiers provide specific binding sites for the redox protein and control the spacing between the electrode and the protein (reduce tunneling length), thus facilitating the electron transfer.<sup>23</sup> Kinetic studies at SAM-modified electrodes showed that the presence of carbonyl functionalities facilitates the orientation conducive for a reversible electron transfer between the protein and electrode surface.

Alternatively, other researchers have taken the approach of studying cytochrome c using bare electrodes without promoters. Gold, <sup>24</sup> silver, <sup>25, 26</sup> ITO, <sup>27</sup>.

glassy carbon,<sup>24, 29</sup> graphite,<sup>23, 30</sup> and boron-doped diamond<sup>31, 32</sup> are the most studied bare electrodes. Highly purified protein is required to avoid any contamination of the bare electrode with defunct protein.<sup>33</sup> Armstrong and coworkers reported that the electron-transfer kinetics for cytochrome *c* at the edge plane of pyrolytic graphite are much higher compared to the basal plane due to the high oxygen/carbon (O/C) ratio of the edge plane.<sup>30, 34</sup> In general, two factors seem to be necessary for rapid electron transfer for cytochrome *c* at bare electrodes: (i) a pure cytochrome *c* solution and (ii) electrode pretreatment to produce a clean, hydrophilic surface.<sup>29, 35</sup>

Previously, our group reported a different finding of quasi-reversible, diffusion-controlled voltammetry for cytochrome c at an as-deposited boron-doped ultrananocrystalline diamond thin-film electrode possessing a hydrophobic, hydrogen-terminated surface. Rivas *et al.* also reported immobilization of cytochrome c on Ag electrodes that were coated with a hydrophobic self-assembled monolayer (SAM) n-alkanethiol HS-(CH<sub>2</sub>)<sub>n</sub>-CH<sub>3</sub>. They supposed that hydrophobic interactions with the electrode were important for orienting the protein in such a way as to facilitate electron transfer. Comparing with electrostatically-bound cytochrome c, the hydrophobic interactions lead to the same structural changes of the heme and larger rate constants for conformational transitions. Marken *et al.*, on the other hand, reported direct cytochrome c electrochemistry at boron-doped diamond electrodes after polishing with alumina or cathodic cycling; but no voltammetric response was

detected after anodic cycling.31 This observation was explained in terms of favorable interactions between the pretreated, hydrophilic diamond surface and the reactive region of the cytochrome c molecule. 31 The pretreatment was also proposed to impact fouling resistance to the electrode. Zhou et al. reported direct electrochemistry of covalently immobilized cytochrome c at carboxyl-terminated boron-doped diamond electrodes.<sup>22</sup> The modified electrode showed the ability to electrocatalyze the reduction of hydrogen peroxide.<sup>22</sup> Similarly, Geng et al. designed a sandwich structured SiO<sub>2</sub>/cytochrome c/SiO<sub>2</sub> gel on a boron-doped diamond film electrode for used as an electrochemical nitrite biosensor.<sup>37</sup> More detailed investigation of electrochemistry of cytochrome c at boron-doped diamond electrodes is needed in order to better understand what factors are most important for rapid electron transfer for redox proteins. Specifically, cyclic voltammetric data as a function of the diamond film morphology, surface chemistry and solution pH were obtained and analyzed in order to better understand the redox reaction at diamond electrodes.

## 3.1.2 Oxygen-Terminated Boron-Doped Diamond Electrodes

Boron-doped diamond films are normally deposited under  $H_2$ -rich conditions, so the as-deposited films are typically hydrogen-terminated. The surface can straightforwardly be converted to an oxygen-termination by any one of three methods: (1) chemical oxidation (e.g., hot acid), (2) oxygen plasma treatment, and (3) electrochemical oxidation.<sup>38</sup>

The electrochemical properties of oxygen-terminated diamond electrodes have been studied by Fujishima and coworkers.<sup>39-42</sup> The type of carbon-oxygen functional groups formed can be quite distinct across the surface according to both XPS results and electrochemical response changes after certain chemical treatments. In general, carbonyl (C=O) and ether (C-O-C) groups are formed on a diamond (100) surface,<sup>41, 43</sup> whereas hydroxyl groups (C-OH) are generated on a diamond (111) surface.<sup>44, 45</sup> Figure 3.2 shows the terminal atomic structure for hydrogen-terminated and oxygen-terminated diamond (100) and (111) surfaces.

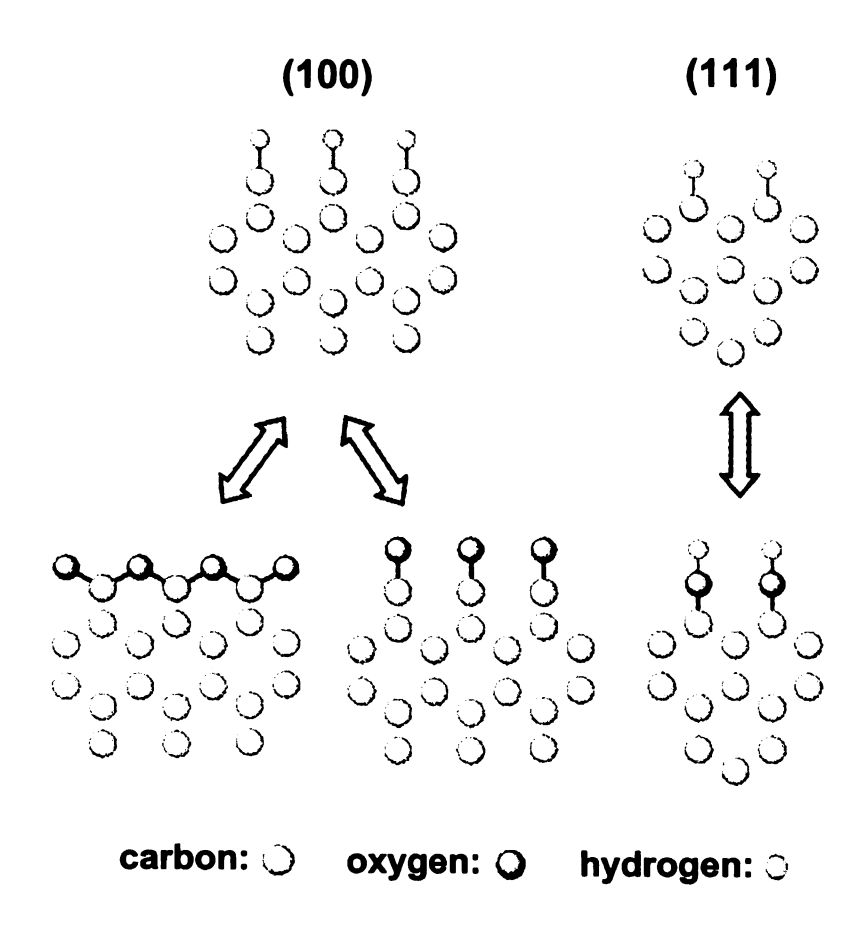


**Figure 3.2** Terminal atomic structure for hydrogen- and oxygen-terminated diamond (100) and (111) surfaces.<sup>46</sup>

Due to the change of surface hydrophobicity, wider working potential windows and larger voltammetric background currents were observed for oxygen-terminated diamond electrodes as compared to hydrogen-terminated electrodes.<sup>39</sup> The Fujishima group also reported that redox analytes with a negative charge exhibit decreased apparent electron-transfer rates at oxygenterminated diamond electrodes, while the apparent electron-transfer rates for redox analytes with positive charge either did not change or were accelerated. An electrostatic explanation was offered such that anionic complexes are repelled from the oxidized surface while cationic complexes are attracted. They proposed that these effects are due to ion-dipole interactions of the charged redox system with either the carbon-hydrogen surface groups, which have dipoles with the positive ends pointing away from the electrode surface, or with the carbon-oxygen groups, which have oppositely oriented dipoles.<sup>42, 47</sup> general, there are two merits of the oxidized diamond surface. First, the electrochemical properties of diamond electrodes are affected by means of electrostatic interactions between the electrode surface and redox charged system. Second, the oxygen-terminated surface can facilitate the introduction of other functional groups. Oxygen-terminated diamond electrodes have been widely used in electroanalysis. 42, 48

In order to understand the electron transfer process between cytochrome c and the diamond electrode, we studied the electrochemical behavior of this protein at boron-doped diamond electrodes. The rate of electron transfer was

investigated by cyclic voltammetry as a function of (i) film morphology (ultrananocrystalline diamond (UNCD) vs. microcrystalline diamond (MCD) thin films; (ii) surface chemistry (oxygen- vs. hydrogen-termination); and (iii) the solution pH.

## 3.2 Results

## 3.2.1 XPS Measurements

X-ray photoelectron spectroscopy (XPS) was used to characterize the elemental composition of the diamond surface. Typical XPS spectra for as deposited, oxygen-terminated (after chemical oxidation) and hydrogen-terminated (after chemical oxidation and then rehydrogenation) UNCD surfaces are shown in Figure 3.3.

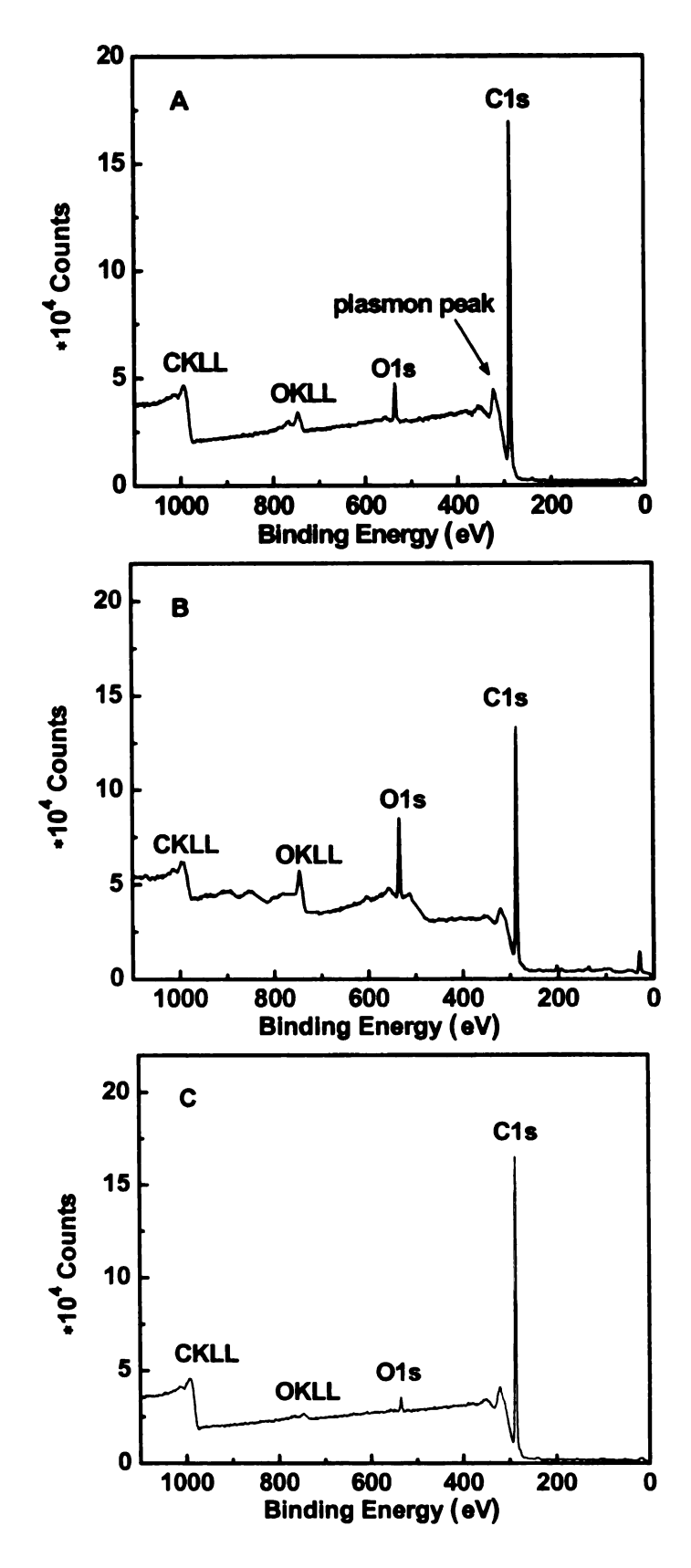


**Figure 3.3** XPS spectra for (A) as-deposited, (B) oxygen-terminated, and (C) hydrogen-terminated UNCD electrode surfaces.

The spectrum for the as-deposited film showed a sharp C 1s peak at 284 eV and a small discernable O 1s peak at 532 eV. The O/C atomic ratio for this sample was determined to be 0.05. The plasmon loss feature (34 eV higher in energy relative to the C 1s peak) results from energy losses of the outgoing photoelectrons due to excitations of the bulk and surface plasmons of diamond.<sup>49</sup> This is a good indication of high purity of the diamond film.<sup>49</sup> No peak corresponding to the excitation of the graphite  $\pi$ - $\pi$ \* plasmon (7 eV higher in energy relative to the C 1s peak) was observed. After chemical oxidation, the O 1s peak intensity increased considerably, indicating greater oxygen coverage. In other words, chemical oxidation introduces oxygen functional groups onto the diamond surface. The O/C value was determined to be 0.17, similar to the reported 0.18 for a diamond electrode treated in an oxygen plasma.<sup>39</sup> The rehydrogenation step converted the electrode surface back to a hydrogentermination surface by removing oxygen functional groups, as indicated by the reduced O/C ratio of 0.02.

After exposure to the cytochrome c solution, the XPS spectrum for the oxidized UNCD electrode showed the appearance of a N 1s peak from the residual cytochrome c on the surface, as shown in Figure 3.4. Similar trends were seen for oxidized MCD. The XPS data for electrodes with different terminations before and after cytochrome c exposure are listed in Table 3.1. It is clear that the nitrogen signal appears after the protein exposure, indicating the existence of absorption of cytochrome c at specific sites.

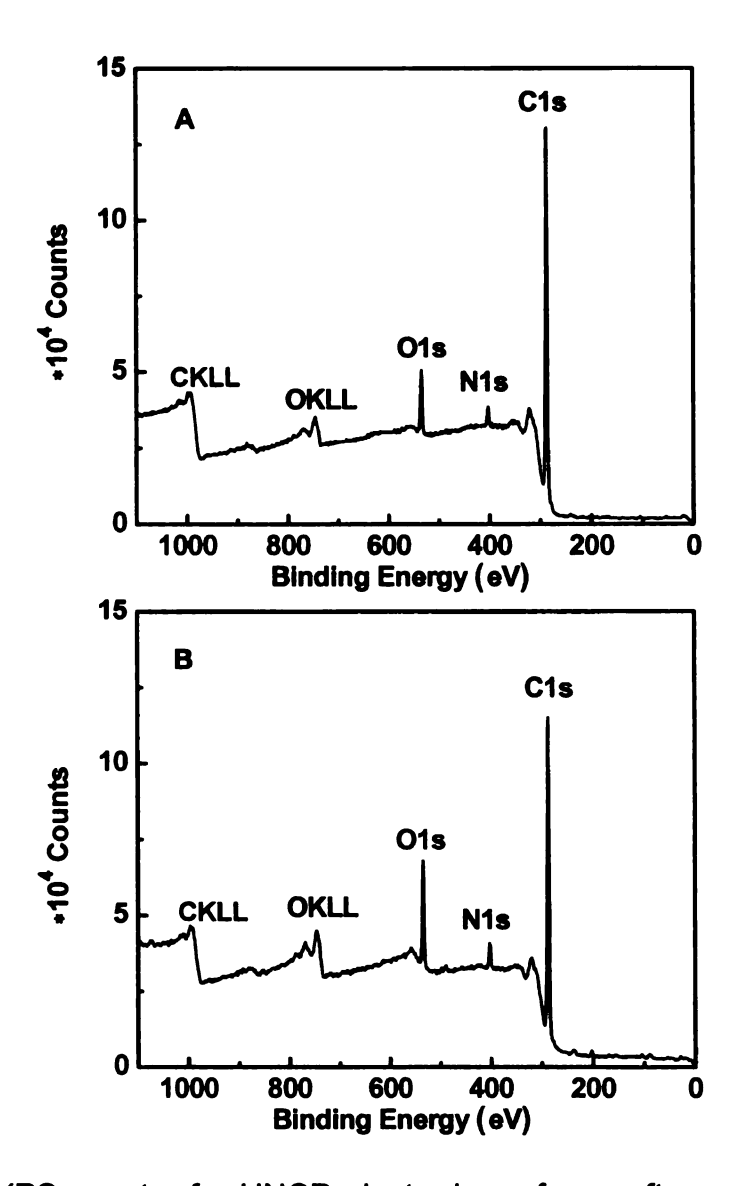


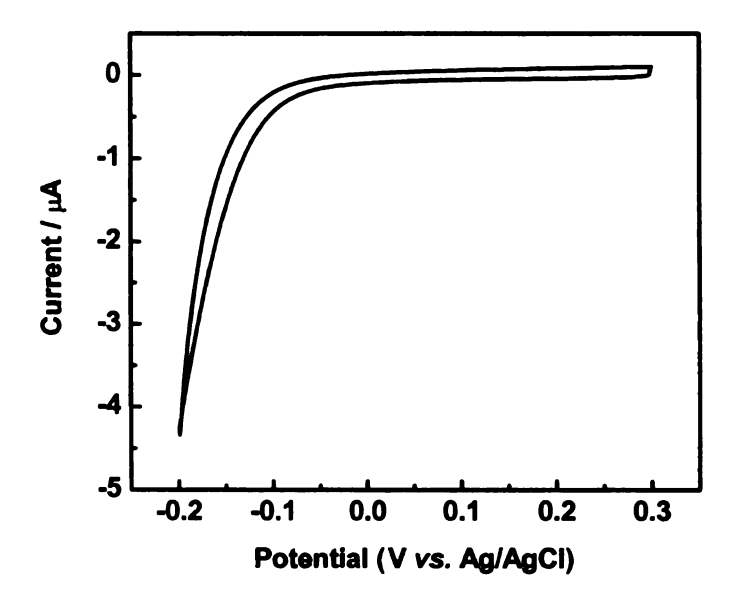
**Figure 3.4** XPS spectra for UNCD electrode surfaces after potential cycling in cytochrome c solution. (A) Hydrogen-terminated surface; (B) oxygen-terminated surface.

**Table 3.1** Summary of the surface composition on various diamond electrode surfaces.

XPS	UNCD				MCD			
	C1s	O1s	N1s	O/C	C1s	O1s	N1s	O/C
As deposited	95.04	4.96		0.05	97.96	2.04		0.02
H-terminated	97.56	2.09		0.02	98.07	1.93		0.02
H-terminated+cyt c	88.76	6.41	3.35		86.96	8.81	3.61	
O-terminated	80.32	13.58		0.17	87.52	10.79		0.12
O-terminated+cyt c	82.30	12.52	4.33		88.73	10.88	4.02	

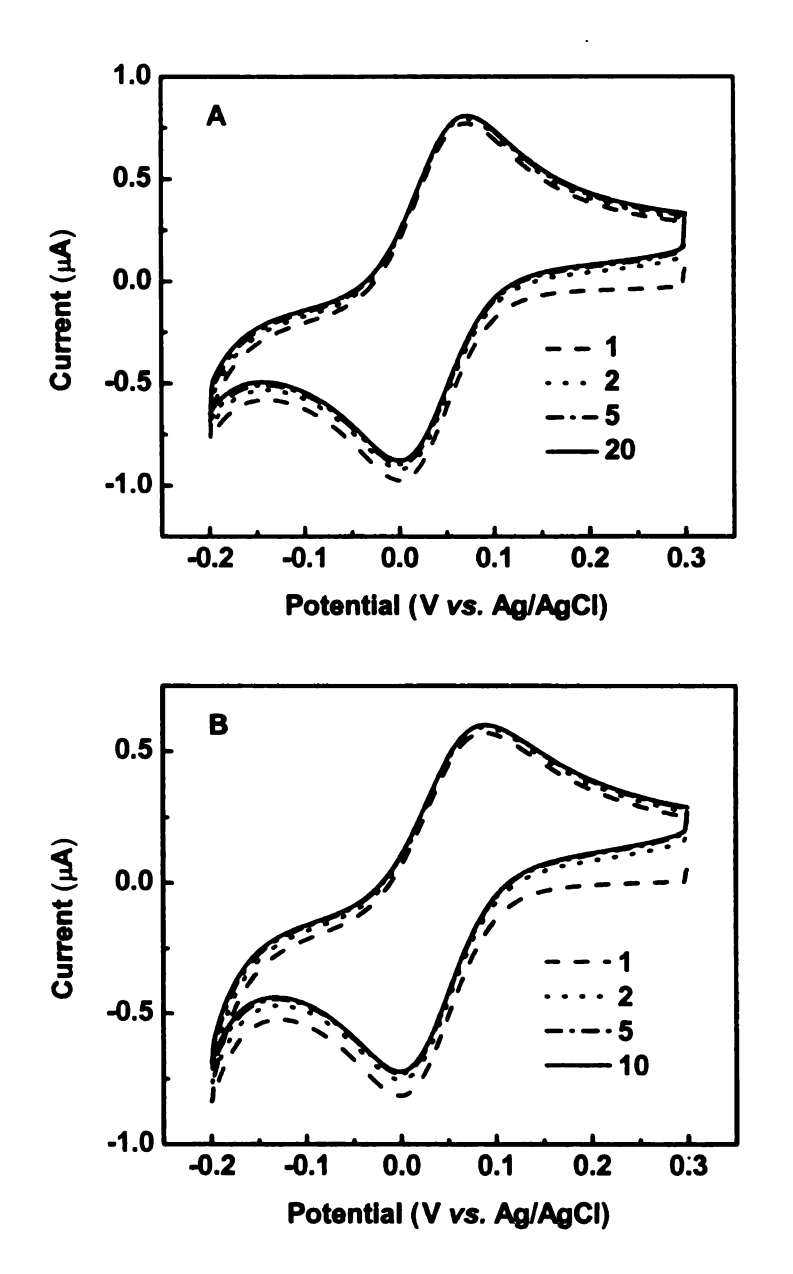
## 3.2.2 Cyclic Voltammetric Studies

In contrast to the previously reported quasi-reversible, diffusion-controlled voltammetric response at the as-deposited boron-doped diamond electrode, there was no defined cyclic voltammetric reduction or oxidation peak observed for cytochrome c (Figure 3.5) at hydrogen-terminated boron-doped diamond. The increase in the cathodic current at -0.2 V can be attributed to the reduction of dissolved oxygen catalyzed by a polymerized Fe-porphyrin protein, as will be discussed later.  $^{50, 51}$ 



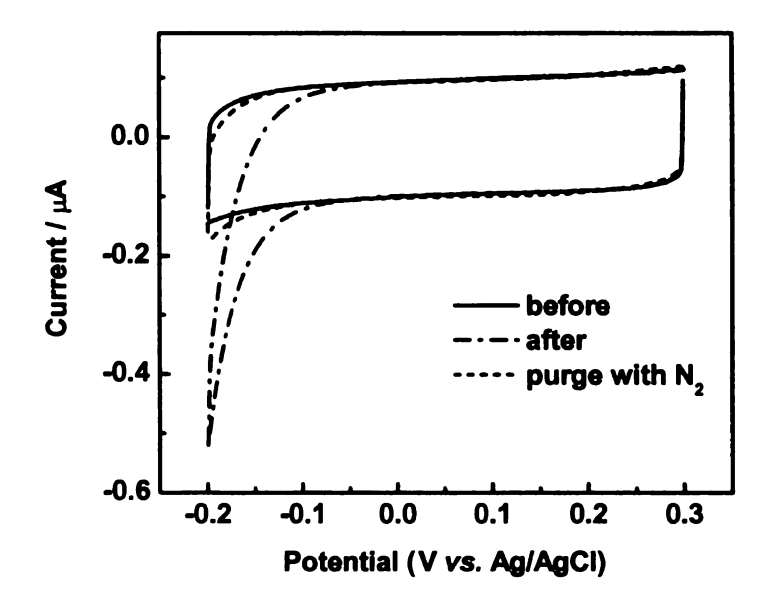
**Figure 3.5** Cyclic voltammetric *i-E* curve of 0.1 mM cytochrome *c* in 0.1 M NaCl, 10 mM Tris-HCl (pH 7) solution at a hydrogen-terminated UNCD electrode. Scan rate=20 mV/s.

However, a completely different response was observed for the oxygenterminated electrodes. Figure 3.6 shows cyclic voltammetric *i-E* curves for cytochrome c at oxygen-terminated UNCD and MCD electrodes as a function of the cycle number. Two well-resolved oxidation and reduction peaks are seen for both electrodes with no decrease in peak current or change in  $\Delta E_p$  during repeated cycling. This indicates that no significant protein denaturation occurs that could foul the electrode.



**Figure 3.6** Cyclic voltammetric *i-E* curves for 0.1 mM cytochrome *c* in 0.1 M NaCl, 10 mM Tris-HCl buffer (pH 7) at oxygen-terminated (A) UNCD and (B) MCD electrodes. Curves are shown for different scan numbers. Scan rate=20 mV/s.

Stable voltammetric traces are indicative of stable protein structure near the electrode surface. Cyclic voltammetric *i-E* background curves for oxygenterminated UNCD before and after electrode cycling in the presence of cytochrome *c* are shown in Figure 3.7. A small increase in the cathodic current at -0.2 V is seen for the electrode after potential cycling in the presence of the protein. Similar curves were also observed for oxygen-terminated MCD electrodes. We suppose that this "extra" cathodic current is due to the reduction of dissolved oxygen, catalyzed by a polymerized Fe-porphyrin protein residue on the electrode. <sup>50, 51</sup> Indeed the current diminished after a 10 min deoxygenation step involving N<sub>2</sub> purging.



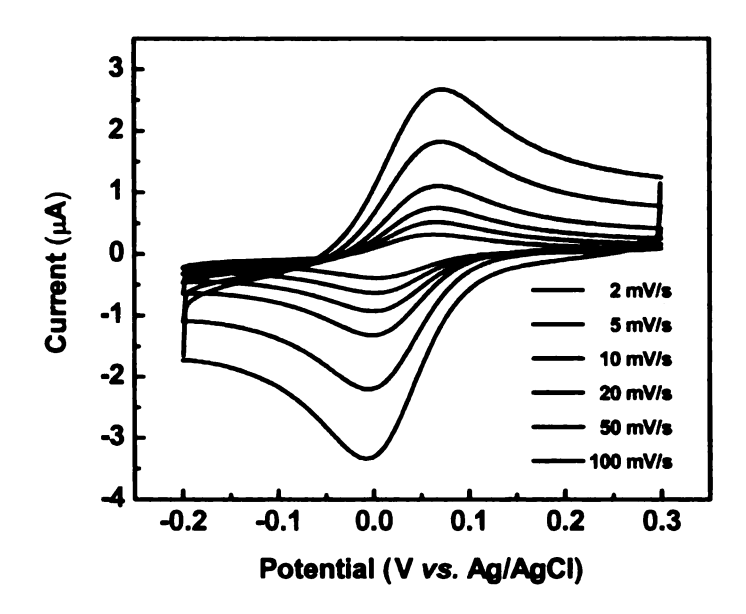
**Figure 3.7** Cyclic voltammetric background *i-E* curves for an oxygenterminated UNCD electrode. Cyclic voltammograms were measured in 0.1 M NaCl and 10 mM Tris-HCl (pH 7) before (solid line), after (dashed dot line) cytochrome c potential cycling and after purging with  $N_2$  (dashed line) following cytochrome c measurements. Scan rate=20 mV/s.

Figure 3.8 shows cyclic voltammetric *i-E* curves for cytochrome c at an oxygen-terminated UNCD electrode at different scan rates. The midpoint potential ( $E_{1/2}$ ), measured as the average between the reduction and oxidation peak potentials, is 0.032 V vs. Ag/AgCl (0.229 V vs. NHE).  $E_{1/2}$  is unchanged over the probed scan rate range. The cathodic peak currents,  $i_{pc}$ , were found to increase proportionally with the square-root of the potential scan rate,  $v^{1/2}$ , and with the protein concentration,  $C^*$ , as shown in Figure 3.9A and B. The linear relationship between  $i_p$  and  $v^{1/2}$  is typical of a diffusion-controlled electrochemical reaction according to the Randles-Sevcik equation,

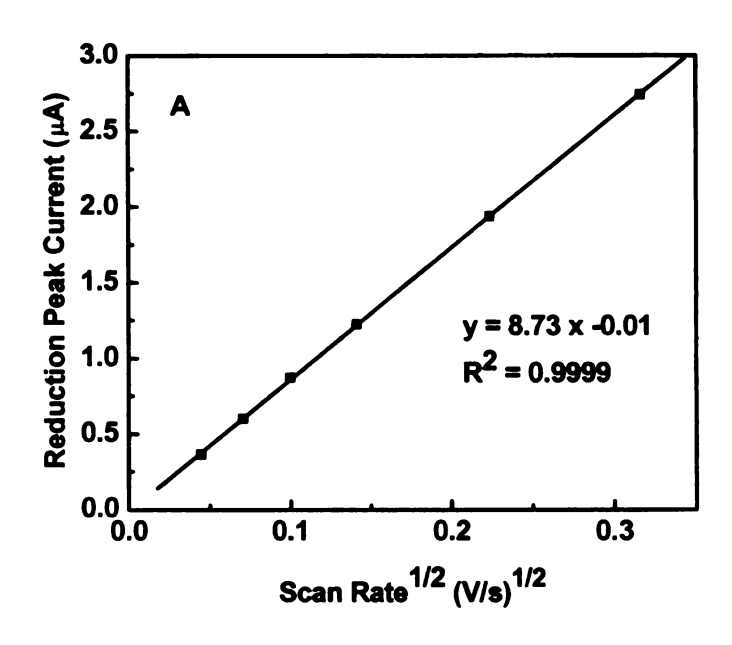
$$i_p = (2.69 \times 10^5) n^{3/2} AD^{1/2} C^* v^{1/2},$$

where n is the number of electrons, A is the electrode area (cm²), C\* is the bulk concentration of analyte (mol/cm³), D is the diffusion coefficient (cm²/s), and v is the scan rate (V/s). The diffusion coefficient, D<sub>ox</sub>, was determined from the slope of the i<sub>pc</sub>- $v^{1/2}$  curve and was calculated to be 2.63 ×10<sup>-6</sup> cm²/s for UNCD (2.09 ×10<sup>-6</sup> cm²/s for MCD). The apparent heterogeneous electron-transfer rate constant,  $k_{app}^{o}$ , was calculated from the scan rate dependence of  $\Delta$ E<sub>p</sub> using Nicholson's theoretical treatment, and assuming a charge-transfer coefficient  $\alpha$ =0.5.<sup>52</sup> The nominal values of  $k_{app}^{o}$  (3.48±1.25 ×10<sup>-3</sup> cm/s for UNCD and 2.38±0.72 ×10<sup>-3</sup> cm/s for MCD) are slightly higher than but close to the rate constant reported for other bare electrodes (1.0±0.1 ×10<sup>-3</sup> cm/s).<sup>53</sup> These rate constants were calculated using diffusion coefficient value 1.1×10<sup>-6</sup> cm²/s

determined by other methods.<sup>54, 55</sup> The fact that the calculated  $k_{app}^{o}$  value is statistically the same at all scan rates (Table 3.2), suggests that ohmic resistance within the electrode or the cell does not influence the voltammetric curve shape (i.e.,  $\Delta E_p$ ).



**Figure 3.8** Cyclic voltammetric *i-E* curves for 0.1 mM cytochrome *c* in 0.1 M phosphate buffer (pH 7.5) at UNCD electrodes at different scan rates. Electrode area=0.2 cm<sup>2</sup>.



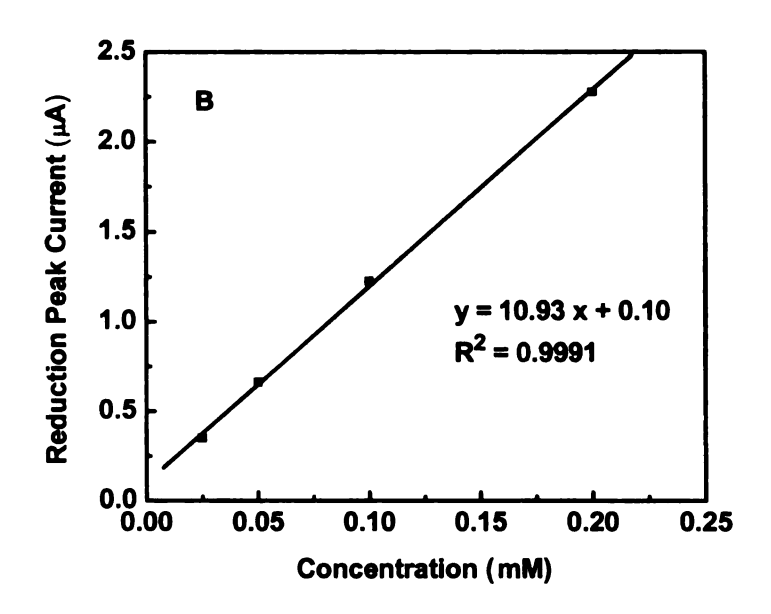


**Figure 3.9** Cyclic voltammetric data for cytochrome c at UNCD electrodes. Electrode area=0.2 cm<sup>2</sup>. (A) Plot of reduction peak current for 0.1 mM cytochrome c solution versus the square root of the scan rate; (B) Plot of reduction peak current versus cytochrome c concentration from 0.025 to 0.2 mM in 0.1 M phosphate buffer (pH 7.5) at 20 mV/s.

**Table 3.2** Apparent heterogeneous electron-transfer rate constant,  $k_{app}^{o}$ , calculated from cyclic voltammetric data.

Scan rate	k <sup>o</sup> <sub>app</sub> (×10 <sup>-3</sup> cm/s)*				
V/s	UNCD	MCD			
0.005	3.55 ± 1.18	1.98 ± 0.31			
0.01	$2.90 \pm 0.58$	$2.26 \pm 0.34$			
0.02	$3.28 \pm 0.72$	$2.55 \pm 0.35$			
0.05	$3.29 \pm 0.94$	$2.33 \pm 0.34$			
0.1	3.46 ± 1.23	$2.80 \pm 0.30$			
Avg.	3.48 ± 1.25	$2.38 \pm 0.72$			

<sup>\*</sup> Calculations were performed with T=298 K,  $D_o=D_R=1.1\times10^{-6}$  cm²/s and  $\alpha=0.5$ .

The effect of pH on the cytochrome c voltammetric response was investigated between pH 6 and 9. A slight shift in  $E_{1/2}$  toward more negative values by ca. 10 mV over the pH range was found, as shown in Table 3.3. The peak separation  $\Delta E_p$  showed a slightly decrease followed by an increase as the pH was increased from 6 to 9. This trend was more obvious for the MCD electrodes. This indicates that there is an optimum pH range for the electron transfer kinetics. Figure 3.10 shows the dependence of the reduction peak current on the solution pH. The maximum reduction peak current was obtained between pH 7 and 7.5, which was the same as the biological media pH. This might be caused by a decrease of the electrostatic interaction between the cytochrome c and the electrode surface at pH<7 and pH>7.5.

**Table 3.3** pH dependence of the midpoint potential  $E_{1/2}$  of cytochrome c at boron-doped diamond electrodes. Scan rate=20 mV/s. Electrode area=0.2 cm<sup>2</sup>.

рН	E <sub>1/2</sub> (mV) <i>vs.</i> Ag/AgCl	ΔE <sub>p</sub> (mV) UNCD	ΔE <sub>p</sub> (mV) MCD
6	40	82	98
7	33	72	79
7.5	32	73	77
8	32	71	77
9	30	77	82

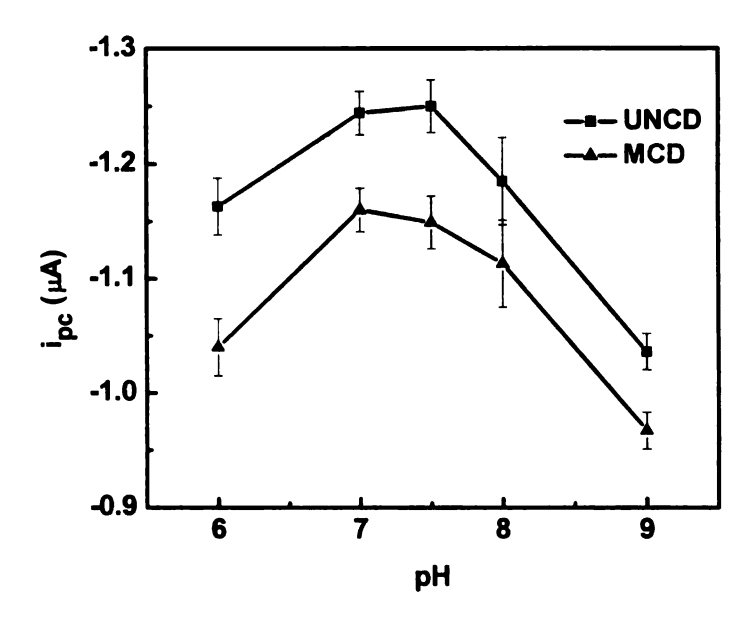


**Figure 3.10** Effect of the solution pH on the cytochrome c reduction peak current at boron-doped diamond electrodes. The solutions were 0.1 mM cytochrome c in 0.1 M phosphate buffer at different pH. Scan rate=20 mV/s. Electrode area=0.2 cm<sup>2</sup>.

#### 3.3 Discussion

The key finding from this work is that there is no observed voltammetric response for cytochrome *c* at the hydrogen-terminated boron-doped diamond electrode, but there is for the oxygen-terminated electrode. This is contrary to our previously reported results.<sup>32</sup> Haymond *et al.* reported quasi-reversible, diffusion-

controlled electron transfer for cytochrome c at as-deposited boron-doped diamond electrodes, which were presumed to be hydrogen-terminated.<sup>32</sup> The asdeposited surface was presumed to be low in oxygen, largely hydrogenterminated, however, no independent measurements was made (e.g., XPS) to confirm this. The different electrochemical response of the as-deposited and hydrogen-terminated diamond electrodes reported presently probably means that the as deposited films used in the original work contained some surface oxygen. The results presented herein clearly show that the oxygen-terminated diamond electrode is the most active surface for cytochrome c electron transfer. As the isoelectric point for cytochrome c is near pH 10, ion-dipole interactions between the positively charged cytochrome c at pH 7 and carbon-oxygen groups, which have dipoles with the negative ends pointing away from the electrode surface, or carbon-hydrogen groups, which have oppositely oriented dipoles, can be used to explain the different electrochemical responses observed at oxygen- and hydrogen-terminated diamond electrodes.

The diffusion coefficients determined from the slope of the  $i_{pc}$ - $v^{1/2}$  curves  $(2.63 \times 10^{-6} \text{ cm}^2/\text{s} \text{ for UNCD and } 2.09 \times 10^{-6} \text{ cm}^2/\text{s} \text{ for MCD})$  are about two times higher than the reported value of  $1.1 \times 10^{-6} \text{ cm}^2/\text{s}$  determined by other methods.<sup>54</sup>. Uncertainty in the magnitude of certain variables, such as the electrode area (A), the solution concentration (C), and the number of electrons transferred per mole (n), that were used to calculate the diffusion coefficient, could lead to errors in the calculated coefficient. Calculation of the diffusion coefficient from the

voltammetric data assumes that the peak current is exclusively controlled by diffusion of the analyte to and from the electrode. We suppose that the higher calculated diffusion coefficient in our work is caused by some limited protein adsorption on the electrode surface. In other words, the electrochemical reaction of the cytochrome c at oxygen-terminated boron-doped diamond electrodes appears to involve a combination of adsorption and diffusion. It should be pointed out though, that we only have an indirect response for protein adsorption; i.e., the enhanced oxygen reduction current. Rikhie et al. showed that carbonyl functionalities on graphite promote cytochrome c adsorption leading to a molecular orientation favorable for electron transfer.<sup>23</sup> We did not determine the specific carbon-oxygen functional groups on the oxidized diamond, but Fujishima and coworkers did. 41, 43-45 They reported that the carbon-oxygen functional groups on diamond can be of multiple types: carbonyl (C=O) and ether (C-O-C) on diamond (100) surface, 41, 43 and hydroxyl (C-OH) on diamond (111) surface. 44. <sup>45</sup> The carbonyl groups at the oxygen-terminated diamond surface might promote the pre-concentration of cytochrome c and facilitate the electron transfer. Compared to other carbon electrode materials, molecular adsorption on diamond is generally weak and this is what leads to the high level of fouling resistance. This is in contrast to the fouling caused by adsorbed cytochrome c at the exfoliated graphite electrode surface in less than 1 h.23 The diamond surface is auite heterogenerous structurally and chemically. There are different crystallographic orientations with different functional groups. There are grain boundaries and the sp<sup>2</sup>-bonded carbon that resides there. There are boron clusters aggregated in the grain boundaries and likely boron sites at the surface of the diamond. Therefore, there are multiple sites where adsorption can occur. It appears that electron transfer proceeds in a diffusion controlled manner at most sites on the electrode. There are sites that are presumably free of adsorbed proteins. There are other sites where some protein adsorption occurs. Some of this protein is electrochemically active leading to slightly larger voltammetric peak currents than those for the diffusion-controlled reaction. There also appears to be some of this adsorbed protein that is electrochemically inactive because of denaturation, but the exposed heme catalyzes the oxygen reduction reaction.

The midpoint potential, E<sub>1/2</sub>, measured at the oxygen-terminated diamond electrodes (0.229±0.007 V vs. NHE) is more negative than the 0.257±0.017 V vs. NHE value reported for cytochrome c in solution, but close to 0.221±0.007 V vs. NHE for immobilized cytochrome c.<sup>56, 57</sup> An open heme conformation proposed by Hildebrandt and coworkers might explain the negative shift of the formal potential.<sup>36, 56, 58</sup> They demonstrated the existence of two conformational states (B1 and B2) of immobilized cytochrome c on a silver electrode using surface enhanced resonance Raman spectroscopy.<sup>36, 58, 59</sup> In state B1, the native structure of the heme protein is fully preserved, while in conformational state B2, the heme iron exists as a mixture of five-coordinated high-spin and six-coordinated low-spin configurations in thermal equilibrium. The B2/B1 conformational equilibrium is potential dependent. The differences of the two states, in heme pocket structure and coordination configuration, result in different

electron-transfer properties.<sup>59</sup> The structural changes in state B2 are restricted to the heme crevice, which leads to a more open conformation compared to the closed structure in state B1. In our case, the pre-concentrated cytochrome *c* might exhibit a more open conformational than cytochrome *c* in the solution, and results in the negative shift of formal potential.

As mentioned, our evidence for adsorption is indirect and comes from the voltammetric data presented in Figure 3.7 for the residual oxygen reduction current. XPS data were recorded for the oxidized UNCD electrode after potential cycling in a cytochrome c solution. The spectrum showed a N 1s peak at 400 eV, presumably from the heme of adsorbed cytochrome c molecules on the surface. Similar observations were made for MCD. However, there was no detectable signal for Fe (2p<sub>3</sub>, 710 eV) or S (2p<sub>3</sub>, 165 eV) atoms from the heme moiety as one might expect. This can be explained in the following manner: (1) the high number of N atoms relative to Fe in the heme and (2) the Fe in the heme may be buried within the tertiary structure of the protein such that the probability of a photoelectron from the Fe escaping is low. D'Souza et al. also reported very weak XPS signals for Fe and S atoms of immobilized cytochrome c on fullerene film-modified electrodes. 18 The cyclic voltammetric background curve after electrode cycling in the presence of cytochrome c showed an increased cathodic current at -0.2 V, which was attributed to the reduction of dissolved oxygen catalyzed by the porphyrin of adsorbed cytochrome c.50 The absence of cytochrome c redox peaks in the background voltammograms could be because the protein is adsorbed, but in a configuration less favorable for electron transfer. The absence of redox peaks might also be due to the amount of adsorbed cytochrome c or heme unit is too low to be electrochemically detected but is enough to catalyze the oxygen reduction reaction.

#### 3.4 Conclusions

Room temperature cyclic voltammetric data as a function of the surface chemistry, film morphology and solution pH were presented at boron-doped diamond electrodes. Quasi-reversible, diffusion-controlled electrochemical responses were observed for oxygen-terminated and not for hydrogen-terminated diamond electrodes. No decrease in peak currents or change in  $\Delta E_p$  during repeated cycling indicates that no significant protein denaturation occurs at the electrode surface. The pH studies show that a maximum peak current and relatively low peak separation appears between pH 7 and 7.5. No electrochemical response was observed for hydrogen-terminated diamond electrodes. The different electrochemical responses of as-deposited and hydrogen-terminated diamond electrodes can be explained by different atomic ratios of O/C. In conclusion, the key finding was that the most reproducible and reversible response was observed for the oxygen-terminated, hydrophilic diamond electrode.

#### 3.5 References

- (1) Moore, G. R.; Williams, R. J. P. *Eur. J. Biochem.* **1980**, *103*, 523-532.
- (2) Moore, G. R.; Huang, Z.-X.; Eley, C. G. S.; Barker, H. A.; Williams, G.; Robinson, M. N.; Williams, o. J. P. *Faraday Discuss. Chem. Soc.* **1982**, *74*, 311-329.
- (3) Stellwagen, E. *Nature* **1978**, 275, 73-74.
- (4) Koppenol, W. H.; Margoliash, E. *J. Biol. Chem.* **1982**, 257, 4426-4437.
- (5) Matthew, J. B.; Weber, P. C.; Salemme, F. R.; Richards, F. M. *Nature* **1983**, *301*, 169-171.
- (6) Liu, H.-H.; Lu, J.-L.; Zhang, M.; Pang, D.-W.; Abruña, H. D. *J. Electroanal. Chem.* **2003**, *544*, 93-100.
- (7) Eddowes, M. J.; Hill, H. A. O. *J. Chem. Soc. Chem. Commun.* **1977**, 771 772.
- (8) Yeh, P.; Kuwana, T. Chem. Lett. 1977, 1145-1148.
- (9) Yue, H.; Waldeck, D. H.; Petrovic, J.; Clark, R. A. *J. Phys. Chem. B* **2006**, *110*, 5062-5072.
- (10) Ji, X.; Jin, B.; Jin, J.; Nakamura, T. *J. Electroanal. Chem.* **2006**, *590*, 173-180.
- (11) Zhong, T.; Qu, Y.; Huang, S.; Li, F. Microchimica Acta 2007, 158, 291-297.
- (12) Wu, Y.; Hu, S. Bioelectrochemistry 2006, 68, 105-112.
- (13) Zhou, J.; Lu, X.; Hu, J.; Li, J. Chem. Eur. J. 2007, 13, 2847-2853.
- (14) Wang, L.; Wang, E. Electrochem. Commun. 2004, 6, 49-54.
- (15) Ding, X.; Yang, M.; Hu, J.; Li, Q.; McDougall, A. *Microchimica Acta* **2007**, *158*, 65-71.
- (16) Yin, Y.; Wu, P.; Lü, Y.; Du, P.; Shi, Y.; Cai, C. *J. Solid State Electrochem.* **2007**, *11*, 390-397.
- (17) Zhao, G.-C.; Yin, Z.-Z.; Zhang, L.; Wei, X.-W. *Electrochem. Commun.* **2005**, 7, 256-260.

- (18) D'Souza, F.; Rogers, L. M.; O'Dell, E. S.; Kochman, A.; Kutner, W. *Bioelectrochemistry* **2005**, *66*, 35-40.
- (19) Liu, Y.-C.; Cui, S.-Q.; Yang, Z.-S. Anal. Sci. 2006, 22, 1071-1074.
- (20) Sallez, Y.; Bianco, P.; Lojou, E. J. Electroanal. Chem. 2000, 493, 37-49.
- (21) Huang, L. C.; Chang, H. C. Langmuir 2004, 20, 5879-5884.
- (22) Zhou, Y.; Zhi, J.; Zou, Y.; Zhang, W.; Lee, S.-T. *Anal. Chem.* **2008**, *80*, 4141-4146.
- (23) Rikhie, J.; Sampath, S. *Electroanalysis* **2005**, *17*, 762-768.
- (24) Szucs, A.; Novak, M. J. Electroanal. Chem. 1995, 383, 75-84.
- (25) Reed, D. E.; Hawkridge, F. M. Anal. Chem. 1987, 59, 2334-2339.
- (26) Hill, H. A. O.; Hunt, N. I.; Bond, A. M. J. Electroanal. Chem. 1997, 436, 17-25.
- (27) Kasmi, A. E.; Leopold, M. C.; Galligan, R.; Robertson, R. T.; Saavedra, S. S.; Kacemi, K. E.; Bowden, E. F. *Electrochem. Commun.* **2002**, *4*, 177-181.
- (28) Runge, A. F.; Saavedra, S. S. *Langmuir* **2003**, *19*, 9418-9424.
- (29) Hagen, W. R. Eur. J. Biochem. 1989, 182, 523-530.
- (30) Armstrong, F. A.; Hill, H. A. O.; Oliver, B. N. J. Chem. Soc., Chem. Commun. 1984, 976-977.
- (31) Marken, F.; Paddon, C. A.; Asogan, D. *Electrochem. Commun.* **2002**, *4*, 62-66.
- (32) Haymond, S.; Babcock, G. T.; Swain, G. M. *J. Am. Chem. Soc.* **2002**, *124*, 10634-10635.
- (33) Bowden, E. F.; Hawkridge, F. M.; Chlebowski, J. F.; Bancroft, E. E.; Thorpe, C.; Blount, H. N. *J. Am. Chem. Soc.* **1982**, *104*, 7641-7644.
- (34) Armstrong, F. A.; Cox, P. A.; Hill, H. A. O.; Lowe, V. J.; Oliver, B. N. J. *Electroanal. Chem.* **1987**, 217, 331-366.
- (35) Daido, T.; Akaike, T. J. Electroanal. Chem. 1993, 344, 91-106.
- (36) Rivas, L.; Murgida, D. H.; Hildebrandt, P. *J. Phys. Chem. B* **2002**, *106*, 4823-4830.
- (37) Geng, R.; Zhao, G.; Liu, M.; Li, M. *Biomaterials* **2008**, *29*, 2794-2801.

- (38) Liu, F. B.; Wang, J. D.; Liu, B.; Li, X. M.; Chen, D. R. *Diam. Relat. Mater.* **2007**, *16*, 454-460.
- (39) Yagi, I.; Notsu, H.; Kondo, T.; Tryk, D. A.; Fujishima, A. *J. Electroanal. Chem.* **1999**, *473*, 173-178.
- (40) Rao, T. N.; Yagi, I.; Miwa, T.; Tryk, D. A.; Fujishima, A. *Anal. Chem.* **1999**, 71, 2506-2511.
- (41) Notsu, H.; Yagi, I.; Tatsuma, T.; Tryk, D. A.; Fujishima, A. *J. Electroanal. Chem.* **2000**, *4*92, 31-37.
- (42) Tryk, D. A.; Tachibana, H.; Inoue, H.; Fujishima, A. *Diam. Relat. Mater.* **2007**, *16*, 881-887.
- (43) Pehrsson, P. E.; Mercer, T. W. Surf. Sci. 2000, 460, 49-66.
- (44) Loh, K. P.; Xie, X. N.; Yang, S. W.; Zheng, J. C. *J. Phys. Chem. B* **2002**, *106*, 5230-5240.
- (45) Notsu, H.; Fukazawa, T.; Tatsuma, T.; Tryk, D. A.; Fujishima, A. *Electrochem. Solid-State Lett.* **2001**, **4**, H1-H3.
- (46) Fujishima, A.; Einaga, Y.; Rao, T. N.; Tryk, D. A. *Diamond Electrochemistry*, 2005.
- (47) Rutter, M. J.; Robertson, J. Phys. Rev. B 1998, 57, 9241.
- (48) Rao, T. N.; Loo, B. H.; Sarada, B. V.; Terashima, C.; Fujishima, A. *Anal. Chem.* **2002**, *74*, 1578-1583.
- (49) Steinmuller-Nethl, D.; Kloss, F. R.; Najam-Ul-Haq, M.; Rainer, M.; Larsson, K.; Linsmeier, C.; Kohler, G.; Fehrer, C.; Lepperdinger, G.; Liu, X.; Memmel, N.; Bertel, E.; Huck, C. W.; Gassner, R.; Bonn, G. *Biomaterials* **2006**. *27*. 4547-4556.
- (50) Su, Y. O.; Kuwana, T.; Chen, S.-M. *J. Electroanal. Chem.* **1990**, 288, 177-195.
- (51) Okunola, A.; Kowalewska, B.; Bron, M.; Kulesza, P. J.; Schuhmann, W. *Electrochim. Acta* **2009**, *54*, 1954-1960.
- (52) Nicholson, R. S. Anal. Chem. 1965, 37, 1351-1355.
- (53) Bowden, E. F.; Hawkridge, F. M.; Blount, H. N. *J. Electroanal. Chem.* **1984**, *161*, 355-376.
- (54) Theorell, H. *Biochem. Z.* **1936**, *285*, 207-218.

- (55) Ehrenberg, A. Acta Chem. Scand. 1957, 11, 1257-1270.
- (56) Petrovic, J.; Clark, R. A.; Yue, H.; Waldeck, D. H.; Bowden, E. F. *Langmuir* **2005**, *21*, 6308-6316.
- (57) Hawkridge, F.; Kuwana, T. Anal. Chem. 1973, 45, 1021-1027.
- (58) Hildebrandt, P.; Stockburger, M. *Biochemistry* **1989**, 28, 6710-6721.
- (59) Wackerbarth, H.; Murgida, D. H.; Oellerich, S.; Döpner, S.; Rivas, L.; Hildebrandt, P. *J. Mol. Struct.* **2001**, *563-564*, 51-59.

# **CHAPTER 4**

# SPECTROELECTROCHEMICAL BEHAVIOR OF REDOX PROTEINS IN A THIN-LAYER TRANSMISSION CELL

## 4.1 Introduction

Spectroelectrochemistry is a hybrid combination of spectroscopy and electrochemistry, and has become an essential tool in the study of redox reaction mechanisms, particularly these for proteins and enzymes.<sup>1-7</sup> There are two essential components for transmission spectroelectrochemistry: an optically transparent electrode (OTE) and a thin-layer transmission electrochemical cell. There are two common types of OTEs: thin films of metal oxides and carbon. The development and application of carbon OTEs has recently been reviewed.<sup>8</sup> The main advantage of a thin-layer cell design is that exhaustive electrolysis of a redox analyte can occur within a short time (typically 20-120 s). Thin-layer cells should have a large electrode area (A) to solution volume (V) ratio, which can be achieved by confining a very small volume (e.g., a few μL) into a thin layer (< 100 μm) adjacent to an electrode surface.<sup>8, 9</sup> As long as the solution thickness, *I*, is less than the diffusion layer thickness, which depends on the analyte's diffusion

coefficient and time scale of measurement,  $I << \sqrt{2Dt}$ , finite diffusion will exist and the solution can be electrolyzed quickly and completely.

## 4.1.1 Ideal Thin-Layer Behavior

The theoretical thin-layer cyclic voltammetric *i-E* curve for a reversible, one-electron redox reaction is shown in Figure 4.1.

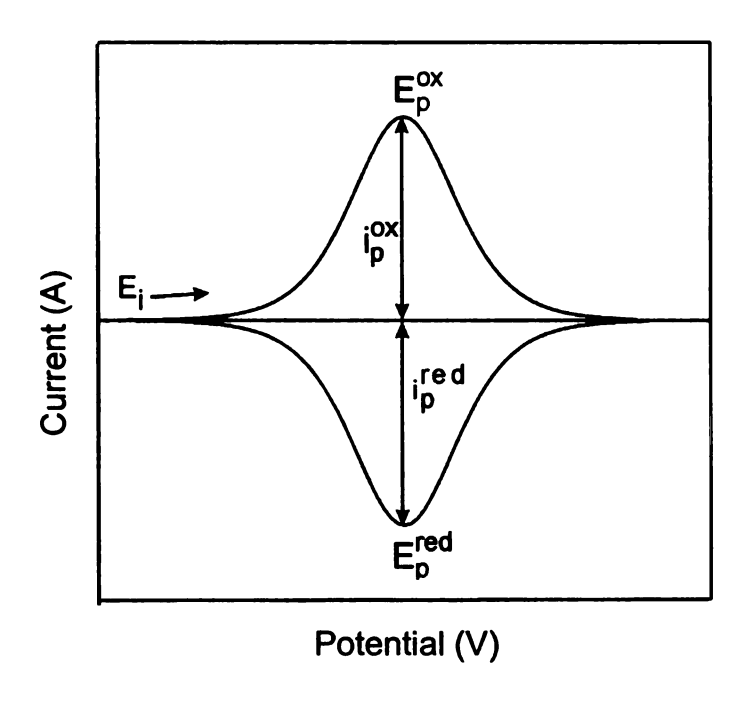


**Figure 4.1** A theoretical cyclic voltammetric *i-E* curve for a reversible, one-electron redox reaction in a thin-layer cell.

For ideal thin-layer behavior, the forward and reverse scans are in Gaussian shaped and mirror images of each other due to the exhaustive transformation between the reduced and oxidized forms. The cyclic voltammetric peak current,  $i_p$ , is equal to: $^{10}$ 

$$i_p = \frac{n^2 F^2 V C^* v}{4RT} = (9.39 \times 10^5) n^2 V C^* v$$

in which V is the cell volume (cm³), C\* is the bulk concentration of the redox molecule (mol/cm³), and v is the scan rate (V/s). n, F, R and T have their usual meanings. The peak current is predicted to vary linearly with the scan rate and the analyte concentration. The integrated area under the cyclic voltammetric peak is the faradaic charge, Q (Coulomb), which is independent of the scan rate according to the following expression:<sup>10</sup>

$$Q = nFN = nFVC^{\circ} = nFALC^{\circ}$$

in which A is the electrode area (cm²) and L is the thickness of the solution layer (cm). It can be seen that the charge is invariant with the scan rate, but depends on the number of moles of analyte electrolyzed and the number of electrons transferred per mole of analyte. From the charge associated with exhaustive electrolysis of a reactant, one can calculate the cell volume and compare it with the theoretical cell volume based on the cell dimensions (area × thickness). For a reversible system (*i.e.*, kinetically fast), the oxidation,  $i_p^{ox}$ , and reduction,  $i_p^{red}$ , peak currents, are predicted to be equal in magnitude. Also, the peak separation,  $\Delta E_p$ , is expected to be 0. However, if there is significant ohmic resistance between the working and counter electrodes or within the working electrode, or the electron-transfer kinetics are sluggish, the voltammogram will have a distorted shape and  $\Delta E_p > 0$ . Slow scan rates and low analyte concentrations can be used to minimize ohmic distortion of the cyclic voltammogram.

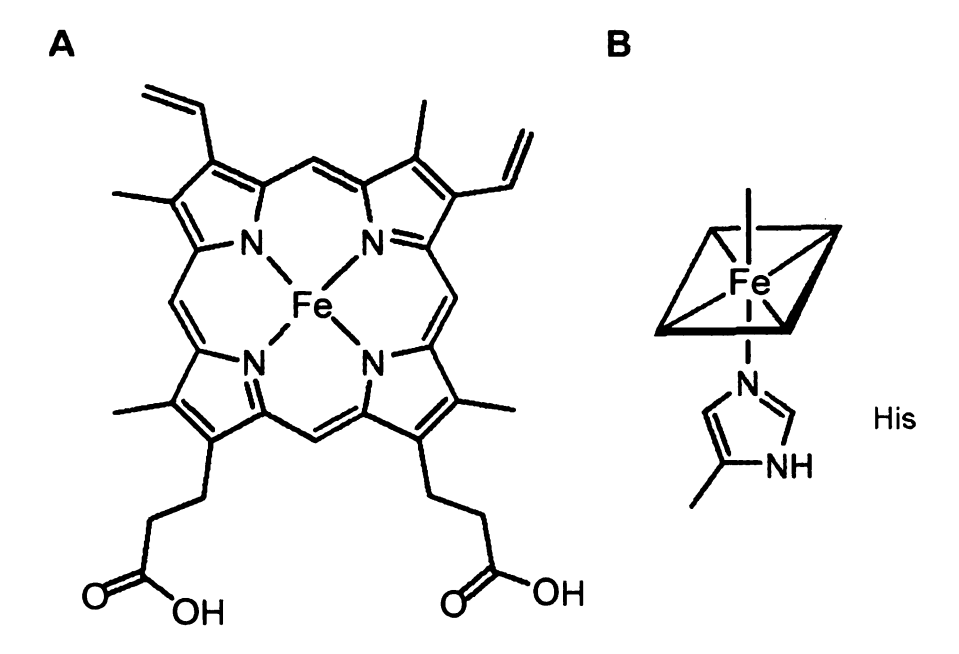
### 4.1.2 Ideal Thin-Layer Transmission Cell

An ideal thin-layer transmission cell should possess several features in order for good correlation between the electrochemical and spectroscopic signals:

a) rapid and complete electrolysis of the redox analyte, and b) agreement between the experimental and theoretical values. Moreover, the cell needs to c) accept different electrode materials, including thin-film electrodes, d) require a small operational sample volume, especially for anaerobic conditions, and e) provide reproducible, quantitative portability between optical and infrared domains (physically and spectrally) for direct spectral correlations.

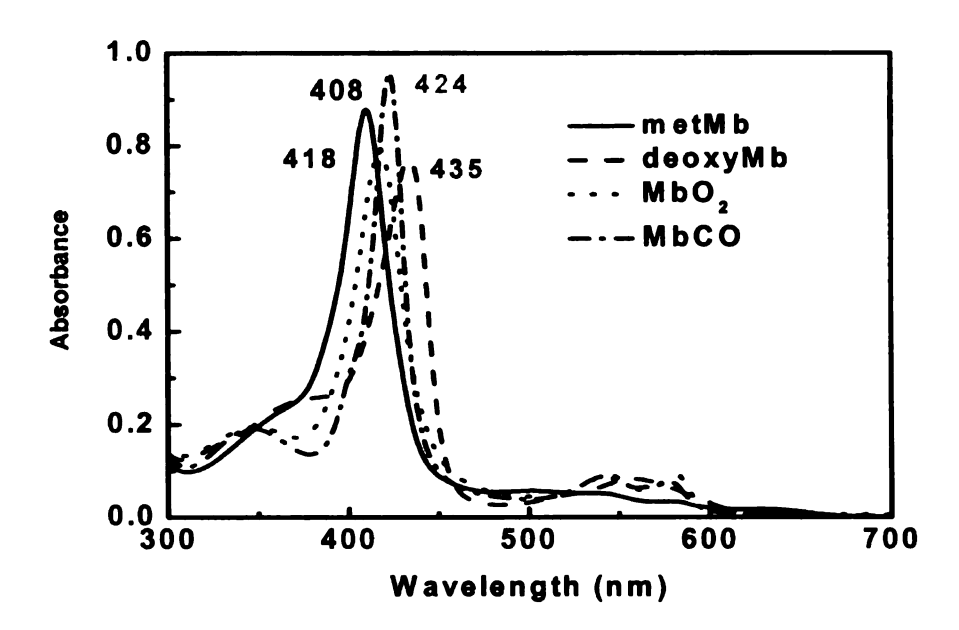
# 4.1.3 Electrochemical Studies of Myoglobin

Myoglobin (Mb) plays a critical role in oxygen transport and storage in muscle cells. It is a small (MW ~18,800 g/mol), heme-containing protein. It functions to maintain full muscular working capacity and a high level of oxidative phosphorylation under long-term oxygen deficiency. It is a globular protein with a single polypeptide chain that is made up of 153 amino acids. It contains a single heme b prosthetic group, as shown in Figure 4.2. Histidine is one of the iron's axial ligands, while the opposite axial coordination site is vacant or weakly ligated by the solvent. The heme group is largely buried inside the nonpolar pocket of the polypeptide chain. 13-15



**Figure 4.2** Heme *b* structure of myoglobin. (A) Planar porphyrin ring system and (B) heme Fe is axially bound to a histidine molecule with the sixth coordination site remaining unoccupied or weakly ligated by a solvent molecule.

Due to the vacant sixth coordination position, the heme iron can bind oxygen. It can also easily bind other ligands, such as CO and NO. The UV-Vis absorption spectra of horse myoglobin, with different bound ligands and different iron oxidation states, are displayed in Figure 4.3. The corresponding extinction coefficients for the absorption peaks are listed in Table 4.1.<sup>16</sup> The concentration of myoglobin in solution can be determined spectroscopically from the absorption spectrum for MbCO.



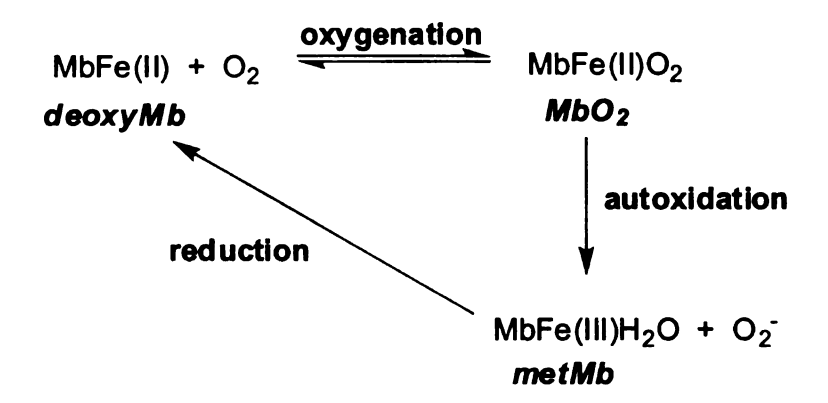
**Figure 4.3** UV-Vis spectra for horse myoglobin in different oxidation states with different bound ligands. Metmyoglobin (metMb): MbFe(II)H<sub>2</sub>O, deoxymyoglobin (deoxyMb): MbFe(II), oxymyoglobin (MbO<sub>2</sub>): MbFe(II)O<sub>2</sub> and carboxymyoglobin (MbCO): MbFe(II)CO.

Table 4.1 Extinction coefficients for horse myoglobin at pH 7, ~20 °C. 16

	metMb		MbO <sub>2</sub>		MbCO		deoxyMb	
Soret / nm	408				424		435	
ε / mM <sup>-1</sup> cm <sup>-1</sup>	188				207		121	
visible / nm	502	630	542	580	540	579	560	
ε / mM <sup>-1</sup> cm <sup>-1</sup>	10.2	3.9	13.9	14.4	15.4	13.9	13.8	

Due to the vacant coordination position, the ferrous heme iron can bind oxygen reversibly and carry out its physiological function.<sup>17</sup> As shown in the following scheme, after the oxygen binding, the oxygen-containing form of MbO<sub>2</sub> is easily oxidized to ferric metMb with generation of superoxide anion. The metMb can not be oxygenated and is physiologically inactive. The metMb

reductase in muscle tissues can reduce the metMb to the ferrous deoxyMb and maintains the continuity of myoglobin function *in vivo*.<sup>17</sup>



Electrochemical studies of Mb without ligands other than water is believed to involve a one-electron redox reaction between deoxyMb and metMb:<sup>18</sup>

MbFe(II) + 
$$H_2O \longrightarrow MbFe(III)H_2O + e^-$$
 E°'= 46 mV vs. NHE<sup>18</sup> deoxyMb metMb

The sixth coordination site is vacant in deoxyMb, while in metMb, the sixth coordination position is ligated by water. Compared with the physiological reaction, the differences are the oxidation state of the heme iron as well as the transition of the coordination state. This reaction involves heterogeneous electron transfer at the electrode followed by a ligand dissociation reaction in solution.<sup>18</sup>

Solution: MbFe(II)H<sub>2</sub>O 
$$\Longrightarrow$$
 MbFe(II) + H<sub>2</sub>O

It is well known that Fe(II) complexes are quickly and irreversibly oxidized in the presence of oxygen at ambient temperature. To inhibit the autoxidation reaction, the experiment should be carried out in an anaerobic environment. Both MbFe(III)H<sub>2</sub>O and MbFe(II) are known to have high-spin states and the iron is

below the heme plane positioned toward the proximal histidine due to the longer Fe-N bond. The intermediate MbFe(II)H<sub>2</sub>O is proposed to be low-spin with shorter Fe-N bonds in the porphyrin plane. The relatively slow heterogeneous electron-transfer kinetics are considered to be due to a large activation energy barrier for conversion of high-spin iron to low-spin states. 19

There is considerable interest in achieving direct electron transfer between an electrode and myoglobin. <sup>20-26</sup> Rusling and coworkers developed a method to perform direct protein electrochemistry by using insoluble surfactants to incorporate the protein onto an electrode. <sup>24, 27, 28</sup> They showed that protein-surfactant films on carbon, Au and Pt electrodes are stable for weeks in buffer. The surfactant provides a hydrophobic environment, much like that of the cell membrane, where the protein natively exists. Taniguchi *et al.* showed quasi-reversible voltammetry of horse heart myoglobin with an ultra-clean and hydrophilic indium oxide electrode. <sup>25, 26</sup>

In this chapter, the electrochemical and spectroscopic performance of a new thin-layer cell is described. Three model systems were used for demonstration:  $Fe(CN)_6^{-3/-4}$  as a fast and robust inorganic model; cytochrome c as a simple, stable and well characterized redox protein; and mygolobin as an oxygen-sensitive redox protein capable of chemical binding at the active site. It is well established in the literature that cyanide strongly competes with  $Met_{80}$  for binding to axial heme position in ferric cytochrome c. Taking advantage of the

excellent electrochemical properties of boron-doped diamonds (BDD), we present, for the first time, spectral characterization of redox-dependent cyanide binding to cytochorme c. The effect of UV irradiation on functional integrity of metMb was also investigated.

#### 4.2 Results

### 4.2.1 Electrochemical Performance of the Cell

Background-corrected cyclic voltammetric i-E curves for Fe(CN)<sub>6</sub><sup>-4</sup> in 1 M KCl at a glassy carbon electrode are shown in Figure 4.4 A-C. Symmetric oxidation and reduction peaks are seen with no evidence of any diffusional tailing. The  $i_p^{ox}$  /  $i_p^{red}$  and  $Q_p^{ox}$  /  $Q_p^{red}$  ratios are both close to unity, as expected for reversible electrolysis in the thin-layer cell. This shows that all of the reactant  $(Fe(CN)_6^{-3})$  is converted to the product  $(Fe(CN)_6^{-3})$  on the forward sweep and then is returned completely to the reactant on the reverse sweep. The  $E_{1/2}$  value for Fe(CN)<sub>e</sub> -3/-4 was stable across all the experimental conditions tested (E<sub>1/2</sub>=286±3 mV). Figure 4.4D shows a plot of the peak potential separation values  $(\Delta E_p)$ , recorded for  $Fe(CN)_6^{-4}$  using cyclic voltammetry, as a function of the solution layer thickness.  $\Delta E_p$  remains stable with increasing analyte concentration at all spacer thicknesses. However,  $\Delta E_p$  values for a 7.5  $\mu m$  spacer are higher than those for thicker 25 and 75 µm spacers.

Figure 4.4 Background-corrected cyclic voltammetric *i-E* curves for  $Fe(CN)_6^4$  in 1 M KCl in the thin-layer cell with a glassy carbon electrode. (A) Effect of scan rate for 1 mM  $Fe(CN)_6^4$  using the 75  $\mu$ m spacer; (B) effect of  $Fe(CN)_6^4$  concentration using the 75  $\mu$ m spacer at 1 mV/s; (C) effect of layer thickness for 1 mM  $Fe(CN)_6^4$  at 1 mV/s; and (D) peak separation as a function of layer thickness.

Figure 4.4

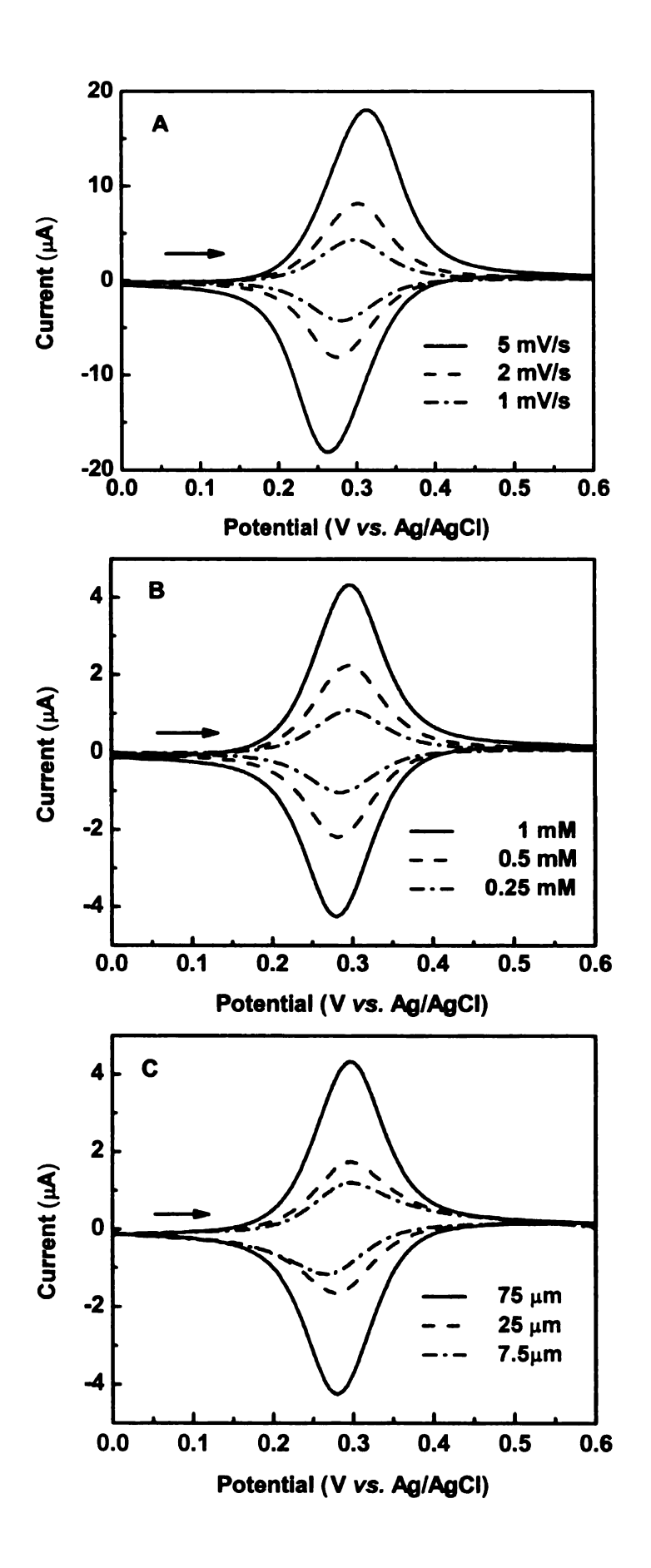
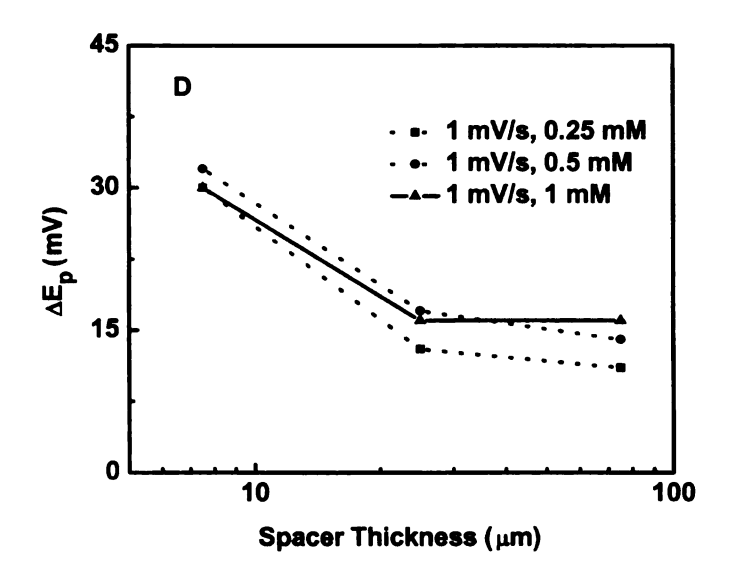
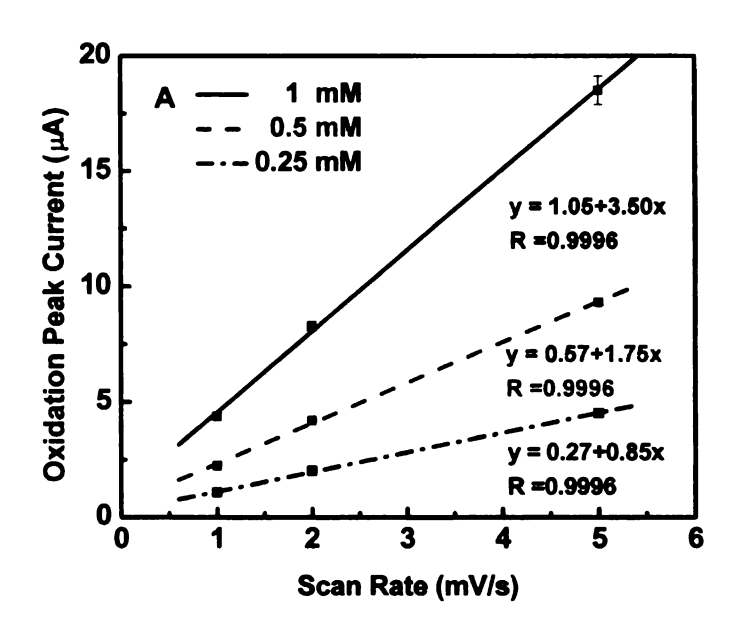


Figure 4.4 continued



The oxidation peak current increased linearly with the scan rate for all concentrations of  $\text{Fe}(\text{CN})_6^{-4}$  in 1 M KCI (Figure 4.5A). The thickness of the thin layer calculated from the slope is 58  $\mu\text{m}$ , which is slightly smaller than the specified spacer thickness of 75  $\mu\text{m}$ . The specified value was indicated by the manufacture of the material and not independently measured in this work. Similarly, layer thicknesses were calculated to be 19 and 10  $\mu\text{m}$ , respectively, for the 25 and 7.5  $\mu\text{m}$  spacers (figure not shown). The layer thicknesses obtained from optical measurements of metMb using  $\epsilon_{408}$ =188 mM<sup>-1</sup>cm<sup>-1</sup>) according to Beer's Law were 60, 18 and 6  $\mu\text{m}$  for the 75, 25 and 7.5  $\mu\text{m}$  spacers, respectively. These values are in good agreement with values determined from the electrochemical measurements. Figure 4.5B shows a trend of decreasing faradaic charge with increasing scan rate for all concentrations tested. The

decrease was most evident for the 1 mM concentration. Ideal thin-layer behavior would be evidenced by a constant change with increasing scan rate.



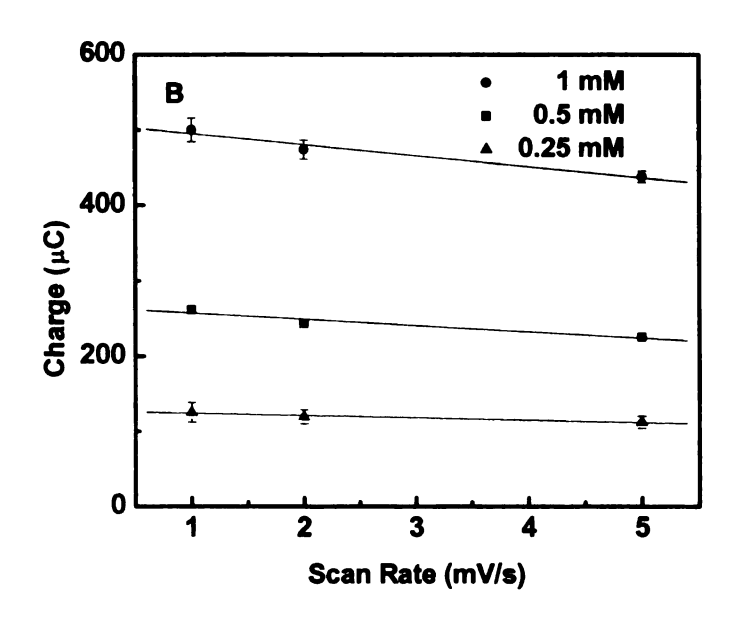


**Figure 4.5** Plots of (A) oxidation peak current and (B) faradaic charge vs. scan rate for different concentrations of  $Fe(CN)_6^{-4}$ . The spacer thickness was 75  $\mu m$  and the supporting electrolyte was 1 M KCI.

# 4.2.2 Spectroelectrochemcial Kinetics

Figure 4.6 shows the amperometric and simultaneously-recorded optical absorption measurements at 220 nm for  $Fe(CN)_6^{-4}$  at a gold minigrid electrode using the 25  $\mu$ m spacer. The current and absorbance were recorded during a potential step from -0.1 to 0.6 V. At lower electrolyte concentration (100 mM KCI), 1 and 5 mM  $Fe(CN)_6^{-4}$  was electrolyzed completely in 2 and 10 sec, respectively. The process was much faster at a higher concentration of supporting electrolyte (1 M KCI) with bulk electrolysis occurring within instrument sampling time.

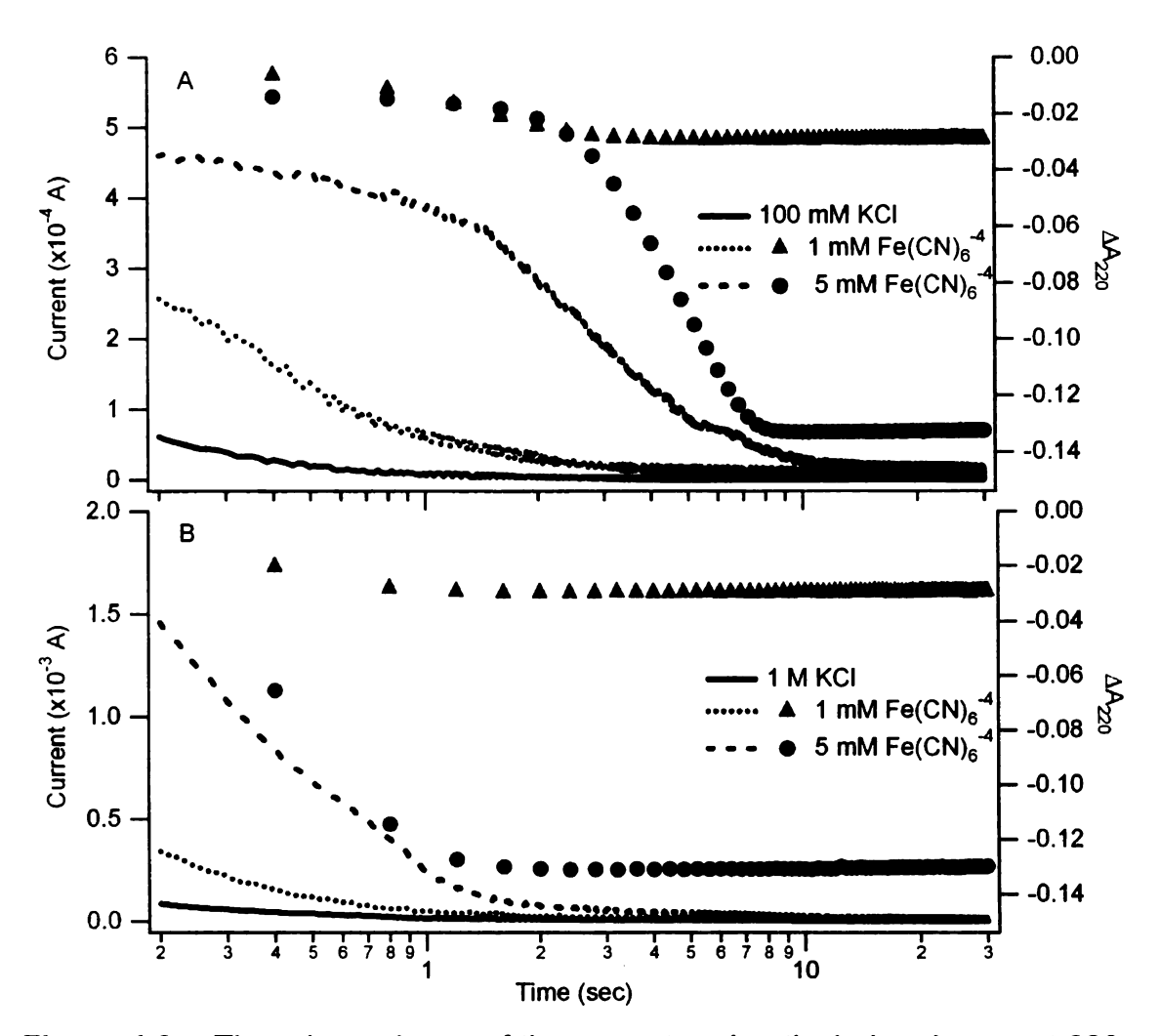
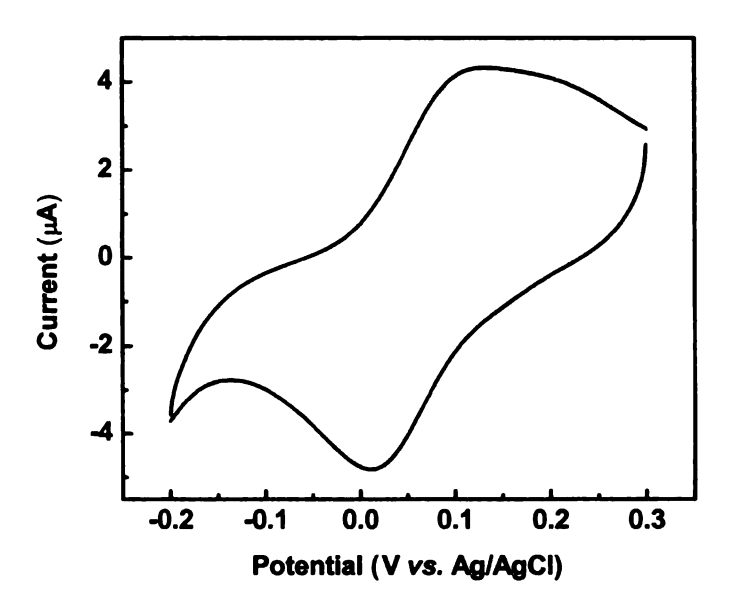


Figure 4.6 Time dependence of the current and optical absorbance at 220 nm for  $Fe(CN)_6^{-4}$  at a gold minigrid electrode in the thin-layer cell during a potential step from -0.1 to 0.6 V. Data are shown for supporting electrolyte concentration of (A) 100 mM KCl and (B) 1 M KCl. Lines are for the current on the left and markers are for the simultaneous optical changes on the right. The spacer thickness was 25  $\mu$ m.

Figure 4.7 shows cyclic voltammetric *i-E* curve for cytochorme c at a gold minigrid electrode in a thin-layer cell with a 75  $\mu$ m spacer. Well-defined oxidation and reduction peaks are present at 0.132 and 0.011 V. The determined midpoint potential at 0.071 V is in good agreement with the accepted value of 0.06 V.<sup>30</sup>

The cathodic current at -0.2 V is believed to be due to some residual oxygen reduction, as the thin-layer cell was not deoxygenated.



**Figure 4.7** Cyclic voltammetric *i-E* curve for cytochrome c at a gold minigrid electrode in a thin-layer cell with a 75  $\mu$ m spacer. The analyte solution was 0.1 mM cytochorme c in 10 mM phosphate buffer (pH 7) and 100 mM KCl. Scan rate=10 mV/s.

Figure 4.8 shows the difference absorbance spectra for cytochrome c during a potential step from 0.5 to -0.3 V at a gold minigrid electrode. As the potential was stepped to -0.3 V, the reduction of the cytochrome c occurred. A serious of positive-going (reduced form of the protein) and negative-going (oxidized form of the protein) peaks are observed. The spectra are the same as those reported previously.<sup>6,31</sup> Not only Soret (400-450 nm) and Q (500-600 nm) bands, but also N and L (200-400 nm) bands, are seen in the spectra. They are all attributed to porphyrin  $\pi \rightarrow \pi^*$  transitions in the protein.

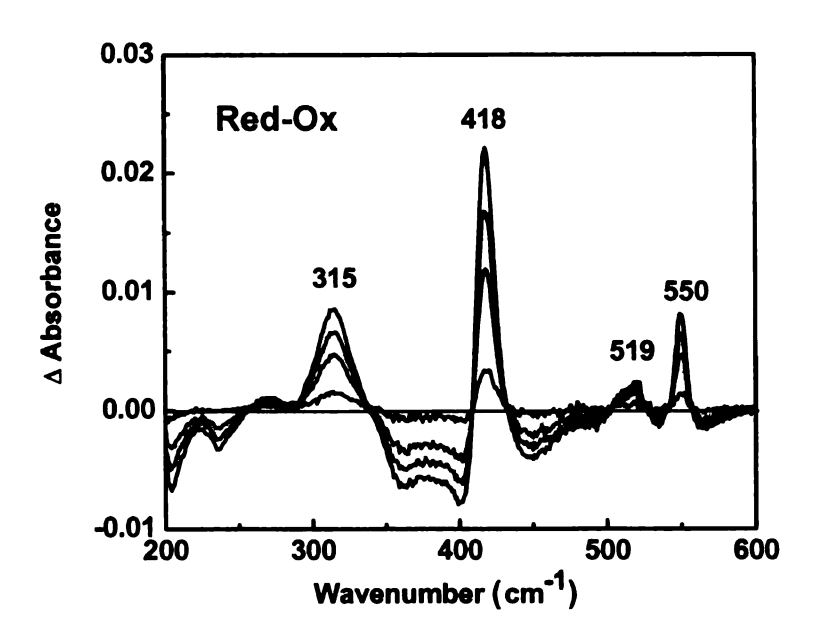


**Figure 4.8** Difference absorbance spectra of cytochrome c at a gold minigrid electrode in a thin-layer cell with a 75  $\mu$ m spacer. The Red-Ox difference spectra were generated during a potential step from 0.5 to -0.3 V. The analyte solution was 0.1 mM cytochorme c in 10 mM phosphate buffer (pH 7) and 100 mM KCl. The spacer thickness was 75  $\mu$ m.

Figure 4.9 shows the absorption-time curves for 0.1 mM cytochrome c in 10 mM sodium phosphate buffer (pH 7)+100 mM KCl during potential steps from 0.5 to -0.3 V at (A) a gold minigrid electrode and (B) a boron-doped diamond/quartz electrode using a 75  $\mu$ m spacer. The repetitive potential steps produced relatively slow, but generally reversible optical changes. The potentials were selected according to the voltammetric i-E curve for cytochrome c in aqueous solution. Clearly, cytochrome c exhibited slower electrochemical kinetics compared to  $Fe(CN)_6^4$ , as evidenced by the longer time required to reach a steady-state response after application of the potential step. While relatively fast at the beginning, both the rates and amplitudes of the absorbance

changes diminished noticeably in successive redox cycles over several minutes at a gold electrode. The reduction and oxidation of cytochrome c at a boron-doped diamond was noticeably slower than at the gold minigrid, but significantly more stable as no obvious change in amplitude or rate was observed over several redox cycles.

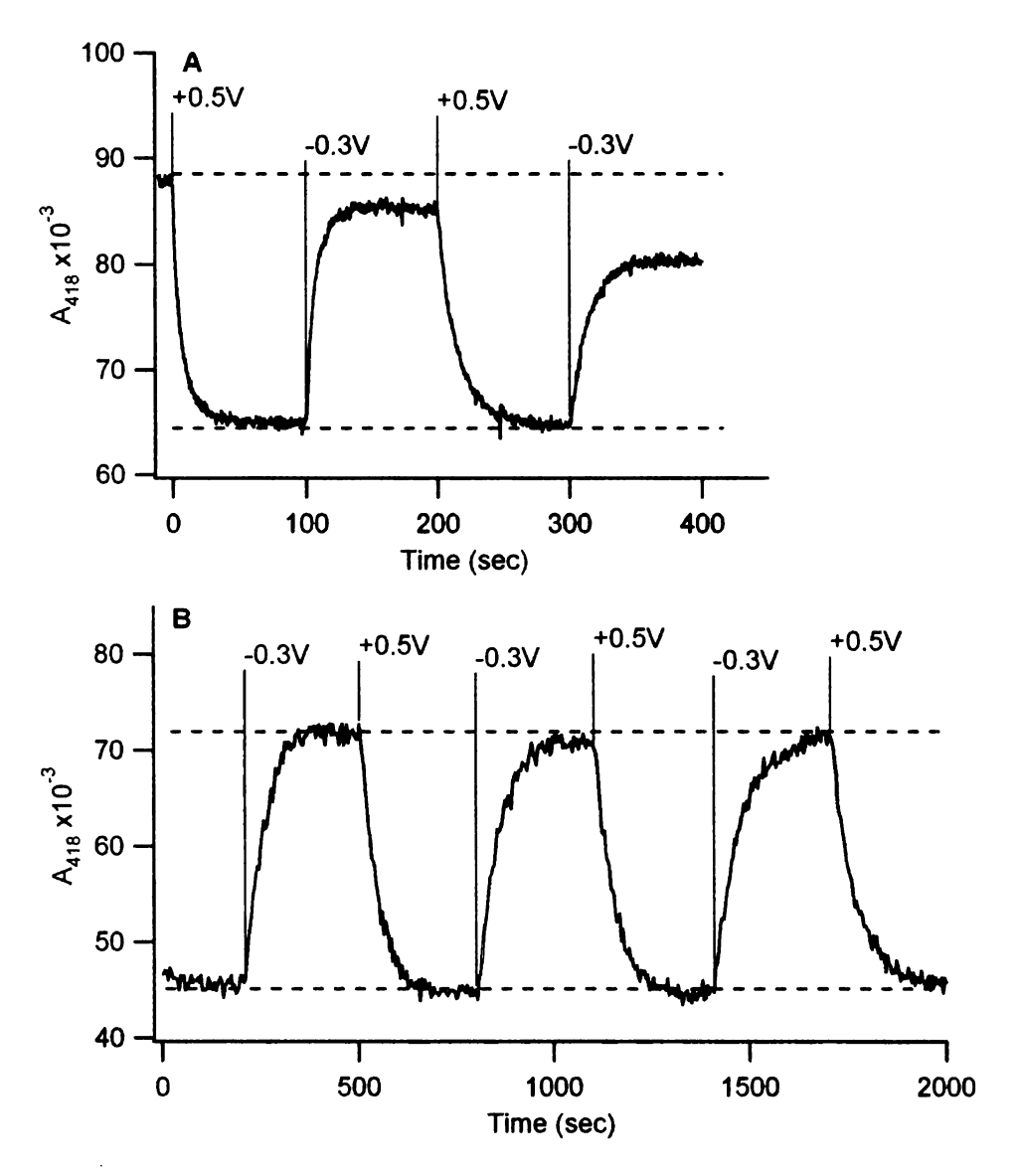


**Figure 4.9** Absorbance change of cytochrome c on (A) a gold minigrid electrode and (B) a boron-doped diamond thin film at 418 nm. The analyte solution was 0.1 mM cytochorme c in 10 mM phosphate buffer (pH 7) and 100 mM KCl. The spacer thickness was 75  $\mu$ m. Repetitive potential steps between 0.5 and -0.3 V were applied, as indicated in the figure.

# 4.2.3 Spectroelectrochemistry of Cytochrome *c* – Cyanide Complex

Scheiter et al. reported cyclic voltammetric studies of cytochrome c in the presence of KCN at a modified gold electrode.<sup>29</sup> They determined the redox potential of ferric/ferrous cytochrome c-cyanide redox couple for the first time and provided a detailed thermodynamic characterization of the complete cycle (Figure 4.10E).<sup>29</sup> Here, we use spectroelectrochemical method to demonstrate thermodynamic cycle of cytochrome c-cyanide complex. The spectral changes of cytochrome c in response to potential steps in the presence of CN are shown in Figure 4.10. The potential was stepped between +0.3, -0.3, and -0.7 V, as indicated in Figure 4.10A. These potentials were selected based on the reported potentials for oxidation and reduction of cytochrome c and cytochrome c-cyanide at 0.06 and -0.44 V vs. Ag/AgCl, respectively.<sup>29</sup> Data are shown as differences between wavelength pairs to minimize the contribution of baseline variations over time. The 421/404 nm pair corresponds to maximal peak/trough difference and reflects a combination of processes occurring in the sample. The 438/415 nm and 432/409 nm pairs are based on apparent isobestic points of two major observed processes. The difference absorbance spectra between key states (designated by letters a-g in Figure 4.10A) are shown in Figure 4.10 B-D. Upon the initial step from +0.3 to -0.3 V (a→b), a relatively rapid absorbance change was observed mostly at 438 nm. The corresponding difference spectrum is reflective of typical ferric/ferrous cytochrome c transition (Figure 4.10B, b-a). A subsequent step to -0.7 V (b→c) produced fast and intense changes at 432/409 nm, but caused no immediate response at 438/415 nm. Difference spectrum c-b was similar to that of the b-a transition except for a distinctive red shift in both Soret (400-450 nm) and  $\alpha$  (500-600 nm) spectral regions. Initial response was followed by slow, but distinctive reversal of optical changes at 421/404 and 432/409 nm (c $\rightarrow$ d). This slow phase was also clearly visible at 438/415 nm. The corresponding difference spectrum d-c (Figure 4.10D) indicated all an optical shift from 423 to 411 nm. A second shift was also clearly observed from 557 to 550 nm. In general, the 421/404 nm pair responded to both -0.3 and -0.7 V potential steps, while the 438/415 nm and 432/409 nm pairs only responded to one of them.

**Figure 4.10** Spectroelectrochemical measurements of cytochrome c-cyanide complex on a boron-doped diamond electrode. (A) Absorption changes at characteristic wavelengths; (B-D) difference absorbance spectra between key states as designated by letters a to g; and (E) thermodynamic cycle of cytochrome c-cyanide complex. The analyte solution was 0.1 mM cytochorme c in 0.1 M KCN, Tris buffer (pH 7) and 100 mM KCl. Potentials were stepped between +0.3, -0.3 and -0.7 V as indicated in the figure.

Figure 4.10

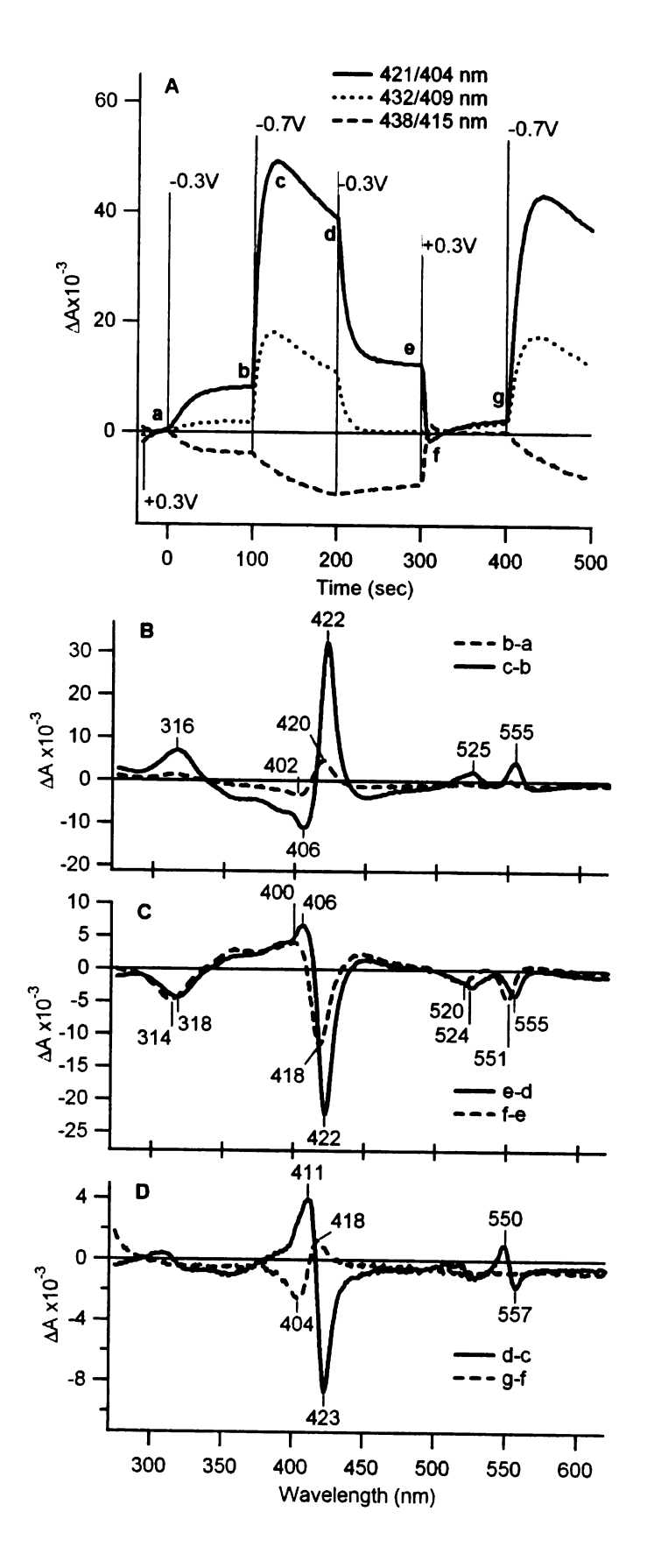


Figure 4.10 continued

E

Cyt c Fe(III) + e<sup>ot</sup> 
$$E_{Cytc}^{ot} = 60 \text{ mV}$$
 Cyt c Fe(II)

CN<sup>-</sup>  $K_D^{ox}$   $K_D^{red}$   $CN^-$ 

Cyt c Fe(III) ← CN<sup>-</sup> + e<sup>-</sup>  $E_{Cytc-CN}^{ot} = -440 \text{ mV}$  Cyt c Fe(II) ← CN<sup>-</sup>

Reversing the potential from -0.7 to -0.3V (d $\rightarrow$ e) mostly reversed the sample to state b, with one noticeable exception that the 438/415 nm pair did not respond to the potential step immediately, but showed a much slower change. Difference spectrum of the d $\rightarrow$ e transition (Figure 4.10C, e-d) was similar to that of b $\rightarrow$ c transition (Figure 4.10A, c-b) but at ~2/3 amplitude. The spectral changes for the next step (e $\rightarrow$ f) were similar, but much faster and twice the amplitude compared to initial a $\rightarrow$ b transitions. This was followed by slow spectral changes similar to the b $\rightarrow$ c step. Corresponding difference spectrum g-f showed peak/troughs at 418/404 nm. No clear changes were observed in the  $\alpha$  region at this step.

# 4.2.4 Spectroelectrochemistry of Myoglobin

Electrochemical studies of Mb without ligands other than water is believed to involve a one-electron redox reaction between deoxyMb and metMb (E°'= 0.046 V vs. NHE, -0.151 V vs. Ag/AgCl). Figure 4.11 shows absorbance-time profiles and absorption spectra for 50 μM myoglobin in 10 mM phosphate buffer solution (pH 7) and 100 mM KCl at a gold minigrid electrode. The spacer

thickness was 75 µm. The potential was stepped between +0.4 and -0.7 V for several cycles, as indicated in the figure. These potentials were selected based on the reported redox potential of myoglobin at -0.15 V vs. Ag/AgCl. The absorbance change depended on whether the protein solution was exposed to far-UV light or not. When all wavelengths were used for excitation (Figure 4.11 C and D), the peak for deoxyMb at 434 nm shifted to 412 nm as the potential was stepped to +0.4 V. However, for subsequent potential steps, the peak shifted to and stayed at 421 nm irrespective of the number of positive or negative potential steps. On the other hand, the redox reaction of Mb became fully reversible when mid-/far-UV sampling light ( $\lambda$ <300 nm) was blocked using a glass filter (Figure 4.11 A and B). A positive potential step led to a shift of the Soret absorption maximum initially at 434 (reduced form) to 409 nm (oxidized form), characteristic of a transition from deoxyMb to metMb and in agreement with the literature.<sup>7</sup> Such changes were reversed upon a potential step from +0.7 to -0.4 V. Spectra of deoxyMb and metMb obtained at the third redox cycle were completely superimposable with the corresponding initial spectra (Figure 4.11B).

**Figure 4.11** Absorbance-time profiles and absorption spectra of myoglobin without (A, B) and with (C, D) far-UV light exposure. Spectra were recorded in the thin-layer transmission cell with a gold minigrid electrode. The spacer thickness was 75  $\mu$ m. The analyte solution was 50  $\mu$ M myoglobin in 10 mM sodium phosphate buffer (pH 7) and 100 mM KCI.

Figure 4.11

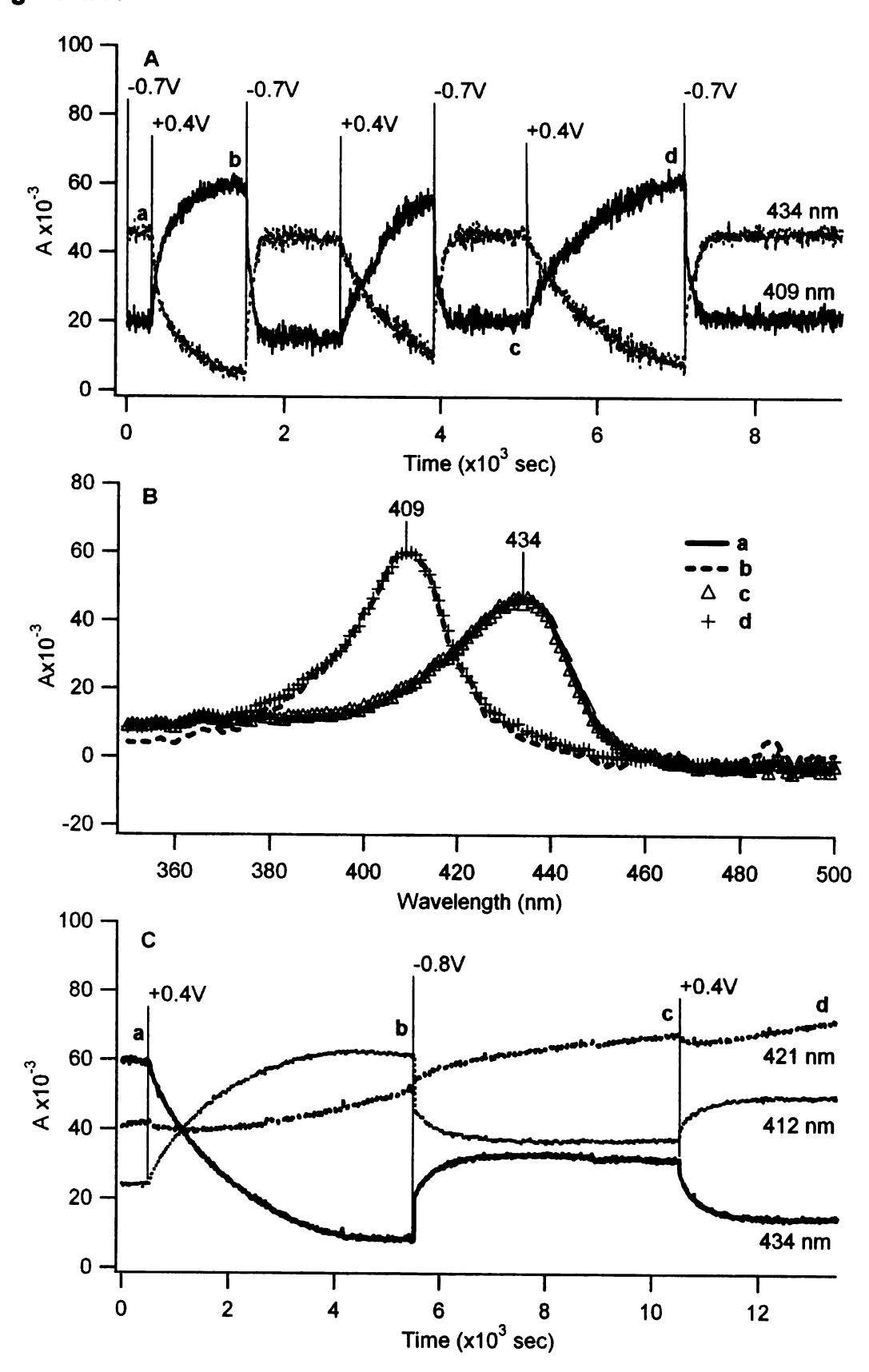
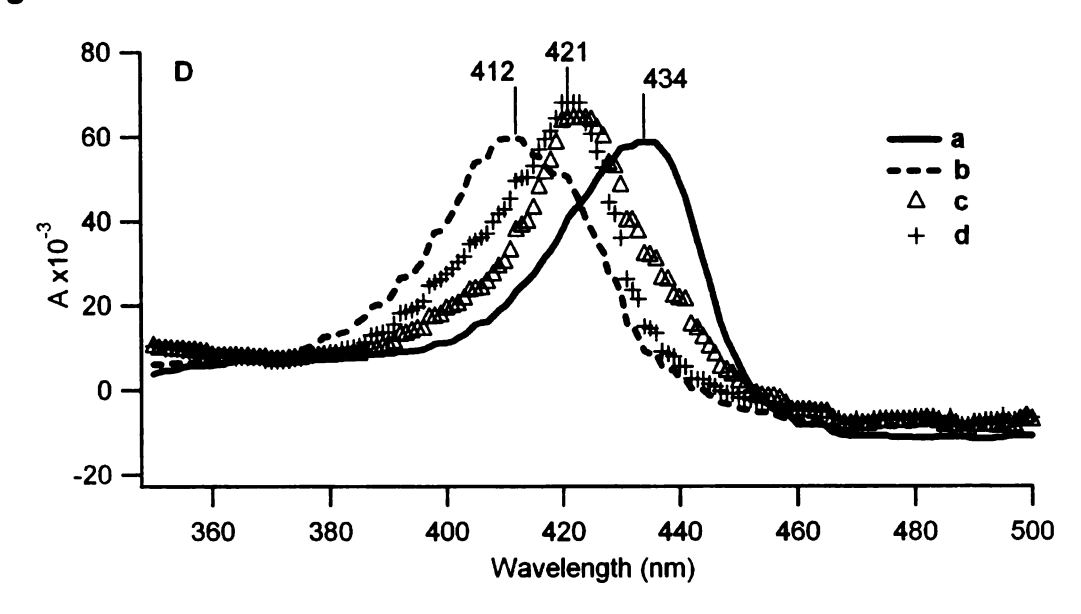


Figure 4.11 continued



## 4.3 Discussion

Electrochemical characterization of the new thin-layer cell showed that there were two notable deviations from the expected thin-layer behavior. Some distortion of the *i-E* curves lead to non-zero  $\Delta E_p$  values being observed.  $\Delta E_p$  values larger than 0 can be caused by ohmic resistance within the cell and electrode and or slow electron-transfer kinetics at the electrode surface. The stability of  $\Delta E_p$  with increasing analyte concentration, demonstrates that sluggish electron-transfer kinetics at the electrode surface are the main cause of the nonzero  $\Delta E_p$ . The second deviation was that the  $\Delta E_p$  was largest under at all conditions at minimal layer thickness (7.5  $\mu$ m). This behavior can be rationalized by considering the diffusion of analyte in the electrolyte volume above the electrode that connected the thin layer with reference and counter electrodes (Figure 2.3). For thick layers (e.g., 75  $\mu$ m), this volume is negligible compared to

the volume of the thin layer. As the layer thickness decreases to 25 and 7.5  $\mu$ m, the relative contribution of this volume increases to a significant level.

Spectroelectrochemical measurements can provide the information about current and absorbance change at the same time. The current can be recorded as soon as the electron transfer occurs at the electrode surface. However, it needs some time for the product to build up in the cell to be detected by spectrophotometer. This explains the delayed absorbance response is observed in Figure 4.6. Diamond electrode offers several major benefits in biological applications, such as outstanding chemical inertness, stability, as illustrated in Figure 4.9, and a wide potential window. 32-37 Due to the continuous nature of diamond film electrodes, their ohmic resistance has to be balanced against their optical transmission. Light transmitted through the film electrode can also probe analytes on the electrode surface, allowing spectroscopic studies of analytes immobilized on the electrode via chemical or lipid assemblies, thus eliminating diffusion altogether, which can counterbalance resistance of the film electrode.

Cytochorme c-Cyanide Complex. The difference absorption spectra for the cytochrome c-cyanide complex can be interpreted by a redox-driven ligand exchange of cytochrome c in the presence of cyanide ion.<sup>29</sup> The ferric cytochrome c solution was initially equilibrated with 0.1 M KCN at +0.3 V. When the potential was stepped to -0.3 V (a $\rightarrow$ b), the native ferric cytochrome c was reduced (E°'<sub>Cyt c</sub>= 60 mV), the cytochrome c-cyanide complex remained oxidized

due to the more negative formal potential ( $E^{\circ}'_{\text{Cyt c-CN}}$ = -440 mV). As the potential was decreased to -0.7 V (b→c), a 5× larger absorbance change was observed due to the reduction of the ferric cytochrome c-cyanide complex. The relative amplitudes of two reduction phases indicate that the equilibrium was shifted toward the CN-bound ferric cytochrome c. Affinity of ferrous cytochrome c for CN<sup>-</sup> is significantly lower (binding constant: 4.7×10<sup>-3</sup> M<sup>-1</sup> <sup>29</sup>) and dissociation of the ferrous cytochrome c-cyanide complex occurred (c-d) increasing the population of native ferrous cytochrome c. When the potential was stepped back to -0.3 V, the oxidation of the remaining ferrous cytochrome c-cyanide complex occurred, with a reduced amplitude compared to that for (b→c). The amplitude of absorbance change for the e→f step was increased for the same reason. Upon oxidation of ferric cytochrome c, binding of CN to the increased population of ferric cytochrome c began to re-establish equilibrium in the sample  $(f\rightarrow g)$  similar to point a.

**Myoglobin.** The equilibration time for myoglobin is longer compared to cytochrome *c*. The relatively slow heterogeneous electron-transfer kinetics are considered to be due to a large activation energy barrier for conversion of highspin iron to low-spin states.<sup>19</sup> Fast electrochemical response for myoglobin has been reported. Rusling and coworkers performed direct protein electrochemistry by using insoluble surfactants to incorporate the myoglobin onto an electrode.<sup>24, 27, 28</sup> Taniguchi *et al.* showed quasi-reversible voltammetry of horse heart myoglobin with an ultra-clean and hydrophilic indium oxide electrode.<sup>25, 26</sup> In

Figure 4.11, the far-UV light's effect, to disable the reversible reaction of myoglobin, is obvious with the uncommon peak positions. Far-UV light is likely to cause photoreduction or radical damage of Mb (Figure 4.12) and inhibit the reversible reaction between deoxyMb and metMb. Therefore, it is necessary to check for far-UV damage to the proteins prior to UV-Vis spectroelectrochemical measurements. The conversion between deoxyMb and metMb with far-UV light blocked demonstrated the ability of performing anaerobic experiments in the cell.

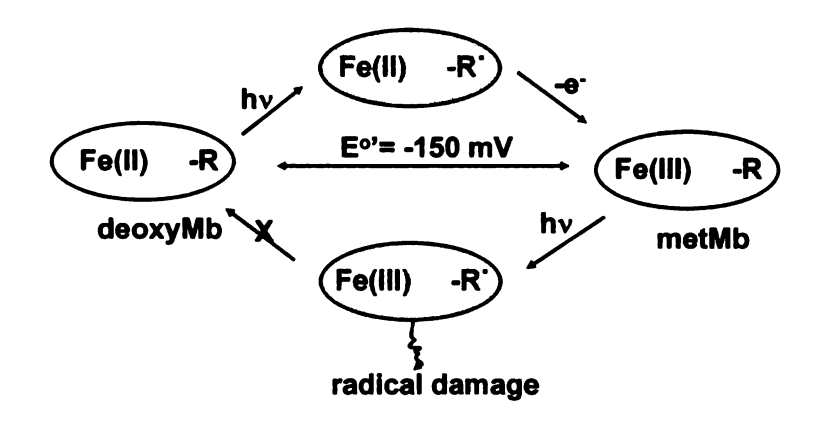


Figure 4.12 Proposed mechanism for photoreduction of myoglobin.

#### 4.4 Conclusions

The electrochemical characterization of the new thin-layer cell showed Gaussian-shaped thin-layer behavior and a linear relationship of peak current *vs.* scan rate. The spectroelectrochemical measurements of ferrocyanide showed that showed the heterogeneous response along the radial coordinate. The fouling resistance to proteins of boron-doped diamond electrode compared to the gold minigrid electrode was clearly demonstrated by the non-decreasing signal of cytochrome *c* over several cycles. The spectroelectrochemical measurements of

the cytochrome *c*-cyanide complex showed the midpoint potentials for the CN-bound cytochrome *c* at more negative values. The conversion between deoxyMb and metMb with far-UV light blocked, demonstrated the ability of anaerobic experiment in the cell. In conclusion, the thin-layer transmission cell design met the criteria for the ideal thin-layer transmission cell.

#### 4.5 References

- (1) Kuwana, T.; Darlington, K. R.; Leedy, D. W. *Anal. Chem.* **1964**, *36*, 2023-2025.
- (2) Anderson, J. L.; Kuwana, T.; Hartzell, C. R. *Biochemistry* **1976**, *15*, 3847-3855.
- (3) Bowden, E. F.; Hawkridge, F. M. J. Electroanal. Chem. 1981, 125, 367-386.
- (4) Zak, J.; Porter, M. D.; Kuwana, T. *Anal. Chem.* **1983**, *55*, 2219-2222.
- (5) Gui, Y.; Kuwana, T. *J. Electroanal. Chem.* **1987**, 226, 199-209.
- (6) Moss, D.; Nabedryk, E.; Breton, J.; Mantele, W. *Eur. J. Biochem.* **1990**, *187*, 565-572.
- (7) Schlereth, D. D.; Mantele, W. *Biochemistry* **1992**, *31*, 7494-7502.
- (8) Dai, Y.; Swain, G.; Porter, M. D.; Zak, J. *Anal. Chem.* **2008**, *80*, 14-22.
- (9) Haymond, S.; Zak, J. K.; Show, Y.; Butler, J. E.; Babcock, G. T.; Swain, G. M. *Anal. Chim. Acta* **2003**, *500*, 137-144.
- (10) Bard, A. J.; Faulkner, L. R. In *Electrochemical Methods: Fundamentals and Applications*, 2 ed.; John Wiley & Sons: New York, 2001.
- (11) Wittenberg, B. A.; Wittenberg, J. B.; Caldwell, P. R. *J. Biol. Chem.* **1975**, *250*, 9038-9043.
- (12) Postnikova, G. B.; Tselikova, S. V.; Kolaeva, S. G.; Solomonov, N. G. Comp. Biochem. Physiol., Part A 1999, 124, 35-37.
- (13) Kendrew, J. C.; Watson, H. C.; Strandberg, B. E.; Dickerson, R. E.; Phillips, D. C.; Shore, V. C. *Nature* **1961**, *190*, 666-670.
- (14) Takano, T. J. Mol. Biol. 1977, 110, 537-568.
- (15) Takano, T. J. Mol. Biol. 1977, 110, 569-584.
- (16) Antonini, E.; Brunori, M. *Hemoglobin and myoglobin in their reactions with ligands*; North-Holland Pub. Co.: Amsterdam, 1971.
- (17) Shikama, K. Chem. Rev. 1998, 98, 1357-1374.

- (18) King, B. C.; Hawkridge, F. M.; Hoffman, B. M. J. Am. Chem. Soc. **1992**, *114*, 10603-10608.
- (19) Cohen, D. J.; King, B. C.; Hawkridge, F. M. *J. Electroanal. Chem.* **1998**, 447, 53-62.
- (20) Armstrong, F. A.; Hill, H. A. O.; Oliver, B. N. J. Chem. Soc., Chem. Commun. 1984, 976-977.
- (21) Armstrong, F. A.; Cox, P. A.; Hill, H. A. O.; Lowe, V. J.; Oliver, B. N. J. *Electroanal. Chem.* **1987**, 217, 331-366.
- (22) Armstrong, F. A.; Hill, H. A. O.; Walton, N. J. Acc. Chem. Res. 1988, 21, 407-413.
- (23) Rusling, J. F.; Nassar, A.-E. F. *J. Am. Chem. Soc.* **1993**, *115*, 11891-11897.
- (24) Nassar, A. E. F.; Willis, W. S.; Rusling, J. F. *Anal. Chem.* **1995**, *67*, 2386-2392.
- (25) Taniguchi, I.; Watanabe, K.; Tominaga, M.; Hawkridge, F. M. *J. Electroanal. Chem.* **1992**, 333, 331-338.
- (26) Tominaga, M.; Kumagai, T.; Takita, S.; Taniguchi, I. *Chem. Lett.* **1993**, 1771-1774.
- (27) Rusling, J. F. Acc. Chem. Res. 1998, 31, 363-369.
- (28) He, P.; Hu, N.; Rusling, J. F. *Langmuir* **2004**, *20*, 722-729.
- (29) Schejter, A.; Ryan, M. D.; Blizzard, E. R.; Zhang, C.; Margoliash, E.; Feinberg, B. A. *Protein Science* **2006**, *15*, 234-241.
- (30) Hawkridge, F.; Kuwana, T. *Anal. Chem.* **1973**, *45*, 1021-1027.
- (31) Stotter, J.; Haymond, S.; Zak, J. K.; Show, Y.; Cvackova, Z.; Swain, G. M. *Interface* **2003**, *12*, 33-38.
- (32) Xu, J.; Granger, M. C.; Chen, Q.; Strojek, J. W.; Lister, T. E.; Swain, G. M. *Anal. Chem.* **1997**, *69*, 591A-597A.
- (33) Swain, G. M.; Anderson, A. B.; Angus, J. C. MRS Bulletin 1998, 23, 56-59.
- (34) Rao, T. N.; Loo, B. H.; Sarada, B. V.; Terashima, C.; Fujishima, A. *Anal. Chem.* **2002**, *74*, 1578-1583.
- (35) Fujishima, A.; Rao, T. N.; Try, D. A. *Proc.-Electrochem. Soc.* **2000**, 99-32, 383-388.

- (36) McGaw, E. A.; Swain, G. M. Anal. Chim. Acta 2006, 575, 180-189.
- (37) Dai, Y.; Proshlyakov, D. A.; Zak, J. K.; Swain, G. M. *Anal. Chem.* **2007**, 79, 7526-7533.

# **CHAPTER 5**

# SPECTROELECTROCHEMICAL STUDIES OF Na<sup>+</sup>-

# TRANSLOCATING NADH:QUINONE

# OXIDOREDUCTASE FROM VIBRIO CHOLERAE

#### 5.1 Introduction

Na<sup>+</sup>-translocating NADH:quinone oxidoreductase (Na<sup>+</sup>-NQR) acts as a redox-driven sodium pump in prokaryotes, such as marine bacteria (e.g., Vibrio alginolyticus) and human pathogenic bacteria (e.g., Vibrio cholerae).<sup>1</sup> Na<sup>+</sup>-NQR is a membrane-bound enzyme that couples electron transfer from NADH to ubiquinone with Na<sup>+</sup> translocation across the membrane. The efficiency of Na<sup>+</sup> translocation by the Na<sup>+</sup>-NQR has been shown to be 1 Na<sup>+</sup>/ 1 e<sup>-,2</sup> The electrochemical sodium gradient generated by Na<sup>+</sup>-NQR provides the energy for cellular metabolic functions, such as driving bacterial flagellum and transporting nutrients.<sup>3, 4</sup>

Na<sup>+</sup>-NQR has a molecular mass of ~210 kDa and is an assembly of six polypeptide subunits (NqrA-F): hydrophobic subunits NqrB, NqrD, NqrE and relatively hydrophilic subunits NqrA, NqrC, NqrF.<sup>2, 4</sup> The known prosthetic groups of Na<sup>+</sup>-NQR include a noncovalently bound flavin adenine dinucleotide (FAD)

and a [2Fe-2S] cluster in NqrF where the binding site for NADH is also located; two covalently-bound flavin mononucleotides (FMNs) that are attached by phosphoester bonds to threonine residues in subunits NqrB and NqrC respectively; a noncovalently bound riboflavin that has not been definitively localized in the structure of the enzyme.<sup>1,5-9</sup> The chemical structures of riboflavin, FMN, FAD and ubiquinone-8 are showed in Figure 5.1.

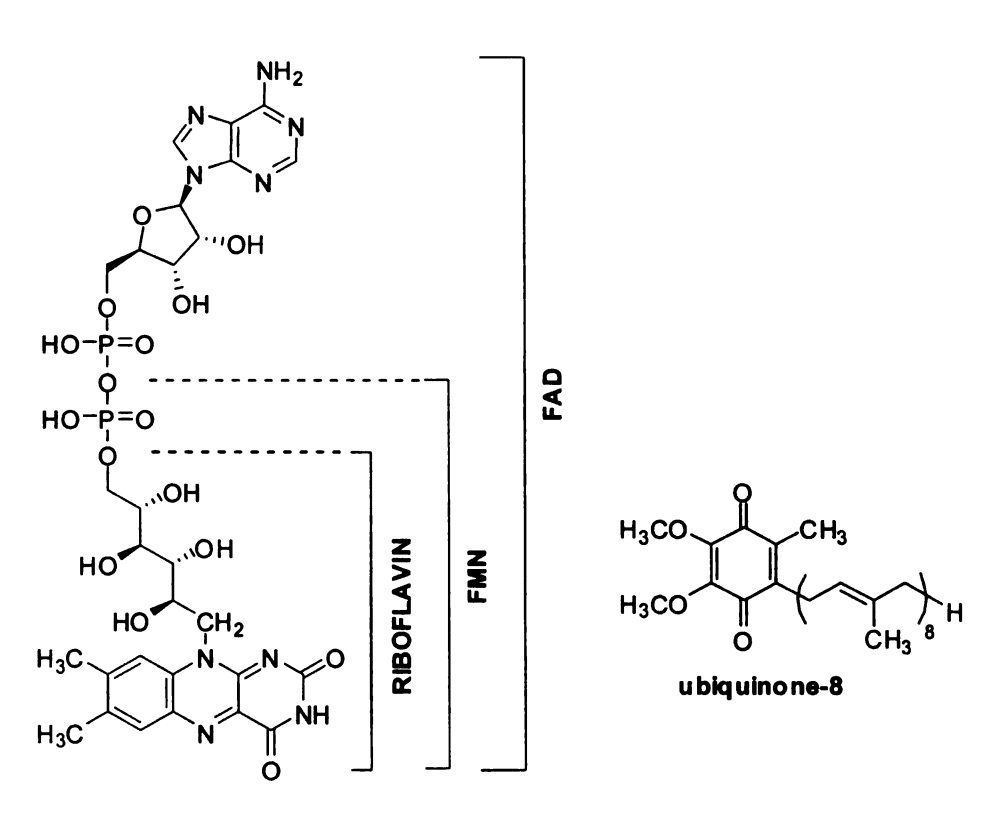


Figure 5.1 Chemical structures of riboflavin, FMN, FAD and ubiquinone-8.

The NqrF catalyzes the initial oxidation of NADH: a two-electron reduction of the noncovalently bound FAD on the C-terminal domain of the NqrF, followed by one-electron transfer to the [2Fe-2S] cluster in the N-terminal Fe-S domain of NqrF.<sup>1, 5, 10, 11</sup>

NADH/NAD+ 
$$\frac{2e}{}$$
 FAD/FADH<sub>2</sub>  $\frac{1e}{}$  [2Fe-2S]<sub>ox</sub> / [2Fe-2S]<sub>red</sub>

The electron transfer pathway from the [2Fe-2S] cluster to other cofactors in the enzyme and the substrate quinone is unclear and this has been discussed controversially in the literature. Juarez *et al.* recently proposed that the electrons flow in the following order using a stopped flow measurement:<sup>7</sup>

$$FAD \rightarrow [2Fe-2S] \rightarrow FMN_C \rightarrow FMN_B \rightarrow riboflavin$$

However, they found that the cofactors were reduced in the following order:

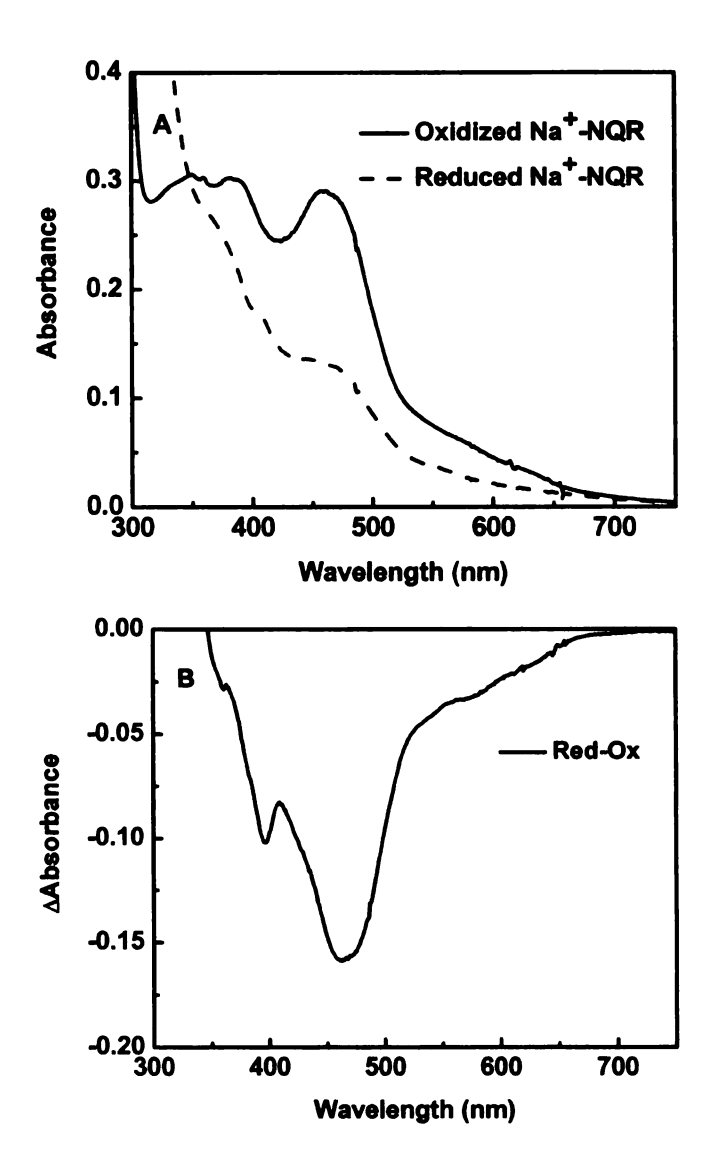
FAD/FADH<sub>2</sub>
$$\rightarrow$$
[2Fe-2S]<sub>ox</sub>/[2Fe-2S]<sub>red</sub> $\rightarrow$ riboflavin  
 $\rightarrow$ 2(FMN/FMN'<sup>-</sup>) $\rightarrow$ FMN<sub>c</sub>'<sup>-</sup>/FMN<sub>c</sub>H<sub>2</sub>

Two FMNs were first transformed to two anionic flavosemiquinone state FMN<sup>--</sup> but only FMN<sub>c</sub><sup>--</sup> was finally converted to FMNH<sub>2</sub>. They also concluded that the reduction of the FMN<sub>c</sub> to its anionic flavosemiquinone state FMN<sub>c</sub><sup>--</sup> is the first Na<sup>+</sup>-dependent step and could be linked to Na<sup>+</sup> uptake.

Na<sup>+</sup>-NQR, which contains four flavins, one [2Fe-2S] center, and ubiquinone-8 as cofactors, is the entry point for the electrons into the aerobic respiratory chain of marine bacteria. Further studies are needed in order to better understand how the energy conversion is coupled with the transmembrane Na<sup>+</sup> translocation. To understand the mechanism of Na<sup>+</sup> pumping, it is important to characterize the redox potentials of all cofactors in Na<sup>+</sup>-NQR and to determine their dependence the Na⁺ concentration. this on chapter, spectroelectrochemical studies of Na<sup>+</sup>-NQR are presented together with the global regression analysis results. The electrochemistry of Na<sup>+</sup>-NQR was first studied using a glassy carbon electrode. The spectroelectrochemical measurements were then performed with a diamond/quartz OTE in the thin-layer cell using a potential step method. Global nonlinear regression analysis was applied to the high resolution (10 mV/step) spectroelectrochemical data to resolve redox centers in the Na<sup>+</sup>-NQR and determine their sodium sensitivity.

#### 5.2 Results

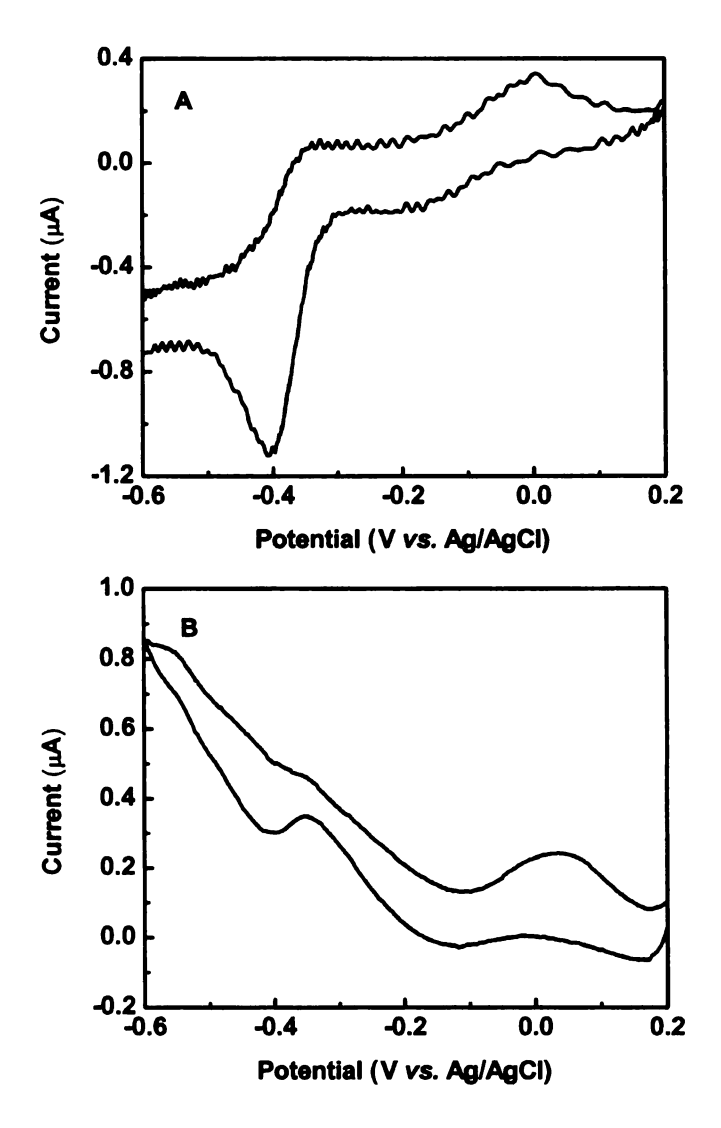
The UV-Vis absorption spectra of the purified Na<sup>+</sup>-NQR after air oxidization and reduction with sodium dithionite are shown in Figure 5.2. The broad peaks centered around 370 and 460 nm are characteristic of flavoproteins.<sup>4</sup> The absorption peak around 460 nm is due to the first singlet state transition  $S_0 \rightarrow S_1$ , and the 370 nm band is associated with the  $S_0 \rightarrow S_2$  transition.<sup>12</sup> The absorption by the [2Fe-2S] cluster is also likely to be included in the broad peaks, as the visible spectra of [2Fe-2S] cluster is usually featureless due to multiple overlapping  $S \rightarrow Fe^{III}$  charge transfer transitions.<sup>13</sup>



**Figure 5.2** (A) UV-Vis absorption spectra for air-oxidized (solid line) and sodium dithionite reduced (dashed line) Na<sup>+</sup>-NQR purified from *Vibrio cholerae*. The solution was 0.01 mM Na<sup>+</sup>-NQR in 50 mM sodium phosphate buffer (pH 8), 100 mM NaCl, 1 mM EDTA, 5% glycerol and 0.05% dodecylmaltoside; (B) difference absorbance spectrum (Red-Ox) for Na<sup>+</sup>-NQR.

Figure 5.3 presents background-corrected cyclic voltammetric *i-E* curves for 0.1 mM Na<sup>+</sup>-NQR in sodium phosphate buffer using glassy carbon and diamond/quartz OTE in the thin-layer cell with a 75 μm spacer. A low potential scan rate of 0.5 mV/s was employed. Both *i-E* curves show two pairs of

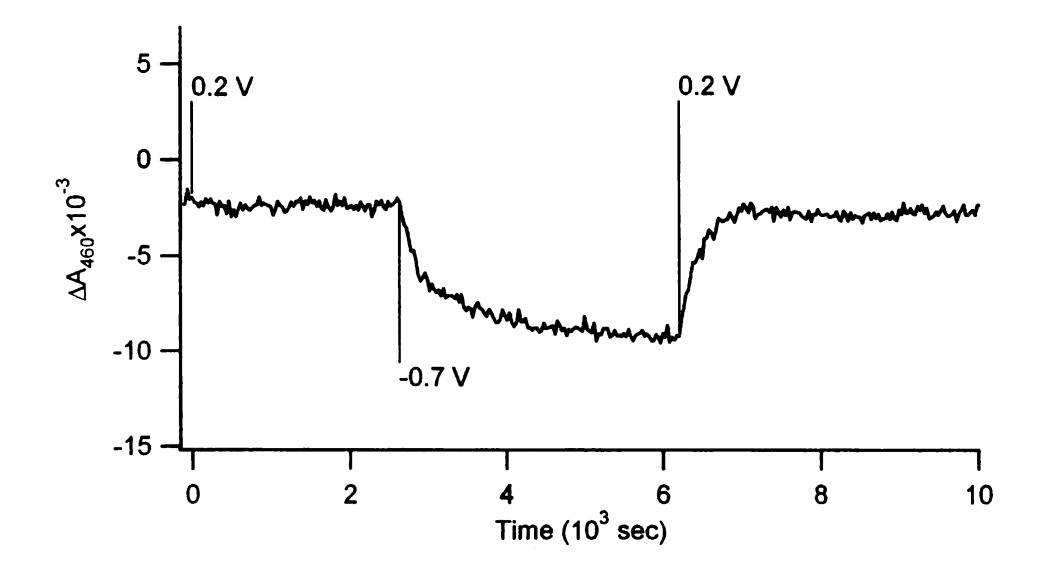
oxidation/reduction peaks with similar peak potentials. Cyclic voltammetry was also performed in small potential ranges (0.2 to -0.2 V and -0.2 to -0.7 V) to investigate the relationship of these two redox couples and the results indicated that they reacted separately. However, Na<sup>+</sup>-NQR contains four flavins and one [2Fe-2S] as cofactors, it is proposed that the redox potentials for some redox centers are similar and can not be resolved by cyclic voltammetry. In general, the voltammetric results show that the potential range desired for the measuring Na<sup>+</sup>-NQR redox activity is from 0.2 to -0.7 V.



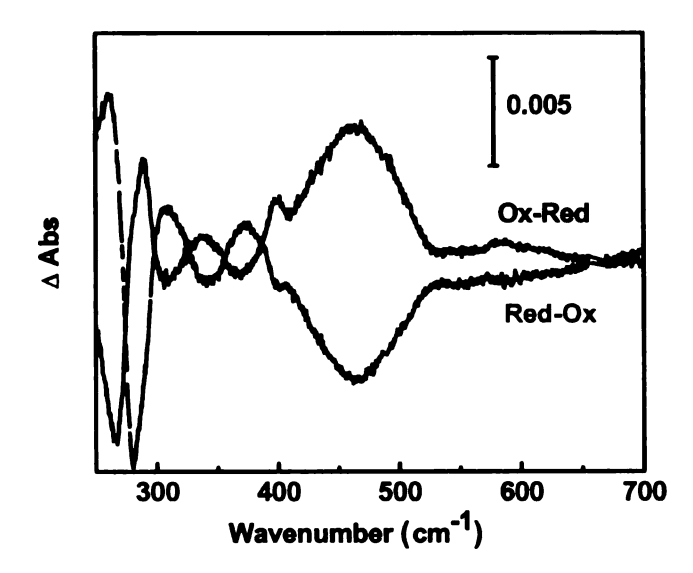
**Figure 5.3** Background-corrected cyclic voltammetric *i-E* curves for Na<sup>+</sup>-NQR at (A) a freshly polished glassy carbon electrode and (B) a diamond/quartz electrode in a thin-layer cell with a 75 μm spacer. The analyte solution was 0.1 mM Na<sup>+</sup>-NQR in 50 mM sodium phosphate buffer (pH 8), 500 mM NaCl, 1 mM EDTA, 5% glycerol and 0.05% dodecylmaltoside. The scan rate was 0.5 mV/s.

Figure 5.4 shows the spectroelectrochemical response of Na<sup>+</sup>-NQR at 460 nm with a diamond/quartz OTE in a transmission cell using a 75 μm spacer. 460 nm was selected due to the maximum spectral response changes. Potential steps between 0.2 and -0.7 V (as indicated in the figure) produced relatively slow,

but generally reversible optical changes. It is obvious that the oxidation is faster than the reduction reaction, based on the observation that the steady-state optical response for the reduced form is reached faster after application of the potential than for the response for the oxidized form. Figure 5.5 shows the Ox-Red and Red-Ox UV-Vis difference absorption spectra for 0.1 mM Na<sup>+</sup>-NQR in 50 mM sodium phosphate buffer (pH 8), 500 mM NaCl, 1 mM EDTA and 0.05% dodecylmaltoside. The difference spectra were generated from the difference between the spectra for the oxidized (0.2 V) and reduced (-0.7 V) forms of the enzyme. The spectra are mirror images of each other, which is consistent with a reversible redox reaction and complete electrolysis of the analyte in the thin-layer cell.

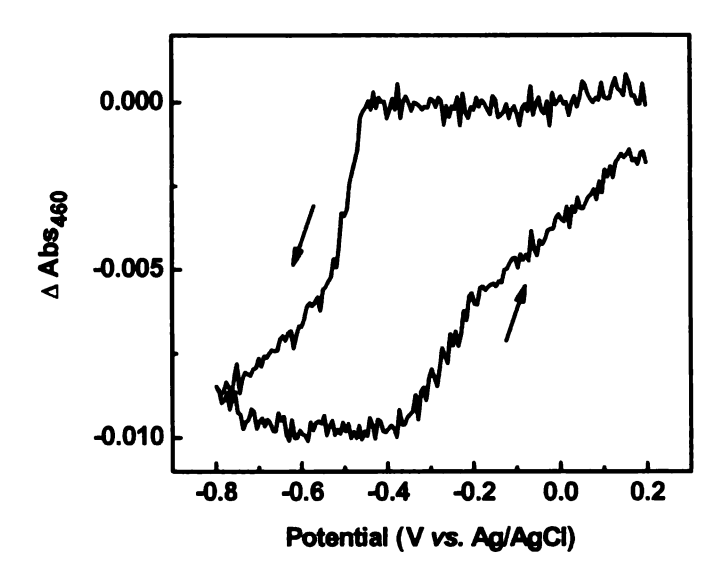


**Figure 5.4** Absorbance change of Na<sup>+</sup>-NQR (460nm) at a diamond/quartz OTE in a transmission cell with a 75  $\mu$ m spacer. Potential steps to 0.2 and -0.7 V were applied as indicated in the figure. The analyte solution was 0.1 mM Na<sup>+</sup>-NQR in 50 mM sodium phosphate buffer (pH 8), 500 mM NaCl, 1 mM EDTA and 0.05% dodecylmaltoside.



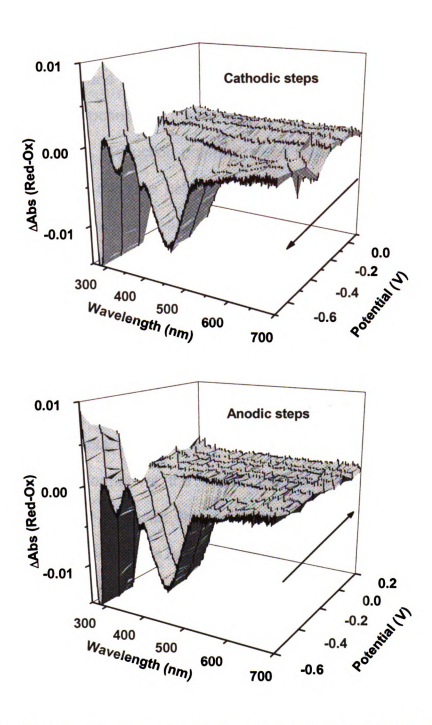
**Figure 5.5** UV-Vis difference absorbance spectra measured for Na $^{+}$ -NQR at a diamond/quartz OTE in a transmission cell with a 75  $\mu$ m spacer. Ox-Red and Red-Ox difference spectra were generated from the oxidized and reduced spectra collected at 0.2 and -0.7 V. The analyte solution was 0.1 mM Na $^{+}$ -NQR in 50 mM sodium phosphate buffer (pH 8), 500 mM NaCl, 1 mM EDTA and 0.05% dodecylmaltoside.

The difference absorbance-potential (voltabsorptometry) curve was also recorded during one cyclic voltammetric cycle and is shown in Figure 5.6. The scan was initiated at 0.2 V and scanned in the negative direction to -0.8 V at a scan rate of 2 mV/s. During the forward scan, there was no change in absorbance until -0.5 V at which point there was a decrease in absorbance with increasing negative potential. On the reverse scan, there is considerable hysteresis. The absorbance is constant on the reverse scan until -0.4 V at which point the absorbance increases progressively to 0.2 V limit. The absorbance at this potential is less than that of the solution initially at the same potential. This could be due to incomplete electrolysis on the time scale of the measurement.



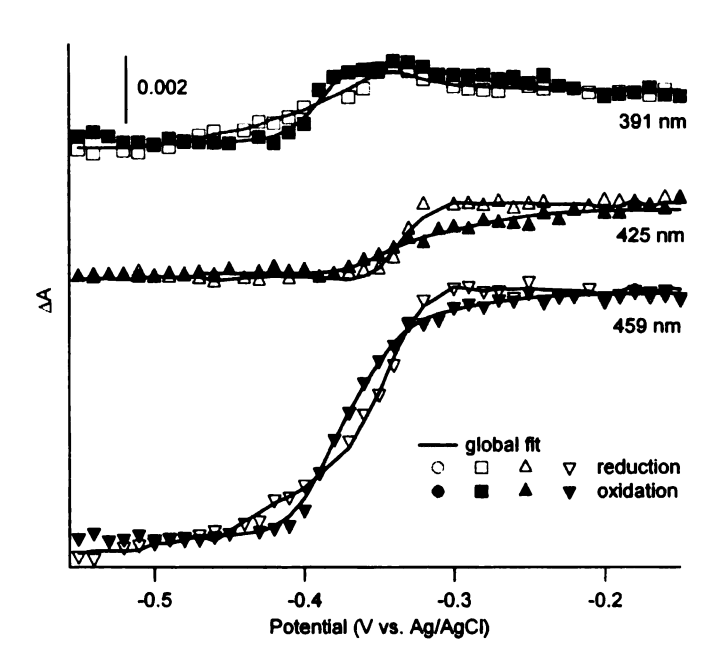
**Figure 5.6** Difference absorbance-potential curve (460 nm) for Na $^{+}$ -NQR at a diamond/quartz OTE in a transmission cell with a 75  $\mu$ m spacer. The analyte solution was 0.1 mM Na $^{+}$ -NQR in 50 mM sodium phosphate buffer (pH 8), 500 mM NaCl, 1 mM EDTA and 0.05% dodecylmaltoside. The data were collected at a scan rate of 2 mV/s.

Figure 5.7 shows the absorbance changes during a series of potential steps from 0.2 to -0.7 V and then back to 0.2 V in 100 mV increments. Both the reduction and oxidation changes are plotted. Sufficient time (20 min) was allowed at each potential to ensure that equilibration conditions were reached. The oxidation process reversed the optical changes of the reduction process and their optical changes were almost identical at all potentials. Background-corrected cyclic voltammetry of Na\*-NQR in Figure 5.3 showed an oxidation peak around 0 V, however, no optical changes were detected around this potential. This might be due to the tightly bound ubiquinone-8 with expected potential of -150 mV.



**Figure 5.7** UV-Vis difference absorbance spectra of Na\*-NQR during cathodic and anodic potential steps at a diamond/quartz OTE in a transmission cell with a 75  $\mu m$  spacer. The difference spectra were generated from the oxidized spectra collected at reference potential 0.2 V for reduction and oxidation potential steps every 100 mV and 20 min. The analyte solution was 0.1 mM Na\*-NQR in 50 mM sodium phosphate buffer (pH 8), 500 mM NaCl, 1 mM EDTA and 0.05% dodecylmaltoside.

In order to resolve redox potentials and spectra of multiple redox centers with similar potentials and spectral signature in Na<sup>+</sup>-NQR with global regression analysis, spectroelectrochemical measurements were performed during much smaller potential steps. Reduction potential steps were applied from -0.15 to -0.55 V at 10 mV, 20 min/step using reference potential at -0.1 V. Similarly, oxidation potential steps were applied from -0.55 to -0.15 V using reference potential at -0.6 V. Specifically, several models of three to five redox transitions involving one to three transferred electrons were applied to the high resolution spectroelectrochemical data. The optical changes at selected wavelengths during the reduction and oxidation of Na<sup>+</sup>-NQR, and the corresponding global fitting results are shown in Figure 5.8. The solid lines represent the result of the global fitting for the experimental data shown in markers. The reduction and oxidation of the protein were performed at the same potential range, and show similar absorbance changes. However, the asymmetry in the course of the two processes was clearly seen. The resolved spectra of Na<sup>+</sup>-NQR at the determined redox potentials are shown in Figure 5.9.



**Figure 5.8** Absorbance changes of Na<sup>+</sup>-NQR upon reduction (*vs.* -0.1 V) and oxidation (*vs.* -0.6 V) potential steps every 10 mV and 20 min. Markers: experimental data, solid line: global fitting results. The analyte solution was 0.1 mM Na<sup>+</sup>-NQR in 50 mM sodium phosphate buffer (pH 8), 500 mM NaCl, 1 mM EDTA and 0.05% dodecylmaltoside.

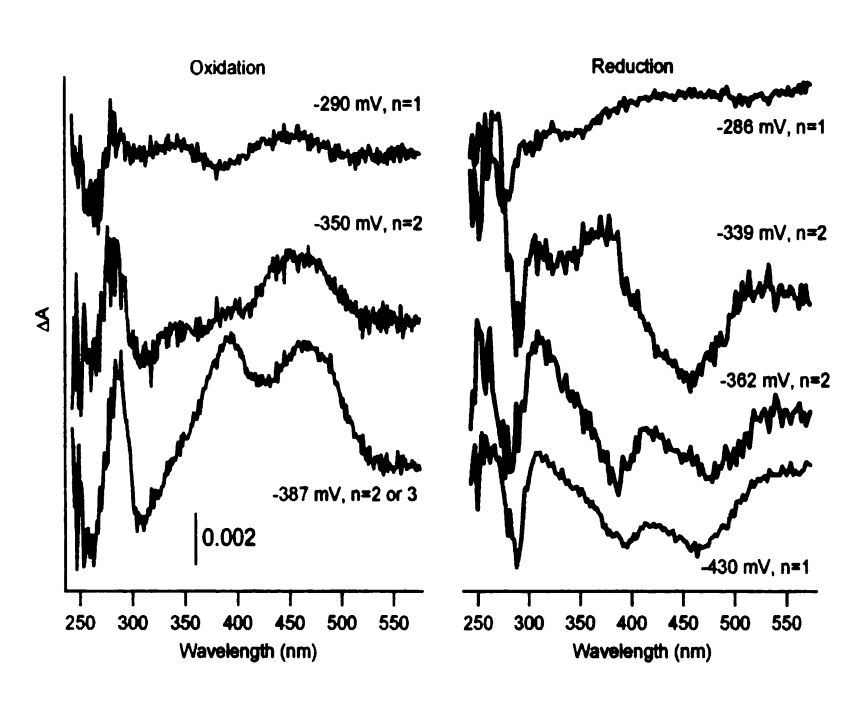


Figure 5.9 Resolved spectra of redox transitions in Na<sup>+</sup>-NQR.

Na<sup>+</sup> sensitivity was also examined at 50 and 0.5 mM Na<sup>+</sup>. However, the global regression analysis of spectroelectrochemical data did not show Na<sup>+</sup> dependence of the redox potentials (60 mV per 10-fold change of Na<sup>+</sup> concentration).

#### 5.3 Discussion

The spectra at -290 or -286 mV (n=1) show small visible features and UV changes, and this could be attributed to riboflavin transitions. The -350 or -339 mV (n=2) spectra show broad peaks around 450 and 285 nm, which may arise from FAD transition. The reduction spectra at -362 (n=2) and -430 (n=1) mV are similar in shape with broad peaks at 390 and 470 nm, which is likely due to the two FMNs transition and [2Fe-2S]; however, the oxidation spectra of FMN is a single phase at -387 mV (n=2 or 3). The determined redox potentials for the reduction and oxidation of the Na\*-NQR are summarized in Table 5.1.

**Table 5.1** Determined redox potentials for Na<sup>+</sup>-NQR.

Cofactor	Redox Transition	E <sub>m</sub> (mV)* Oxidation	E <sub>m</sub> (mV)* Reduction
FAD <sub>NqrF</sub> [2Fe-2S] <sub>NqrF</sub>	FAD/FADH <sub>2</sub> (n=2) [2Fe-2S] <sub>ox</sub> /[2Fe-2S] <sub>red</sub> (n=1)	-390	-340 -430
$FMN_{NqrB,NqrC}$	2(FMN/FMN <sup></sup> )2(n=1)	-350	-360
Rf <sub>Ngr?</sub>	RfH <sup>-</sup> /RfH <sup>-</sup> (n=1)	-290	-290

<sup>\*</sup>E was reported vs. Ag/AgCl, saturated KCl.

Bogachev *et al.* recently reported spectroelectrochemical redox titration of Na<sup>+</sup>-NQR and made a global fitting based on one two-electron and five one-electron transitions.<sup>14, 15</sup> They determined the redox potentials with corresponding redox transitions in Na<sup>+</sup>-NQR, as listed in Table 5.2, and possible electron transfer pathways in Na<sup>+</sup>-NQR: FAD/FADH<sup>-</sup>->[2Fe-2S]<sub>ox</sub>/[2Fe-2S]<sub>red</sub>-> (FMN/FMN<sup>--</sup>)<sub>C</sub>-> (FMN/FMN<sup>--</sup>)<sub>B</sub>-> RfH<sup>-</sup>/RfH<sup>-</sup>. They also reported that the redox potentials of all the redox transitions were independent of Na<sup>+</sup> concentration.

**Table 5.2** Redox transitions for known cofactors in Na<sup>+</sup>-NQR determined by Bogachev. <sup>15</sup>

Cofactor	Redox Transition	E <sub>m</sub> * (mV)
FAD <sub>NorF</sub>	FAD/FADH (n=2)	-400
[2Fe-2S] NgrF	[2Fe-2S] <sub>ox</sub> /[2Fe-2S] <sub>red</sub> (n=1)	-470
FMN <sub>NgrC</sub>	FMN' <sup>-</sup> / FMNH <sup>-</sup> (n=1)	<b>-450</b>
FMN <sub>NgrC</sub>	FMN/FMN <sup></sup> (n=1)	<del>-4</del> 00
FMN <sub>NgrB</sub>	FMN/FMN <sup>··</sup> (n=1)	-330
Rf <sub>Nqr?</sub>	RfH /RfH (n=1)	-210

<sup>\*</sup>E was reported vs. Ag/AgCl, saturated KCl.

The global nonlinear regression analysis employed in this chapter is similar to the procedure used by Bogachev. However, a low-order polynomial baseline correction was made for the low intensity of optical changes due to small protein volume ~5 μL and short pathlength ~75 μm (compared to 40 μL and 600 μm in Bogachev's work). Our spectroelectrochemical data and global fitting results are somewhat different from Bogachev's findings. The data reported by Bogachev were generated using Na<sup>+</sup>-NQR from *Escherichia coli*, while in this work all experiment data were performed with Na<sup>+</sup>-NQR from *Vibrio cholerae*.

Our results indicate that the spectral changes recorded during the reduction and oxidation potential steps are not mirror images of each other, even though they showed similar total absorbance changes. However, practically identical reduction and oxidation titrations, with hysteresis less than 10 mV, was reported by Bogachev.<sup>6</sup> In general, the combination of the spectroelectrochemical method and global nonlinear regression analysis provides a sensitive method for the analysis of a multicomponent redox system.

Juarez et al. recently reported that the reduction of the FMN<sub>c</sub> to its anionic flavosemiquinone state was the first Na<sup>+</sup>-dependent step and could be linked to Na<sup>+</sup> uptake using kinetic measurements.<sup>7</sup> The reason for the absence of Na<sup>+</sup>-dependent in both Bogachev and our work is that Na<sup>+</sup>-NQR might be a kinetic pump. Na<sup>+</sup> dependence is carried out only at a specific stage of the catalytic cycle and is not accessible under thermodynamic conditions. Future spectroscopic measurements of vibrational modes could help us to better understand any Na<sup>+</sup> concentration dependence. It is expected that the spectral analysis will show the contributions of all cofactors to the individual electron-transfer steps.

#### 5.4 Conclusions

An analytical method was developed and used for the study of the multicomponent redox protein: Na<sup>+</sup>-NQR. The UV-Vis difference spectra, recorded with a diamond/quartz OTE, indicated that reversible and complete

electrolysis occurs in the thin-layer cell. This is the first spectroelectrochemical study of this protein without the use of mediators. Global regression analysis results resolved redox transitions and corresponding spectral changes in Na<sup>+</sup>-NQR. The determined redox potentials of the cofactors are important for the vibrational measurements to fully characterize the protein. The thermodynamic measurements did not reveal any Na<sup>+</sup> dependence of the formal potential for the redox transitions. In conclusion, the combination of spectroelectrochemical data and global regression analysis showed the ability of resolving redox centers in Na<sup>+</sup>-NQR.

#### 5.5 References

- (1) Turk, K.; Puhar, A.; Neese, F.; Bill, E.; Fritz, G.; Steuber, J. *J. Biol. Chem.* **2004**, *279*, 21349-21355.
- (2) Bogachev, A. V.; Bertsova, Y. V.; Aitio, O.; Permi, P.; Verkhovsky, M. I. *Biochemistry* **2007**, *46*, 10186-10191.
- (3) Barquera, B.; Zhou, W.; Morgan, J. E.; Gennis, R. B. *Proc. Natl. Acad. Sci. U. S. A.* **2002**, *99*, 10322-10324.
- (4) Barquera, B.; Hellwig, P.; Zhou, W.; Morgan, J. E.; Hase, C. C.; Gosink, K. K.; Nilges, M.; Bruesehoff, P. J.; Roth, A.; Lancaster, C. R. D.; Gennis, R. B. *Biochemistry* **2002**, *41*, 3781-3789.
- (5) Tao, M.; Fritz, G.; Steuber, J. J. Inorg. Biochem. 2008, 102, 1366-1372.
- (6) Bogachev, A. V.; Bertsova, Y. V.; Bloch, D. A.; Verkhovsky, M. I. *Biochemistry* **2006**, *45*, 3421-3428.
- (7) Juarez, O.; Morgan, J. E.; Barquera, B. *J. Biol. Chem.* **2009**, *284*, 8963-8972.
- (8) Bogachev, A. V.; Belevich, N. P.; Bertsova, Y. V.; Verkhovsky, M. I. *J. Biol. Chem.* **2009**, *284*, 5533-5538.
- (9) Juarez, O.; Nilges, M. J.; Gillespie, P.; Cotton, J.; Barquera, B. *J. Biol. Chem.* **2008**, 283, 33162-33167.
- (10) Lin, P.-C.; Puhar, A.; Turk, K.; Piligkos, S.; Bill, E.; Neese, F.; Steuber, J. *J. Biol. Chem.* **2005**, *280*, 22560-22563.
- (11) Lin, P.-C.; Turk, K.; Hase, C. C.; Fritz, G.; Steuber, J. *J. Bacteriol.* **2007**, *189*, 3902-3908.
- (12) Briggs, W. R.; Spudich, J. L. *Handbook of Photosensory Receptors*; Wiley-VCH, 2005.
- (13) Hatzfeld, O. M.; Unalkat, P.; Shergill, J. K.; Cammack, R.; Mason, J. R. *Biochemistry* **1996**, *35*, 7546-7552.
- (14) Bogachev, A. V.; Kulik, L. V.; Bloch, D. A.; Bertsova, Y. V.; Fadeeva, M. S.; Verkhovsky, M. I. *Biochemistry* **2009**, *48*, 6291-6298.
- (15) Bogachev, A. V.; Bloch, D. A.; Bertsova, Y. V.; Verkhovsky, M. I. *Biochemistry* **2009**, *48*, 6299-6304.

## **CHAPTER 6**

# **CONCLUSIONS AND OUTLOOK**

The long-term goal of the project is to develop a transmission spectroelectrochemical method with optically transparent boron-doped diamond thin-film electrodes which are useful for the study of redox proteins. Research conducted in this dissertation shows the progress that has been made towards this goal.

In Chapter 3, the electrochemical behavior of cytochrome c was investigated at both UNCD and MCD electrodes. Room temperature cyclic voltammetry of horse heart cytochrome c was performed as a function of the surface chemistry, film morphology and solution pH. Quasi-reversible, diffusion-controlled electron transfer for cytochrome c was observed at oxygen-terminated boron-doped diamond electrodes. A stable electrochemical response during repeated cycling indicated that no significant protein denaturation occurred at the electrode surface. UNCD electrodes exhibited a similar electrochemical response as the MCD electrodes, but showed higher peak current due to a relatively large surface area. The pH studies showed that the maximum peak current and relative low peak separation was observed between pH 7 and 7.5. On the other hand, no electrochemical response was observed for hydrogen-terminated

diamond electrodes. The requirement of surface carbon-oxygen functionalities at the electrode surface for direct electrochemistry of cytochrome c is in agreement with Armstrong's findings. The characterization of electrochemistry of cytochrome c at boron-doped diamond electrodes serves as a guide for future studies of more complicated redox systems.

In Chapter 4, a custom-designed thin-layer transmission cell was characterized and employed in the spectroelectrochemical measurements. The electrochemical characterization with a reversible, one-electron redox system Fe(CN)<sub>e</sub>-3/-4 at a glassy carbon electrode in the thin-layer cell showed Gaussianshaped thin-layer behavior and a linear relationship of peak current vs. scan rate. Kinetic measurements indicated rapid electrolysis in the cell and good agreement between electrochemical and spectral data. The cell was then used to investigate the spectroelectrochemical behavior of several model redox proteins. The cytochrome c studies showed the advantage of diamond/quartz OTE compared with the gold minigrid as the non-decreasing signal of cytochrome c over several cycles was detected on the diamond electrode. The spectroelectrochemical studies of cytochrome c-cyanide complex demonstrated that the electron transfer of cytochrome c-cyanide complex and native cytochrome c occurred at two different potentials. The investigation of Mb clearly demonstrated the applicability of the cell under anaerobic condition. An interesting finding was that an irreversible spectroelectrochemical response was observed under UV light. This might be caused by radical damage or photoreduction of the protein due to UV irradiation. The reproducible and quantitative spectroelectrochemical responses in the thin-layer cell provide the foundation for the application of the spectroelectrochemical technique to investigate more complicated redox proteins.

Chapter 5 presented a sensitive analysis method for the study of the multicomponent redox protein: Na<sup>+</sup>-NQR. The spectroelectrochemical data with diamond/quartz OTE without mediators, indicate that the reversible reaction and complete electrolysis occurs in the thin-layer cell. The potential step method was used to minimize the baseline change. The spectra were then modeled with a global regression analysis to resolve the redox centers in Na<sup>+</sup>-NQR and to determine the corresponding formal potentials. The combination of spectroelectrochemical data and global regression analysis can also be used to resolve redox centers with similar thermodynamic parameters.

The next aim is to characterize the coupling between redox transitions and Na<sup>+</sup> uptake and release. The IR spectroelectrochemical measurements may provide structural changes related to redox reactions of the cofactors. The vibrational spectra might provide information for the pathways of sodium translocation. There are a number of obstacles to performing vibrational spectroelectrochemical measurements: strong water absorbance, limitations in the optical windows, detector sensitivity and temperature control problems. The broad water lattice vibrations below 1000 cm<sup>-1</sup> are very sensitive, even for a small pathlength (10 μm) or sampling conditions. The low signal-to-noise ratio was

because of the decreased light intensity in the far-IR region, and the smaller vibrational mode extinction coefficients makes it hard to select the window material and a detector with the right sensitivity. The baseline distortions due to the imprecise temperature control can result in thermal bands. Each of these issues has to be considered in future work. A possible approach is to immobilize the protein in a vesicle or dehydrate protein film on an electrode surface in order to reduce the solvent background absorption in protein spectroelectrochemistry in the IR region.

